X-ray diffraction from semiconductor quantum dots

Dissertation der Fakultät für Physik
der
Ludwig-Maximilians-Universität München

Ingo Kegel

Mai 2000

X-ray diffraction from semiconductor quantum dots

Dissertation der Fakultät für Physik
der
Ludwig-Maximilians-Universität München

vorgelegt von Ingo Kegel
geboren am 16.12.1972 in Berlin

München, den 2. Mai 2000

1. Gutachter: Prof. Dr. J. Peisl
2. Gutachter: Prof. Dr. J. P. Kotthaus

Tag der mündlichen Prüfung: 27. Juli 2000

Zusammenfassung

Diese Arbeit zeigt Fortschritte bei der experimentellen und analytischen Methodik zur Untersuchung selbstorganisierter Quantenpunkte mit Röntgenbeugung. Es werden zwei Themenkomplexe behandelt: Die quantitative Bestimmung von Korrelationen in Quantenpunkt-Multischichten sowie die Messung von Verzerrungs- und Zusammensetzungsprofilen in unbedeckten Quantenpunkten.

Für die Charakterisierung der vertikalen Anordnung in säulenartigen Stapeln von Quantenpunkten, die bei einem Wachstum von Multischichten zu beobachten sind, wird eine Meßmethode in Beugungsgeometrie zusammen mit einem statistischen Modell vorgestellt, welches eine quadratische Verbreiterung der Bragg-Schichten mit lateralem Impulsübertrag vorhersagt. Das Modell wird anhand von Ge/Si(001) Multischichten mit Zwischenschichten verschiedener Dicke demonstriert und der analytische Ansatz bestätigt. Die laterale Ordnung der Quantenpunkte wird über die Verzerrungsmodulation im Substrat untersucht. Ein analytisches Modell für den kurzreichweitigen Ordnungszerfall von Gitterlinien entlang eines durch den Oberflächen-Bragg-Reflex vorgegebenen Azimuths ermöglicht die vollständige Bestimmung von Form und Korrelation der Quantenpunkte.

Die experimentelle Untersuchung von Verzerrungsfeldern und Materialzusammensetzung von Quantenpunkten wird mit einem streutheoretischen Ansatz von Iso-Verzerrungsflächen zu einer Technik entwickelt, die keine funktionalen Zusammenhänge über den gesamten strukturellen Aufbau der Quantenpunkte postulieren muß. Neben einer experimentellen Auflösung bezüglich des Verzerrungszustandes, werden durch das Ausnutzen von Mehrfach-Streuprozessen bei Beugung unter streifendem Einfall und der daraus resultierenden erweiterten optischen Funktion eine sub-Nanometer Höhenauflösung erzielt. Zusammen mit der Bestimmung der Krümmung der Iso-Verzerrungsflächen erlaubt diese Datenbasis die Darstellung des Verzerrungsfeldes im unbedeckten Quantenpunkt als tomographisches Bild. Zusätzlich kann mittels Kontrastvariation an starken und schwachen Reflexen die Materialzusammensetzung als Funktion der Höhe im Quantenpunkt ermittelt werden.

Mit der Bestimmung der Verzerrungsbilder und des vertikalen Zusammensetzungsprofils an verschiedenen Serien von unbedeckten InAs/GaAs(001) Quantenpunkten gibt diese Arbeit eine Antwort auf die umstrittene Frage nach dem bislang weitgehend unbekannten inneren Aufbau von freistehenden Quantenpunkten. Die Interdiffusion von epitaktisch aufgebrachtem Material und Substrat stellt sich als stark temperaturabhängig heraus. Für InAs Quantenpunkte, die bei Substrattemperaturen oberhalb 500° C hergestellt werden, besteht bereits mehr als die Hälfte des Quantenpunktes aus Substratmaterial. Diese unerwartete experimentelle Tatsache wird durch atomistische Relaxations-Rechnungen als selbstkonsistent bestätigt.

Contents

Note to the reader

For the sake of conciseness, techniques and theories which have been described extensively in widely available literature are not discussed in detail in this thesis. This allows for a leaner structure and a clear focus on the actual scientific advances which lead to this publication. For background reading, the two following books are highly recommended:

- For an excellent discussion of grazing incidence diffraction see

  H. Dosch, *Critical Phenomena at Surfaces and Interfaces* (Springer, Berlin, 1992).

- For a comprehensive report on applications and physical properties of semiconductor quantum dots see

  D. Bimberg, M. Grundmann, and N. N. Ledentsov, *Quantum Dot Heterostructures* (Wiley, Chichester, 1999)

Introduction

The quickly evolving field of self-organized quantum dots has evoked high hopes in the community of solid state physicists, where everything is geared towards one word: *nano*. From nano-technology to self-organized quantum dots, the focus of scientific research is shifting from properties of bulk matter towards a world of crystalline structures whose size is of the length scale where the quantum-mechanical nature of matter is at home and the wavelength of a conduction band electron is no longer small compared to its host crystal. And yet, already a cube of 10 nanometers base length may contain more than 50000 atoms, a giant lump of matter from a molecular point of view, but hardly detectable until the recent advent of scanning microscopies. *Visualizing* a world so small that it evades even the resolution of light, was the major achievement which paved the way for today's scientific road map.

Self-organized quantum dots play an important role in the arena of candidates for novel devices. Such islands of perfect crystallinity can be produced in macroscopic numbers by standard techniques of epitaxial thin film growth. Although various sources of self-organization are increasingly exploited, such as the recently reported ion sputtering technique [1], the Stranski-Krastanow growth mode [2] in lattice mismatched heteroepitaxial systems is the most widely used procedure for the fabrication of quantum dot samples. The deposited material forms bonds to the substrate atoms and the resulting lattice is massively strained to meet the requirements of the bulk substrate, but, at a certain point, the growth process will become unstable as the gains of regrouping independently with respect to the substrate outweigh the increase in surface energy. Nevertheless, the growth conditions may often be chosen such that all atoms place themselves coherently with respect to the substrate, with definite spatial relationships from layer to layer, without any formation of dislocations. While the bottom of the arising island remains pseudomorphically attached to the substrate, the higher parts of the three-dimensional structure are free to gradually relax towards their bulk state. This relaxation introduces strain and consequently a varying local lattice parameter into the common lattice of substrate and island.

As easy as the energetic principle which gives rise to this kind of self-organization, as complex is the dependence of the island morphology on the growth parameters. Similar to the seemingly simple hydrodynamic problem of Couette flow [3] – investigated for one century and yet not fully explored – the manifestations of self-organized growth are of a dazzling variety which seems irreconcilable with the quest for a simple theoretical framework which could make quantitative predictions for such systems. With the words of H. L. Swinney [4]:

> "*There is no general theory to describe the behavior of systems far beyond primary instability. In contrast to equilibrium systems, there is no function like the free energy that can be determined and minimized to find the state of a non-equilibrium system for a given set of control parameters. The many attempts to find an extremum principle for systems far from equilibrium have all failed. However, it is just this regime far from equilibrium that is often of interest in nature and technology, where one would like to be able to predict the behavior of, e.g. the atmosphere and oceans, combustion, mixing and separation processes, and biological systems.*"

Therefore, for the understanding and even for the *discovery* of the properties self-organized systems, the primary input is experimental. To establish a sound basis for the development of detailed energetic and kinetic arguments which tempt to fully explain the process of self-organization, the crystalline structure and the statistical properties of spatial distributions have to be known as accurately as possible.

X-ray diffraction usually does not provide the impressive visual results of image producing techniques, but fulfills the important task of assessing the crystalline properties of a sample with high quantitative accuracy. The most fruitful research arises from a combination of the two approaches in real and reciprocal space. While microscopical techniques deliver the general ideas about the fundamental structure of a sample, x-ray diffraction contributes the quantitative details and the crystalline status of the atomic lattice.

This thesis presents methodical advances for two different areas of characterization:

(i) First, statistical properties of spatial arrangements *between* quantum dots are investigated for columnar stacks of quantum dots in multilayered samples and single layers of islands. This thematic complex is treated in chapter 1, where samples from the Ge/Si(001) material system are analyzed. The quality of vertical stacking can now be easily calculated from scattering data, which has been used for analyzing the influence of spacer thickness on vertical ordering. In addition, the evaluation of lateral ordering is facilitated by the concept of measuring diffraction from “strain lattices” as a replacement for conventional small angle forward scattering experiments.

(ii) Second, a method is developed to map out the strain field *within* uncapped islands and determine the vertical composition profile without assuming holistic functional models for the entire structure of the dots. Thus, *images* can be calculated from the x-ray data, bringing the tomographic power of x-rays to a size-regime that was previously thought to be inaccessible for such methods. A detailed discussion of why this achievement is possible – rather unusually for a scattering technique where half the spatial information is lost due to the phase problem – is presented in chapter 2. Using this technique, the influence of substrate temperature on the growth process is investigated for InAs/GaAs(001) islands.

At the time of this writing, it seems to become increasingly accepted that interdiffusion in self-organized quantum dots is a process which is central to growth and morphology itself [5–7], rather than just being a “real-structure” effect which can be neglected in first order approximations. This recent insight has important implications for the understanding of growth dynamics as well as the electronic properties in device applications. While indirect evidence for this revised point of view has been available for about a year prior to the findings presented in chapter 2, these x-ray measurements constitute the first spatially resolved determination of material composition in free-standing islands.

Chapter 1

Ordering analysis of self-organized quantum dots

1.1 Vertical ordering in quantum dot multilayers

1.1.1 Introduction

Vertical stacking of quantum dots in superlattices grown in the Stranski-Krastanow mode is considered a promising technique for improving their size homogeneity [8–11] which is crucial for all kinds of applications [12–14]. Quantum dot formation on non-prepatterned substrates usually results in broad distributions of inter-dot distances and consequently of dot sizes. Due to growth dynamics and various interactions between the dots [15, 16], optimally equalized kinetic and thermodynamic growth conditions can only be achieved if all nucleation centers are distributed on equivalent positions of a lattice. In the case of vertical stacking, a number of bilayers of substrate and dot material are deposited in sequence, while the buried dots act as stressors in a matrix of different lattice parameter, influencing the morphology of the consecutively formed interfaces. Strain propagation through the spacer layer serves as a low pass filter for the preferred nucleation sites in the next layer, decreasing the variation in nearest neighbor distance and size [17]. Ever since the original proposal for a self-improving lateral arrangement has been presented [18], investigations on the optimization of this process have been carried out [19–22], revealing the multifaceted complexity of the subject. Recent theoretical studies [23, 24] emphasize the importance of spacer thickness for the final configuration after a given number of bilayers. While lateral correlational properties are easily accessible by scanning microscopies [25, 26], the analysis of the vertical alignment of the dots traditionally requires demanding cross-sectional transmission microscopy recordings [18, 27] which serve as case studies for single dot columns but cannot provide sufficient accuracy and sample size for a statistical evaluation of the horizontal dot displacements from an average dot position.

In this chapter, an x-ray scattering analysis is presented [28], which is designed to provide a quantitative estimate of the mean deviation from perfect stacking based on a macroscopic portion of the sample's surface. Section 1.1.2 gives details on the kinematic model describing the profile of the Bragg-sheets [29] induced by the superstructure of the bilayers. In section 1.1.3 the experimental technique allowing for the determination of the model parameter for imperfect stacking with sufficient accuracy is described. The experimental results of two Ge/Si(001) samples with different spacer thicknesses are discussed in section 1.1.4.

1.1.2 Analytical model

Horizontal deviations in the vertical stacking of quantum dots are partly driven by deterministic factors based on the various interactions between quantum dots. From interface to interface, strain propagation through the spacer layers alters the initial energetic situation which growth kinetics has to respond to [30] . The mean dot positions may thus change in a deterministic way which depends on the spatial configuration of the first dot layer. The general features of column bending and other processes like merging of different dot stacks as well as the dying out of single columns can be observed in cross sectional TEM measurements [20, 31, 32].

From an analytic point of view, a complete treatment of the "microscopic" evolution of dot columns is often not necessary. Progress in growth techniques relies on characterization of sample series and the comparison of meaningful parameters. Using the relative randomness of the first dot layer on the substrate, averaging is performed over the whole ensemble of dots, which leads to the description of the evolution of a mean column whose lateral displacements are random in nature (Fig. 1.1). For the propagation of one bilayer to the next, a Gaussian distribution of horizontal deviations from the underlying reference dot is assumed. If the interaction between next nearest neighbor bilayers is assumed to be negligible, the width of the lateral dot distribution with respect to the lowest reference dot increases in a random walk-like manner:

$$\sigma_n = \sqrt{n}\,\sigma \tag{1.1}$$

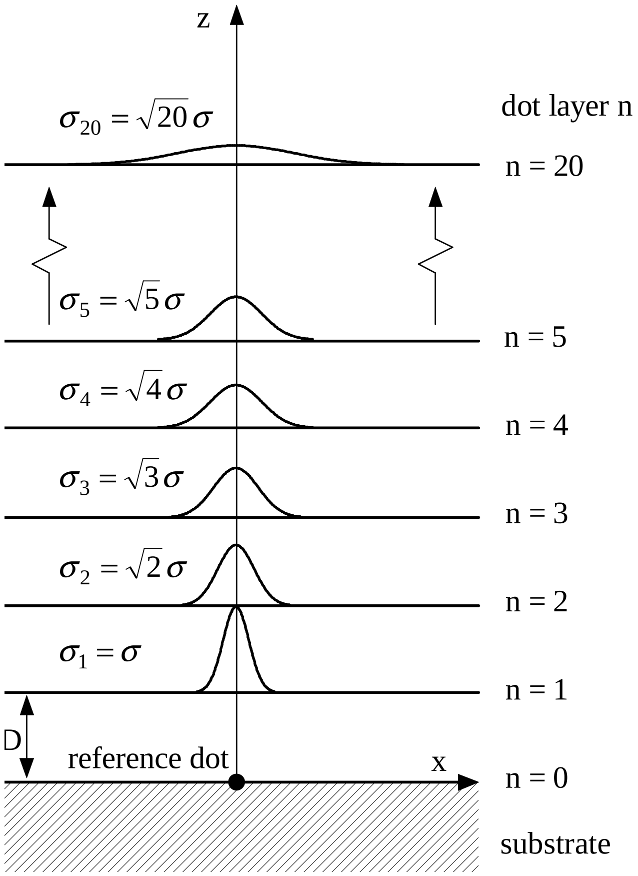

Figure 1.1: Model for the lateral deviations from an average dot position. The half width of the spread in lateral position increases in a random walk-like manner. The mean position of the average dot column is pinned by the reference dot closest to the substrate.

where n is the bilayer number starting with $n = 0$ and σ parameterizes the distribution of the horizontal shift from bilayer to bilayer, whose mean is always congruent with the position of the reference dot. The concept of a mean deviation from perfect stacking σ essentially captures the average quality of the vertical dot alignment. Figure 1.1 visualizes this description for a 20 bilayer sample of period D.

From a kinematical viewpoint the total intensity scattered from a quantum dot multilayer is the product of four factors:

(i) a pair of transmission functions [33] describing the incidence and exit of the wave through the surface,

(ii) a dot form factor [34, 35] modulating the overall intensity,

(iii) a lateral correlation term [36]

(iv) and a function describing the influence of the dot stack.

The following analysis focuses on the functional dependence of the intensity on the vertical momentum transfer q_z to the scattered x-rays. The effects of in-plane correlations result in a constant factor for fixed lateral momentum transfer $q_{||}$ and are therefore not considered. The form factor and the transmission functions exhibit a slow variation along q_z as compared to the superstructure effects. Although they would be needed in a complete fit of the scattering intensity, one can extract the parameter σ from changes in the Bragg-sheets' half width half maxima (HWHM) in q_z where the other terms only provide for a monotonous background and can therefore be excluded. Diffuse scattering of micro-roughness is estimated to be a smaller order effect as compared to dot scattering, especially on epitaxially grown interfaces [37] . The remaining task is the determination of the structure factor of an average dot column.

A phase summation over the stack of N dots gives the average scattering amplitude in $q_{||}$ and q_z normalized to the form factor of a single dot:

$$\begin{aligned} F_N\left(q_z, q_{||}\right) &= \sum_{stack} e^{i\mathbf{q}\cdot\mathbf{r}} e^{-\mu(N-1-n)} \\ &= \sum_{n=0}^{N-1} e^{iq_z Dn} \left\langle e^{iq_{||}x} \right\rangle_{layer} e^{-\mu(N-1-n)} \end{aligned} \tag{1.2}$$

where the vertical positions are assumed to be perfectly correlated and x is the lateral deviation of the reference dot for each column. A dimensionless attenuation factor μ has to be taken into account to describe the loss of intensity in the x-ray beam from one bilayer to the next. The averaging is performed over all dots in one layer, resulting in an integral over the distribution of lateral displacements $P(x, n)$:

$$\begin{aligned} F_N\left(q_z, q_\|\right) &= \sum_{n=0}^{N-1} e^{iq_zDn-\mu n} \int\limits_{x=-\infty}^{\infty} e^{iq_\| x} P\left(x,n\right) dx \\ &= \sum_{n=0}^{N-1} e^{iq_zDn-\mu n} \int\limits_{x=-\infty}^{\infty} e^{iq_\| x} \left(\frac{e^{-\frac{1}{2}\frac{x^2}{n\sigma^2}}}{\sqrt{2\pi n}\,\sigma} \right) dx. \end{aligned} \tag{1.3}$$

Evaluation of the integral leads to a finite sum of complex phases, which is easily evaluated as

$$\begin{aligned} F_N\left(q_z, q_\|\right) &= \sum_{n=0}^{N-1} e^{-n\left(\sigma^2 q_\|^2 - iq_zD-\mu\right)} \\ &= \frac{1-e^{N\left(iq_zD-\sigma^2q_\|^2-\mu\right)}}{1-e^{iq_zD-\sigma^2q_\|^2-\mu}}. \end{aligned} \tag{1.4}$$

The structure factor can then be transformed to the following expression (see Appendix A):

$$\begin{aligned} S_N\left(q_z, q_\|\right) &= \left|F_N\left(q_z, q_\|\right)\right|^2 \\ &= e^{-\sigma^2 q_\|^2 (N-1)} \frac{\sin^2 \frac{q_zND}{2} + \sinh^2 \frac{\sigma^2 q_\|^2 N+\mu}{2}}{\sin^2 \frac{q_zD}{2} + \sinh^2 \frac{\sigma^2 q_\|^2 +\mu}{2}}. \end{aligned} \tag{1.5}$$

For reasons of clarity μ is set to 0 in the following discussion of this result. For $\sigma = 0$, Eq. (1.5) reduces to the usual Laue formula for a finite grating. Even for $\sigma \neq 0$ the scattering intensity along the specular path at $q_\| = 0$ does not differ from a perfectly aligned stack. Only the diffuse scattering at $q_\| \neq 0$ is influenced by the lateral deviation from perfect stacking. The functional dependence of the structure factor on $q_\|$ is shown in Fig. 1.2 at different $\sigma q_\|$ for the case of a $N = 20$ multilayer. Three important features of the distribution described by Eq. (1.5) can be noticed:

(i) The total thickness oscillations die out rapidly for increasing $q_\|$. While their amplitude $\Delta S_{N,thickness}$ is 1 in the close vicinity of the specular condition, it vanishes as

$$\Delta S_{N,thickness} \approx 2\, e^{-\sigma^2 q_\|^2 N} \quad \text{for} \quad \sigma q_\| \gg 1. \tag{1.6}$$

For large N, thickness oscillations will therefore be confined to values of $\sigma q_\|$ smaller than $N^{-\frac{1}{2}}$.

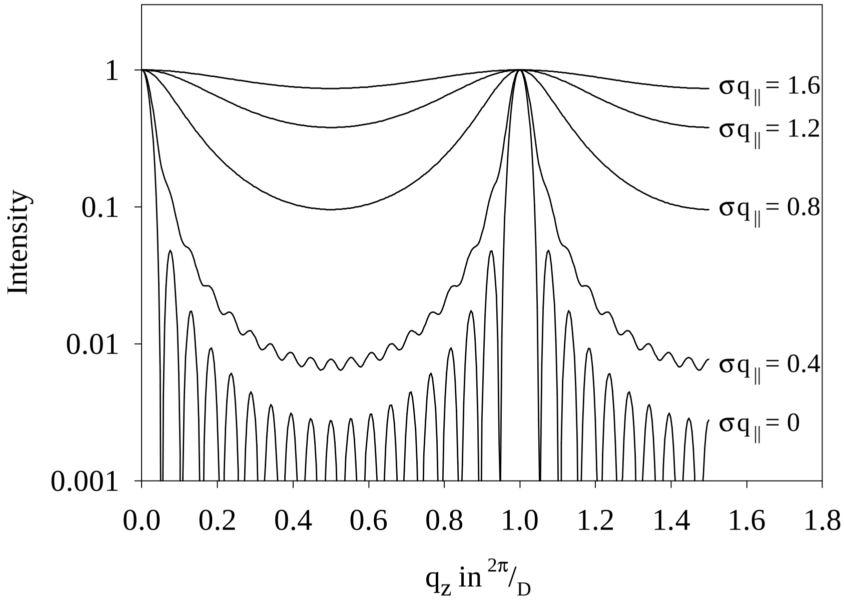

Figure 1.2: Modified Laue function for dot column scattering for different values of $\sigma q_\|$. All curves are normalized to their peak intensity. The lowest graph for $\sigma q_\| = 0$ is equivalent to the simple Laue function resulting from the interference of 20 bilayers. As the total thickness fringes vanish for increasing $\sigma q_\|$, the envelope gets broader and eventually turns into a single bilayer oscillation on top of a constant background.

(ii) The relative intensity in between the main maxima is increasing with $q_\|$. Averaging the rapid oscillation of the first term in the numerator of Eq. (1.5) one obtains the contrast

$$\frac{S_N^{max} - S_N^{min}}{S_N^{min}} = \frac{\tanh^2 \frac{1}{2} N \sigma^2 q_\|^2}{\tanh^2 \frac{1}{2} \sigma^2 q_\|^2}. \tag{1.7}$$

For small arguments, where the peak intensity has a weight of approximately N^2, the contrast decreases slowly with the fourth power of $\sigma q_\|$, whereas for large values of $\sigma q_\|$ it vanishes exponentially, but independently of the number of bilayers:

$$\frac{S_N^{max} - S_N^{min}}{S_N^{min}} \approx \begin{cases} \left(1 - \frac{1}{4}\sigma^4 q_\|^4\right) N^2 & \text{for} \quad \sigma q_\| \ll \frac{1}{\sqrt{N}} \\ 2\, e^{-\sigma^2 q_\|^2} & \text{for} \quad \sigma q_\| \gg 1 \end{cases} \tag{1.8}$$

The contrast resulting from a $N = 20$ multilayer is shown in Fig. 1.3.

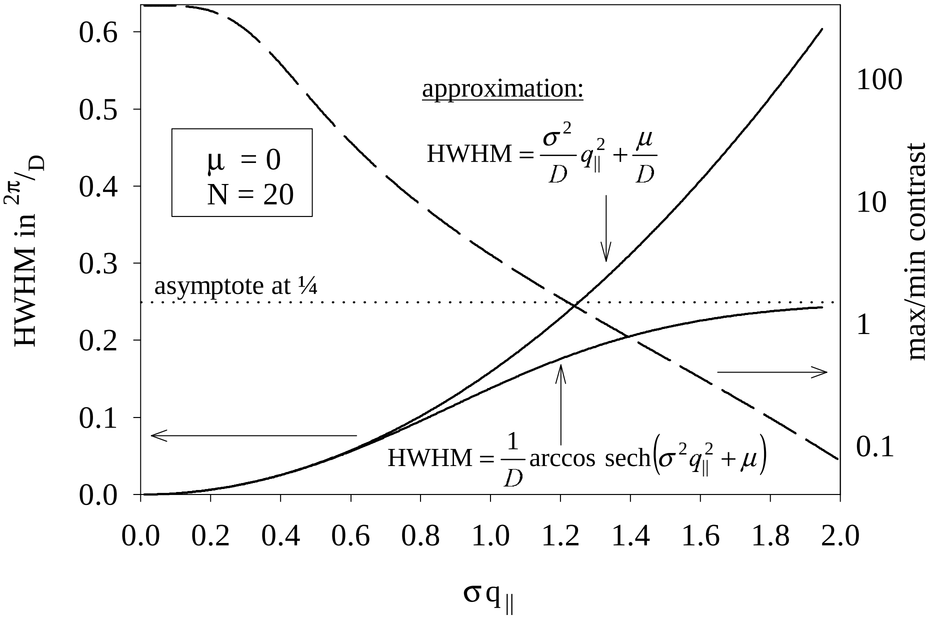

Figure 1.3: Half width half maxima from Eqs. (1.9) and (1.10) and contrast of the Bragg sheets against the intensity in between them as predicted by Eq. (1.7). The quadratic approximation to Eq. (1.9) is seen to be highly accurate for values of $\sigma q_\| < 0.5$ but fails as the exact expression levels off asymptotically to $\frac{1}{4}$

(iii) The HWHM in q_z of the envelope over the thickness oscillations is increasing with $q_\|$ until is saturates at its maximum possible value of $\frac{1}{4}$ of the reciprocal period of the superstructure. At this point, the functional dependence of the envelope corresponds to the oscillation caused by a single bilayer on top of a constant background. The HWHM, which has to be evaluated with respect to the minimum intensity in between the Bragg-sheets, can be calculated analytically as (see Appendix A)

$$\Delta q_z^{HWHM} = \frac{1}{D} \text{ arccos sech} \left(\sigma^2 q_\|^2 + \mu\right) , \tag{1.9}$$

taking again into consideration the attenuation factor μ. A useful approximation for small $\sigma q_\|$ reveals a quadratic increase of the HWHM in q_z with lateral momentum transfer:

$$\Delta q_z^{HWHM} = \frac{\sigma^2}{D} q_\|^2 + \frac{\mu}{D} \tag{1.10}$$

Figure 1.3 shows Eq. (1.9) together with its approximation Eq. (1.10) which deviates from the exact expression by less than 1% for $\sigma q_{\|} < 0.5$. The validation of Eq. (1.10) is the most convenient way to determine the parameter σ from experimental results. In comparison, Eq. (1.6) is based on a small signal that dies out rapidly with $q_{\|}$ while Eq. (1.8) requires a complete simulation of the q_z-spectrum which introduces further unknown parameters.

1.1.3 Experimental technique

A suitable scattering geometry for the determination of the model parameter σ according to Eq. (1.10) has to provide for resolutions in $q_{\|}$ of the order of $\sigma^{-1}\sqrt{N}$ as well as a weak background allowing for a clear differentiation of the Bragg-sheets whose contrast is given by Eq. (1.7). Here, it is best to consider an “out of plane” measurement at constant angle of incidence α_i where the detector is rotated around the surface normal [38]. Assuming typical diffractometer distances and wavelengths of 1.5 Å, the width of the resolution element in $q_{\|}$ can be brought down to 0.0005 Å^{-1} using either a triple crystal setup or a collimation path. For $N = 20$ multilayers the rule of thumb given above sets a maximum observable σ at about 500 Å. ”In-plane” measurements [39], where incident beam, surface normal and detector all lie in the same plane can achieve higher resolutions but create additional difficulties, such as low maximum $q_{\|}$ for small q_z and varying scattering depth along a Bragg-sheet [40]. In any case, the use of synchrotron radiation is mandatory to achieve an adequate collection of data points.

In forward scattering experiments [41–43], which are sensitive to the electron density contrast, parasitic contributions from air scattering of specular and primary beam are hard to minimize and often not negligible. For a crystalline sample, measurements can be performed in the vicinity of a surface Bragg peak of the spacer material separating the layers, thus exploiting the lattice modulation induced by the self-assembled quantum dots. The scattering geometry is sketched in Fig. 1.4. While the scattering angle 2θ remains fixed at its value for the silicon $(hk0)$ reflection, non-zero values of $q_{\|}$ with respect to the surface Bragg-peak are obtained by varying the azimuth ω around the Bragg-condition θ_{Si}. The angle of incidence α_i is adjusted to obtain a scattering depth [44] exceeding the total thickness of the superstructure. A position sensitive detector simultaneously records complete spectra of vertical momentum transfer which is varied by the angle of exit α_f.

The situation in reciprocal space is visualized in Fig. 1.5. For (001) surfaces of diamond lattices, the strong (220) surface reflection is suitable for this investigation. Normal to the sample surface, a crystal truncation rod is found on the q_z-axis, which is modulated by the transmission function.

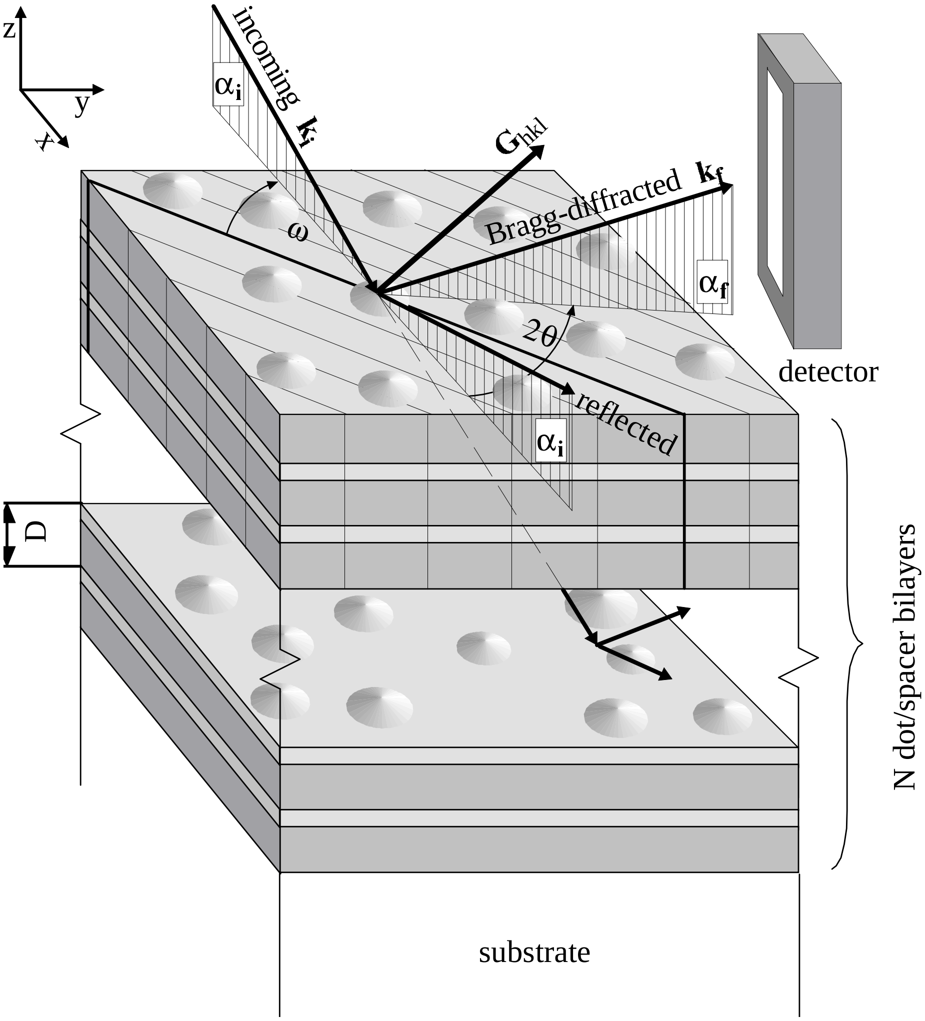

Figure 1.4: Scattering geometry for diffraction under grazing incidence and exit angles

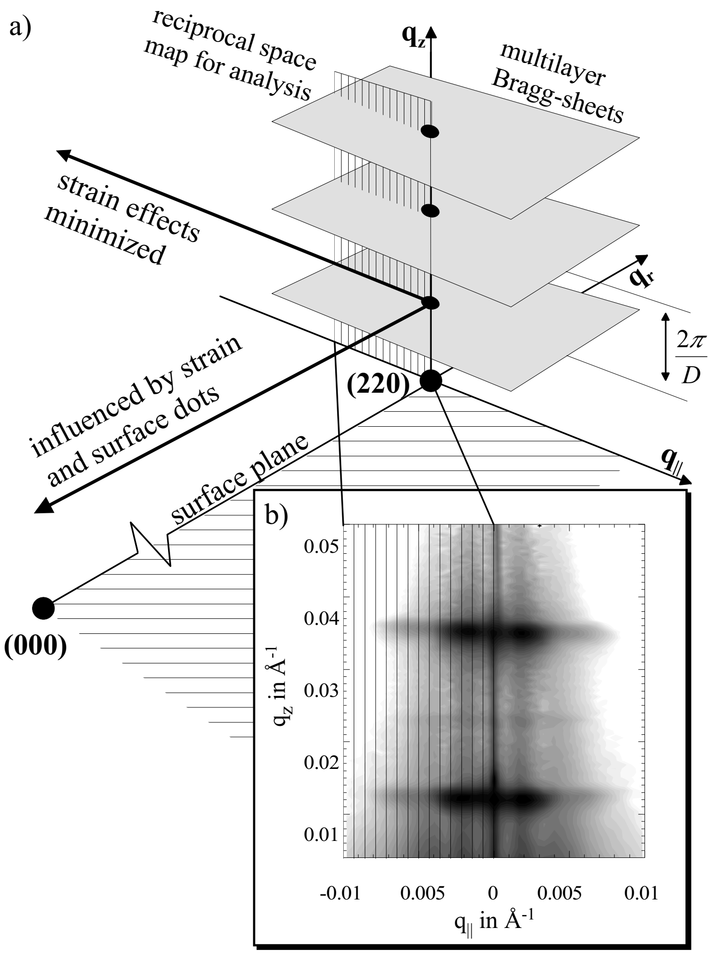

Figure 1.5: Part (a) shows a schematic representation of reciprocal space with the cross-hatched area indicating the choice of the reciprocal space map to be used for the analysis of vertical ordering. The plane of the sample surface is spanned by $q_{||}$ and q_r, while q_z designates the growth direction. The Bragg-sheets, whose spacing is given by the superlattice constant D, are clearly visible in the measured data of sample 1 as shown in (b) (logarithmic gray scale).

It is peaked at the critical angle of total external reflection α_c and exhibits marked oscillations of the superstructure, spaced at $\frac{2\pi}{D}$. Although the diffuse multilayer Bragg-sheets extend in all directions around the lattice rod that are parallel to the surface, strain asymmetries complicate the evaluation in the radial direction denoted as q_r. Hence, measurements take place in the plane spanned by the angular direction ($q_{||}$ in Fig. 1.5) and the surface normal (q_z). When choosing a suitable Bragg-sheet for the analysis, a compromise has to be made between the higher intensity of lower order Bragg-sheets and dynamical effects at low q_z near α_c, where the width of the sheets are modified and the strong curvature of the transmission function is unfavorable for the determination of the half widths in q_z. For our measurements discussed in the next section, the choice was made between second and third order Bragg-sheets.

1.1.4 Results and discussion

Two samples in the Ge/Si(100)-system with 20 bilayers were investigated, one with 300 Å Si-spacers (sample 1), the other with 100 Å Si in between the dot layers (sample 2). Lateral dot sizes are estimated from TEM recordings [45] at about 1500 Å*. X-ray experiments as described in section 1.1.3 have been performed at the TROÏKA II beamline of the ESRF at a wavelength of 1.5 Å. From the measurements along q_z, the HWHMs have been evaluated as a function of $q_{||}$ and are plotted in Figs. 1.6 and 1.7 where the resolution elements of 0.002 $Å^{-1}$ and 0.0025 $Å^{-1}$ respectively are indicated by the horizontal error bars. According to the different requirements of scattering depth, the incident angles have been set to $\alpha_i = 0.4°$ for sample 1 and $\alpha_i = 0.27°$ for sample 2.

Figure 1.6 shows the broadening of the third Bragg-sheet of sample 1 (thicker spacer layer) together with selected scans along q_z. The quadratic relationship between $q_{||}$ and the half width predicted by Eq. (1.10) is confirmed within the experimental errors and a mean statistical deviation from perfect stacking of $\sigma = 122 \pm 13$ Å is obtained from the fit of eq. Eq. (1.9). For this case, the use of Eq. (1.10) is not a satisfactory approximation for the whole measured range, since the maximum value of $\sigma q_{||}$ is close to 1.

Figure 1.7 has been recorded for sample 2 (thinner spacer layer) where the scattered intensity is found to decay much more slowly with $q_{||}$ than for sample 1. Due to the different combination of scattering depth and spacer thickness, the fitted value of the attenuation factor μ is slightly larger than

---

*see Ref. 46 for an extensive discussion of the size and temperature dependence of Ge/Si(001) islands

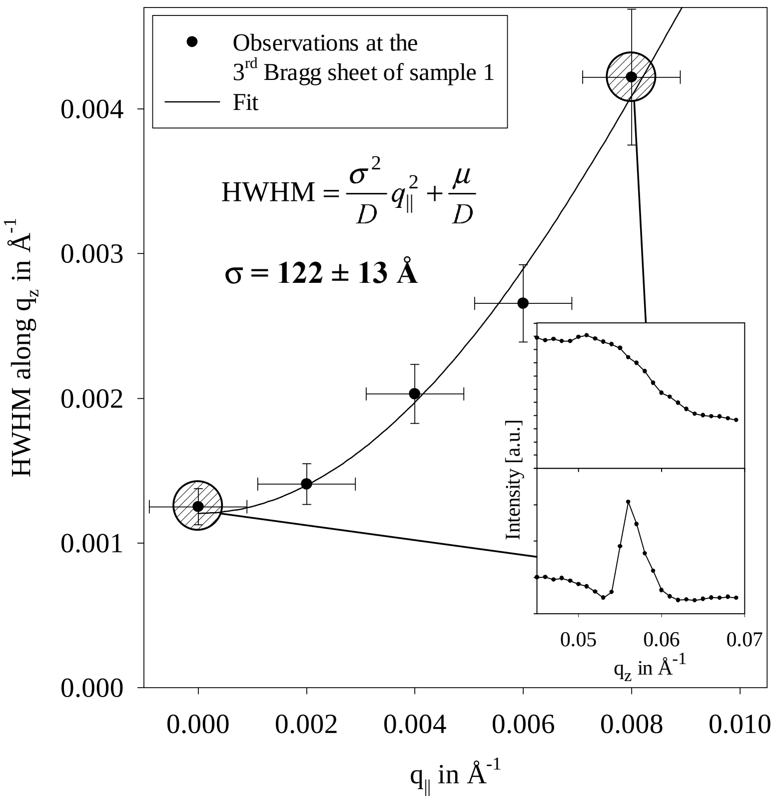

Figure 1.6: Experimental results for the half width half maxima of the 3^{rd} Bragg sheet of sample 1 (300 Å spacer). The insets show the intensity profiles along q_z for two selected values of $q_{\|}$.

for the measurement on sample 1. Here, the experimental data is well approximated by Eq. (1.10) for the whole range in $q_{\|}$ that was accessible in terms of sufficient intensity and peak contrast ($\sigma q_{\|} < 0.6$). The fit results in a statistical deviation from perfect stacking of $\sigma = 15 \pm 2$ Å. Apart from the broadening of the Bragg-sheets in q_z, the insets in Figs. 1.6 and 1.7 clearly show the reduction in contrast with $q_{\|}$ as predicted by Eq. (1.7).

Considering the lateral size of 1500 Å, these results for σ can be translated into relative values which indicate the percentage of a dot's base area that is non-congruent with the corresponding dot in the neighboring layer. TEM-data [20] and x-ray analyses [34, 47] show that the dots have square bases aligned along the $\langle 110 \rangle$ and $\langle 1\bar{1}0 \rangle$ directions. Scattering experiments at the (220) reflection therefore yield the projection of the total lateral displacement along one base of the square (Fig. 1.8). The distributions of the

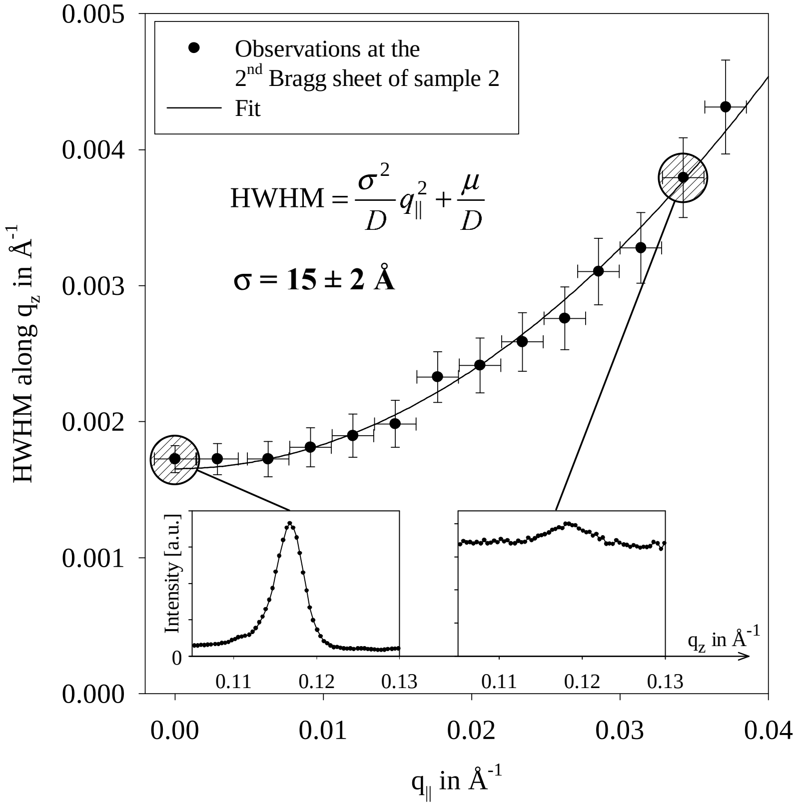

Figure 1.7: Experimental results for the half width half maxima of the 2^{nd} Bragg sheet of sample 2 (100 Å spacer). The insets show the intensity profiles along q_z for two selected values of $q_{||}$.

displacements in the orthogonal directions x and y are Gaussian with mean 0 and standard deviation σ and can be considered as independent. The average non-congruent area $\langle A_{diff} \rangle$ as defined in Fig. 1.8 is given by

$$\langle A_{diff} \rangle = \langle D \left(|\Delta x| + |\Delta y| \right) - |\Delta x| \, |\Delta y| \rangle = \sigma \sqrt{\frac{2}{\pi}} \left(2D - \sigma \sqrt{\frac{2}{\pi}} \right) \qquad (1.11)$$

from which a relative deviation from perfect stacking f can be defined:

$$f = \frac{\langle A_{diff} \rangle}{A_{dot}} = \frac{\sigma}{D} \sqrt{\frac{2}{\pi}} \left(2 - \frac{\sigma}{D} \sqrt{\frac{2}{\pi}} \right) . \qquad (1.12)$$

For sample 1, a relative deviation from perfect stacking of 13% from layer to layer is calculated, whereas sample 2 exhibits only 1.6% of relative lateral deviation from one dot to the next.

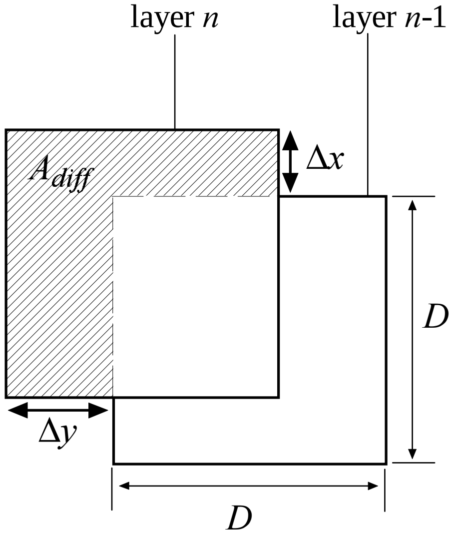

Figure 1.8: Definition of the relative lateral deviation from perfect stacking f by means of the average non-congruent area of two consecutive dots.

1.2 Strain modulation analysis of laterally ordered islands

1.2.1 Introduction

Lateral ordering effects in Ge/Si quantum dot layers have been subject to recent theoretical considerations based on calculations of total energy [15, 17, 23]. Improvements in the homogeneity of self-assembled islands are directly linked to advances in the understanding of their correlational behavior. In this section, a method is outlined [47] which is suitable to quantify ordering and correlations using the concept of random positional stacking faults.

X-ray triple crystal grazing incidence diffraction (TCGID) is a high resolution surface sensitive method revealing lattice properties of the topmost 50-5000 Å [44, 48]. With the appropriate analyzer [49], lateral length scales up to 1 μm are easily accessible. The penetration depth is minimized by confining the angles of incidence and exit to values below the critical angle of total external reflection α_c. The intensity modulation around the surface Bragg peaks induced by the lateral structure is strongly influenced by near surface strain fields in the Si-substrate and strongly varying lattice parameters in the islands. The evaluation of lateral ordering is thus most easily

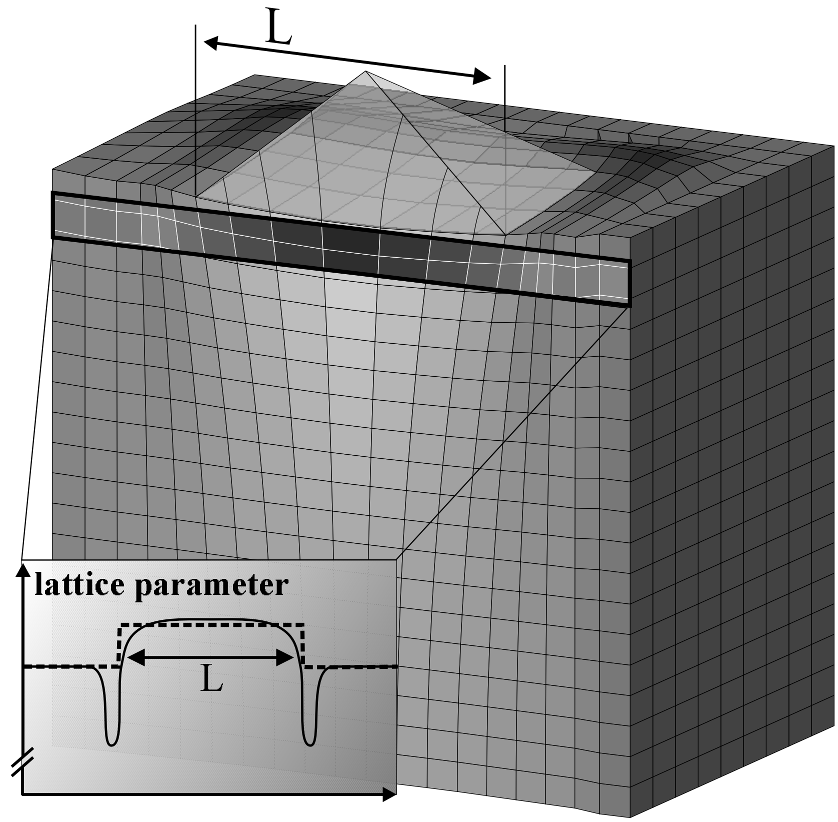

Figure 1.9: Schematic representation of the stressor-induced modulation of the lattice parameter. The near-surface region of the substrate rather than the dots themselves are subject to the presented x-ray analysis. The continuous curve in the inset indicates the lattice parameter variation along the highlighted line while the dashed line shows the approximation applied in the analytic model using only the projected size L.

achieved by investigating the scattered intensity in directions *parallel* to the lattice planes of the surface Bragg reflection of the substrate (angular scans in reciprocal space). Effects due to ordering are maximized and most readily interpreted from the small angle pattern around a surface Bragg peak of silicon. Here, strain modulations in the substrate resulting from the islands acting as stressors [50, 51] rather than their geometric modulation are dominant (Fig. 1.9).

1.2.2 Analysis and results

The investigated sample was a 20 period Ge/Si superlattice grown by molecular beam epitaxy at 670° C. Each period was constituted by nominally 5.5 monolayers Ge on top of a 300 Å thick Si spacer. The experiment was carried out at the BW2 beamline at HASYLAB/DESY using a wavelength of 1.5 Å. The angle of incidence was fixed at $\alpha_i = 0.15°$ ($< \alpha_c = 0.22°$) while the angle of exit was integrated up to α_c by means of a position sensitive detector perpendicular to the sample's surface [52]. Measurements in reciprocal space took place around the (220) and the (400) surface reflections of Si, thus yielding correlational properties of the two elastically most different directions on the Si(001) surface.

Conventional large angle x-ray diffraction data [20, 21, 53, 54] from asymmetric reflections does not allow for an easy separation of surface layer and buried dots. In our grazing incidence setup the information depth is constant and in angular directions the scattering intensity can be described as a product of the structure factor and a correlational term. Atomic force microscopy data (AFM) shows that the islands can be thought of as having a square base which is oriented along [110] and [$\bar{1}$10] [34]. The strain modulation in the substrate can then be approximated by this base shape as shown by the dashed line in the inset of Fig. 1.9. The details of the strain decay are neglected in this approach. To take account of the spread in lateral extent of the islands, the resulting structure factor is averaged incoherently with a size distribution which is assumed to be log normal for convenience:

$$S\left(q_a\right) = const \int\limits_0^\infty \left(\frac{\sin \frac{1}{2} l q_a}{\frac{1}{2} l q_a}\right)^p \exp\left[-\frac{1}{2w^2} ln^2 \left(\frac{l}{L}\right)\right] dl, \qquad (1.13)$$

where w is the width parameter determining the full width half maximum of the size distribution and p is 2 for the $\{110\}$ directions parallel to the square baselines and 4 for the $\{100\}$ directions along the diagonal of the base area (see Fig. 1.9) as given by the Fourier transform of a square of size L.

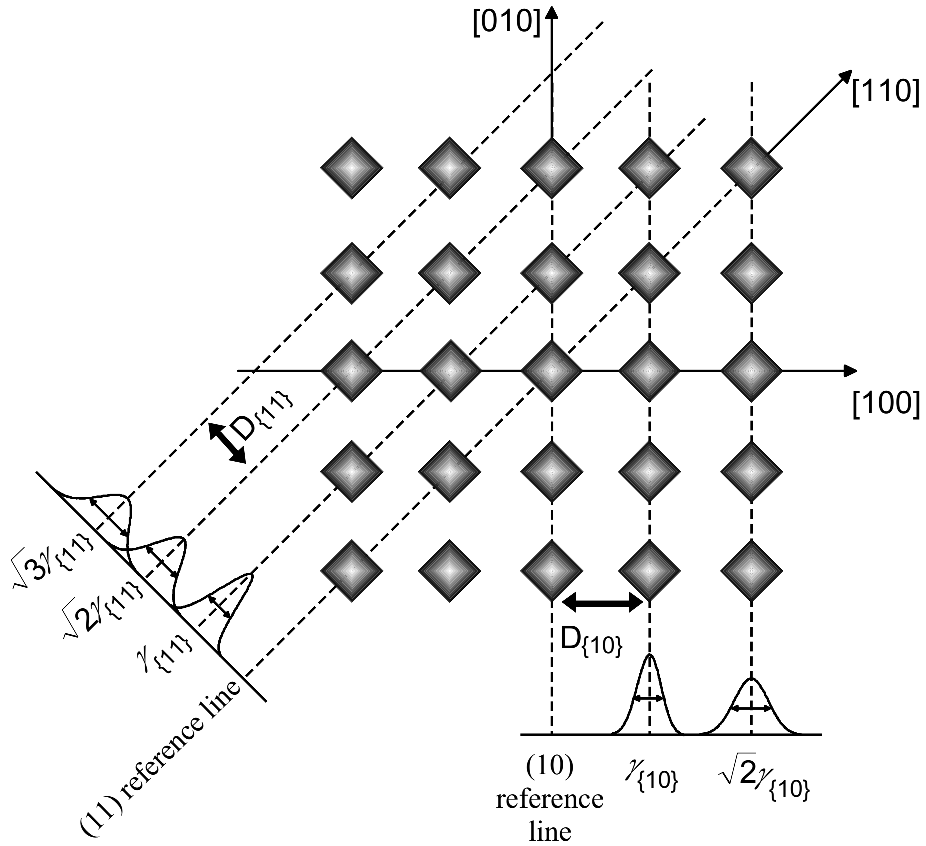

Figure 1.10: Definition of NN-distance D and disorder parameter γ. Ensembles of lattice lines are indicated by dashed lines and the distributions associated with them indicate the increasing spatial variation of the dots from their ideal lattice points with respect to the reference line at the origin. The square lattice and the orientation of the pyramids have been chosen in order to visualize the experimental result.

Since AFM measurements indicate that inter-dot ordering is very weak, long-range order arrangements [55] are not considered. The analysis of ordering is based on a random positional stacking fault argument in a local dot lattice. Although the displacements of the dots with respect to an arbitrary reference dot are two-dimensional in nature, the scattered intensity is not sensitive to displacements perpendicular to the momentum transfer of the chosen surface Bragg reflection. As a first approximation, the statistical variations from the ideal lattice points can be described in terms of 1D lattice lines with a Gaussian positional stacking fault of width γ. Subsequent folding of these positional stacking faults leads to a distribution of width $\gamma\sqrt{n}$ for the n-th neighbor (Fig. 1.10). Numerical simulations confirm the validity of this one-dimensional approach for configurations where γ is of the order of D. The disorder parameter γ can vary for ensembles of lattice lines in different directions. A correlation length ξ is defined as the distance where this width is equal to the projected nearest neighbor distance D. With the n_0-th lattice line fulfilling this condition with respect to the origin:

$$\sqrt{n_0}\gamma = D, \tag{1.14}$$

the correlation length turns out to be

$$\xi = n_0 D = \frac{D^3}{\gamma^2}. \tag{1.15}$$

In contrast to the disorder parameter γ which describes the behavior of the nearest neighbor lattice lines, the correlation length ξ expresses the extent of short range order.

The particular advantage of this one-dimensional approach lies in the fact that anisotropies of disorder and the symmetry of the lattice do not have to be assumed a priori but are obtained directly from the experimental data. The calculation of the Patterson function of the above model leads to the correlation factor $C(q_a)$ describing the scattering from random positional stacking faults [56] without an average lattice (see Appendix B):

$$C\left(q_a\right) = \frac{1-\exp\left(-\frac{1}{2}\gamma^2 q_a^2\right)}{1+\exp\left(-\frac{1}{2}\gamma^2 q_a^2\right) - 2\exp\left(-\frac{1}{4}\gamma^2 q_a^2\right)\cos\left(D q_a\right)}. \tag{1.16}$$

Neglecting optical factors and penetration depth effects which are constant at fixed α_i and α_f, the total intensity is then given by

$$I\left(q_a\right) = I_0\, S\left(q_a\right)\, C\left(q_a\right) + \text{background} \tag{1.17}$$

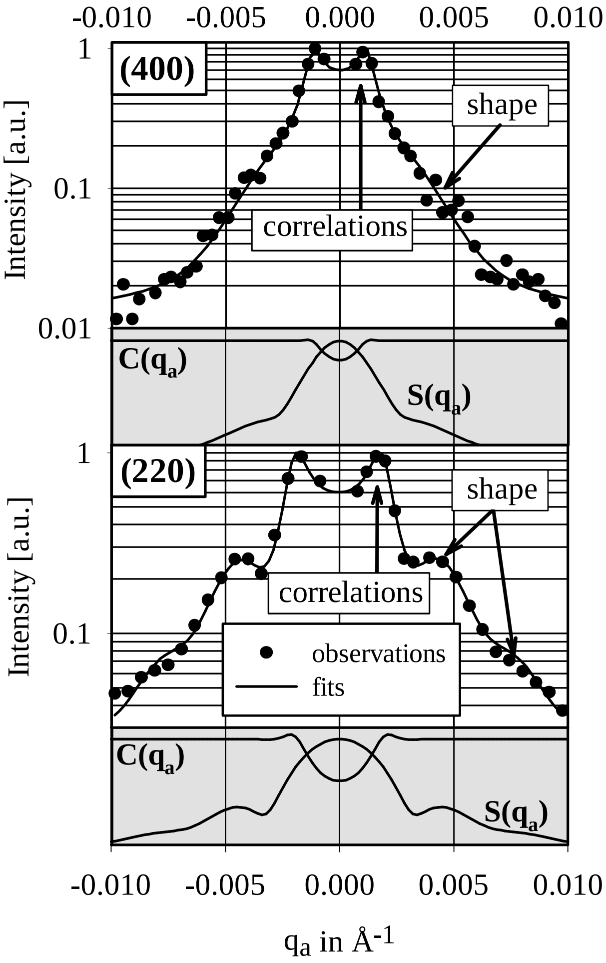

Figure 1.11: Experimental results and fits from the (400) and (220) surface Bragg reflections. The Bragg peaks at $q_a = 0$ Å^{-1} are omitted for reasons of clarity. The grey shaded graphs show the correlational term $C(q_a)$ and the structural term $S(q_a)$ separately as defined in the text.

The experimental results are shown in Fig. 1.11 together with fits of Eq. (1.17). The fit parameters are summarized in Table 1.1. The ratio of the average nearest neighbor distances from the (400) and (220) reflections

$$\frac{D_{\{10\}}}{D_{\{11\}}} = 1.48 \pm 0.07 \tag{1.18}$$

indicates that the dots are arranged in a local square lattice. This result is in accordance with the predictions in Refs. 15 and 23. Although the disorder parameter γ is found to be anisotropic, Eq. (1.15) gives a similar correlation length for both the $\langle 10\rangle$ and $\langle 11\rangle$ directions.

In particulate systems where size, nearest neighbor distance and correlation length are of the same order of magnitude, a simple evaluation of the peak positions may not give the correct results. At first hand, the second peaks in Fig. 1.11 might be explained as second correlation maxima whereas the simulation does not allow for such an interpretation. Evaluating the nearest neighbor distances from the peak positions q_{peak} as $2\pi q_{peak}^{-1}$ also leads to a square lattice but produces values for D which differ from the fitted parameters by 30%.

In contrast to forward scattering experiments which make use of the entire dot volume, this method is not hampered by surface contamination because only the sub-surface crystalline properties are probed. Also, the three-dimensional shape of the dot does not have to be taken into account. With the presented model, ordering can be quantified regarding anisotropy, nearest neighbor distance and correlation length.

Fit parameter	(220) reflection → {*110*} *directions*	(400) reflection → {*100*} *directions*
size of strain modulation L	1952 ± 32 Å	2702 ± 207Å
FWHM of size distribution	$26 \pm 7\%$	not sensitive
Disorder parameter g	1313 ± 30 Å	2423 ± 144 Å
Average NN distance D	2700 ± 47 Å	4008 ± 112 Å
Correlation Length x	11400 ± 1100 Å	11000 ± 2200 Å

Table 1.1: Correlational properties of laterally arranged Ge/Si(001) islands in the {110} and {100} directions

Chapter 2

Nanometer-scale tomographical analysis of strain and interdiffusion in uncapped self-organized quantum dots

2.1 Introduction

A detailed understanding of the growth process of self-assembled semiconductor quantum dots [12, 57–61] requires substantial knowledge about their internal structure. So far, external shape and lateral arrangement have been accessible by scanning microscopies [26]. Structural investigations with techniques like photoluminescence and Raman scattering [62,63] are restricted to estimates of scalar physical quantities such as maxima or averages of strain or material composition. For a measurement of these quantities, which delivers spatial information, some kind of resolution is needed. The resolution can either be in real space, using a direct imaging approach as in transmission electron microscopy (TEM) [64] or in reciprocal space as in an x-ray diffraction experiment [65] where spatial frequencies rather than spatial positions are probed.

The strengths of real space techniques lie in their broad applicability and the direct nature of their results. Relative drawbacks are the technologically demanding sample preparation and the limited statistics. In an x-ray diffraction experiment, the signal of a macroscopic portion of the sample's surface is integrated in the detector. The limitation of this kind of signal collection is given by the homogeneity of the dot ensemble. If the spread of a physical quantity in the dot ensemble is comparable to the spread in a single dot, the statistical value of the quantity yielded by the experiment provides no further information nor resolution.

A serious difficulty is the inaccessibility of the relative phase of the scattering process. Diffraction experiments thus usually require structural models with only a few variable parameters which are optimized to fit the measured data [66–70]. Apart from being a demanding task for a three-dimensional object of a few hundred thousand atoms with variable strain and material composition, these kinds of analyses are case studies, which are not highly generalizable. The kaleidoscopic wealth of different manifestations of self-assembled quantum dots and epitaxial growth phenomena [71, 72] calls for a more extensible and direct method for data evaluation.

In this chapter, a detailed account of an analytical approach for the analysis of grazing incidence diffraction is presented which leads to tomographic images of strain fields and material composition in the dots [73, 74]. The chapter is organized as follows: In section 2.2 the concept of iso-strain scattering is discussed, then the analytical formalism for the data evaluation is presented in section 2.3. After experimental considerations in section 2.4, results of a series of InAs/GaAs dots grown at different temperatures are shown in section 2.5 together with the comparison of experimental results and atomistic simulations.

2.2 Determination of strain and shape

2.2.1 Spatial distinction

In reciprocal space, the distance between two crystals is equivalent to the reciprocal difference of their lattice parameters. Therefore, two crystallites may be far apart in reciprocal space, even though they are spatially adjacent. For a lattice parameter difference of a few percent, the crystallites will result in two distinct peaks, whose half-widths can be used to analyze the size of each crystal (Fig. 2.1).

In this simple example there is an unspecific spatial *distinction*: two parts of a larger sample can be studied independently by tuning the scattering vector to the appropriate lattice parameters. As the lattice parameter difference between the two crystallites is reduced, the peaks merge until finally no distinction is possible anymore. This corresponds to the optical analogue of distinguishing two stars with a telescope. In this picture, the relative lattice parameter difference $\frac{\Delta a}{a}$ is equivalent to the smallest resolvable angle. Additionally, a takes the place of the wavelength of light and the common size R of the crystallites corresponds to the telescope's aperture. For a mean lattice

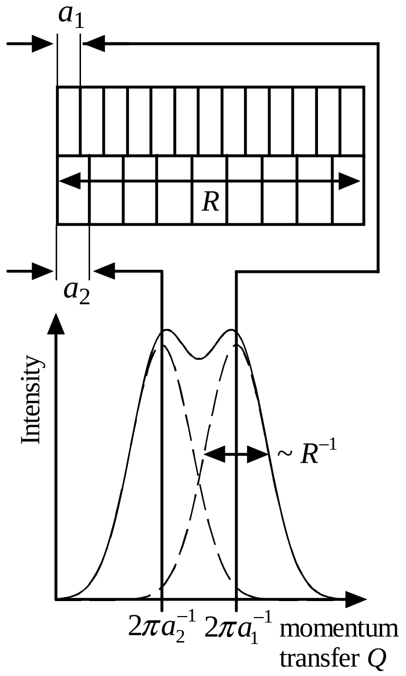

Figure 2.1: Illustration of spatial distinction in hetero-epitaxial systems. Two regions may be distinguished if their difference in lattice parameter $a_2 - a_1$ and size R are big enough to allow the resulting peaks in reciprocal space at $2\pi a_1^{-1}$ and $2\pi a_2^{-1}$ to be separated as two maxima.

parameter a, the minimum percentual difference in lattice parameter is given by

$$\left(\frac{\Delta a}{a}\right)_{\min} = C\,\frac{a}{R}, \tag{2.1}$$

where C is a constant of the order of 1 which depends on the particular shape of the crystallites. Equation (2.1) clarifies the reciprocal relationship between spatial distinction and spatial extent of the regions of equal lattice parameter.

2.2.2 Iso-strain areas

If a nano-crystal has a lattice parameter which varies continuously from one end to the other, it may be thought of as being composed of a distribution of *iso-strain areas* [35,75,76] (Fig. 2.2). For a particular Bragg reflection $\mathbf{Q}$,

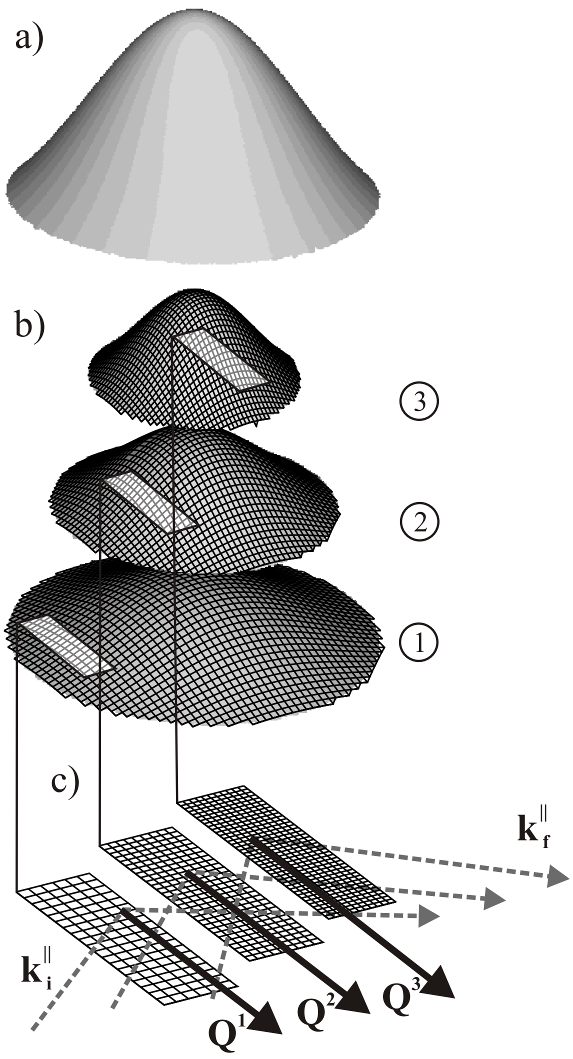

Figure 2.2: Decomposition of a strained nano-crystal into a set of iso-strain areas. Part (a) shows the outer shape of the crystal which is decomposed into areas of equal strain components ϵ in part (b). The particular choice of the Bragg point $\mathbf{Q}$ determines the condensation of the full strain tensor into the scalar ϵ. The projection of the iso-strain areas onto the $(\mathbf{k}_i^{\|}, \mathbf{k}_f^{\|})$-plane in (c) gives two-dimensional meshes which fulfill the Bragg condition at different momentum transfers indicated as $\mathbf{Q}^1$, $\mathbf{Q}^2$ and $\mathbf{Q}^3$ which allows for spatial distinction within the nano-crystal.

the iso-strain areas are defined as the iso-surfaces of the appropriate scalar component ϵ of the strain field $\underline{\boldsymbol{\epsilon}}$ which is determined as

$$\epsilon = \hat{\mathbf{Q}}^T \underline{\boldsymbol{\epsilon}} \hat{\mathbf{Q}}. \tag{2.2}$$

where the hat on $\hat{\mathbf{Q}}$ denotes a unit vector. This definition compresses the full tensorial strain status of the nano-crystal into a scalar field by neglecting shear strains. The cumulative effect of these shear strains on the scattering process can be analyzed *after* the definition of the iso-strain area by calculating rotation matrices $\underline{\mathbf{R}}(\epsilon)$ whose rotation angles $\theta(\epsilon)$ and rotation axes $\mathbf{n}(\epsilon)$ are defined by

$$\begin{aligned}
\cos\theta(\epsilon) &= \frac{\hat{\mathbf{Q}}^T \cdot \int_{\mathrm{ISA}} \underline{\boldsymbol{\epsilon}}\hat{\mathbf{Q}}\,\mathrm{d}a}{\left|\int_{\mathrm{ISA}} \underline{\boldsymbol{\epsilon}}\hat{\mathbf{Q}}\,\mathrm{d}a\right|} = \frac{\epsilon}{\left|\left\langle \underline{\boldsymbol{\epsilon}}\hat{\mathbf{Q}} \right\rangle_{\mathrm{ISA}}\right|} \\
\mathbf{n}(\epsilon) &= \frac{\hat{\mathbf{Q}} \times \left\langle \underline{\boldsymbol{\epsilon}}\hat{\mathbf{Q}} \right\rangle_{\mathrm{ISA}}}{\left|\left\langle \underline{\boldsymbol{\epsilon}}\hat{\mathbf{Q}} \right\rangle_{\mathrm{ISA}}\right|}.
\end{aligned} \tag{2.3}$$

where the subscript "ISA" denotes the integration or averaging over the entire iso-strain area. The average Bragg conditions $\mathbf{Q}_{\mathrm{ISA}}(\epsilon)$ are then located at

$$\begin{aligned}
\mathbf{Q}_{\mathrm{ISA}}(\epsilon) &= \frac{1}{1+\epsilon}\underline{\mathbf{R}}(\epsilon)\mathbf{Q} \\
&\approx (1-\epsilon)\,\underline{\mathbf{R}}(\epsilon)\mathbf{Q} \quad \text{for} \quad \epsilon \ll 1.
\end{aligned} \tag{2.4}$$

Considering only scattering vectors in the plane $\mathcal{P}$ with normal $\mathbf{p}$ spanned by the incoming beam $\mathbf{k_i}$ and $\mathbf{Q}$, the projection of each iso-strain area onto $\mathcal{P}$ may be viewed as a two-dimensional crystal (Fig. 2.2c). From this point of view, each iso-strain area has a homogeneous, non-distorted lattice which scatters around the projected Bragg point.

For distortions which are anisotropic with respect to $\hat{\mathbf{Q}}$ and $\hat{\mathbf{Q}} \times \mathbf{p}$, the projected Bragg positions $\mathbf{Q}^{proj}_{\mathrm{ISA}}(\epsilon)$ are given by

$$\mathbf{Q}^{proj}_{\mathrm{ISA}}(\epsilon) \approx (1-\epsilon)\left[\underline{\mathbf{R}}(\epsilon)\mathbf{Q} - \mathbf{p}\big(\underline{\mathbf{R}}(\epsilon)\mathbf{Q}\cdot\mathbf{p}\big)\right], \tag{2.5}$$

defining a new matrix $\underline{\mathbf{R}}^{proj}(\epsilon)$ such that

$$\mathbf{Q}^{proj}_{\mathrm{ISA}}(\epsilon) \approx (1-\epsilon)\,\underline{\mathbf{R}}^{proj}(\epsilon)\mathbf{Q} \quad \text{for} \quad \epsilon \ll 1. \tag{2.6}$$

For isotropic distortions with respect to $\hat{\mathbf{Q}}$ and $\hat{\mathbf{Q}}\times\mathbf{p}$, the shear components in the plane $\mathcal{P}$ will average out giving $\mathbf{n}(\epsilon) = \hat{\mathbf{Q}}\times\mathbf{p}$. In this case, $\underline{\mathbf{R}}^{proj}(\epsilon) = \underline{\mathbf{1}}$ in Eq. (2.6) and the projected Bragg points of the iso-strain areas are associated with momentum transfers which are scalar multiples of $\mathbf{Q}$.

2.2.3 Spatial resolution

Spatial *resolution* implies the determination the relative position of the two crystallites. While there is no generic procedure to determine relative arrangements for the general case, self-assembled quantum dots grown in the Stranski-Krastanow (SK) mode are subject to boundary conditions which reduce the three-dimensional positional difference to a one-dimensional scalar value. In SK systems, the stress energy that builds up during the growth of mismatched hetero-epitaxial layers is lowered through the formation of three-dimensional nanometer-sized islands, whose crystalline structure remains coherent to the underlying substrate. This coherency demands that the lattice parameter parallel to the surface normal is relaxed gradually from bottom to top, leading to the decomposition into iso-strain areas as explained in section 2.2.2.

Changing the selected strain state by adjusting the total momentum transfer $\mathbf{Q}$ to a different $\mathbf{Q}_{\mathrm{ISA}}^{proj}(\epsilon)$ thus corresponds to a change in *height* above the sample's surface (Fig. 2.3). Assuming the height above the surface $h(\epsilon)$ to be a monotonic function of the strain state ϵ and rewriting Eq. (2.1)

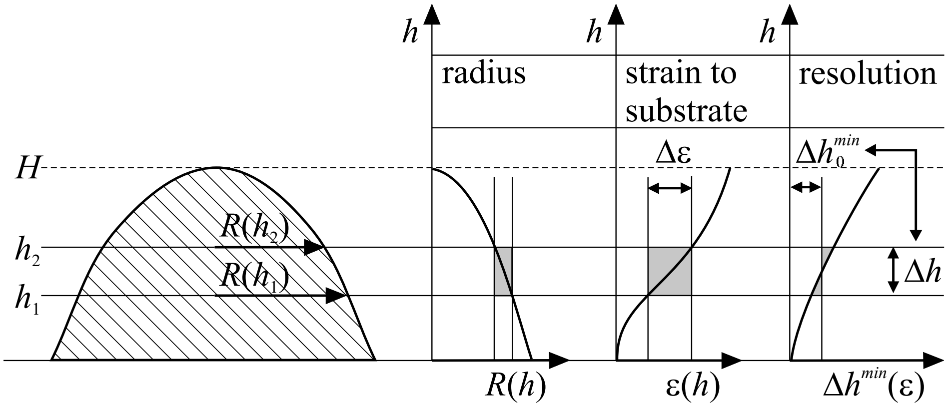

Figure 2.3: Schematic functional dependence of strain, height and resolution in islands grown in the SK mode. Radius R and strain to substrate ϵ are required to calculate the local minimum height difference Δh^{min} to resolve two parts of the nano-structure. In the particular case shown in the figure, the heights h_1 and h_2 are resolvable since their height difference Δh exceeds the mean local minimum value of Δh_0^{min}.

in reciprocal space coordinates as

$$\Delta\epsilon \approx C\frac{2\pi}{R(\epsilon)Q} \quad \text{for} \quad \epsilon \ll 1 \tag{2.7}$$

gives an expression for the minimum resolvable height difference in the crystallite:

$$\Delta h^{min}(\epsilon) \approx h'(\epsilon)\,\Delta\epsilon = C\,h'(\epsilon)\frac{2\pi}{R(\epsilon)Q}. \tag{2.8}$$

The above resolution element has three important features: first, the proportionality to $h'(\epsilon)$ is equivalent to an inverse proportionality to the strain gradient $\epsilon'(h)$, i.e. the faster the lattice parameter changes with height, the better is the resolution. Regarding the material properties of hetero-epitaxial systems, this corresponds to better resolutions for higher lattice mismatches. Second, the resolution element is inversely proportional to the lateral size of the iso-strain areas. Third, the resolution is better for larger Q. In summary, spatial resolution can be achieved for large enough nano-crystals with high enough lattice mismatch with respect to the substrate such that

$$\Delta h(\epsilon) < H, \tag{2.9}$$

where H is the total height of the nano-crystal.

2.2.4 Iso-strain scattering

Let us suppose the projections of the iso-strain areas on $\mathcal{P}$ have shape functions $f_{x_z}(x_r, x_a)$ where x_r is the coordinate of the radial axis along $\mathbf{Q}$ and x_a is measured along the angular direction perpendicular to it. The resulting third axis parallel to $\mathbf{p}$ is written as x_z. Without restricting the general validity, these projections can be assumed to be rectangular meshes with the primitive lattice vectors along x_r and x_a. In this section, only momentum transfers with zero components normal to $\mathcal{P}$ ($q_z = 0$) are considered for which the three-dimensional shape of the iso-strain areas is irrelevant. For the reciprocal coordinates q_r and q_a relative to the Bragg-point $\mathbf{Q}$ of the substrate, the phase sum of all lattice points integrated over all iso-strain areas stacked along $\mathbf{p}$ is

$$F\left(q_r, q_a\right) = \int \mathrm{d}x_z \sum_{\substack{(n_r,n_a)\\ \in\Omega(x_z)}} e^{i(Q+q_r)x_{n_r}(x_z)} e^{iq_a x_{n_a}(x_z)}$$

with

$$\begin{aligned} x_{n_{r,a}}(x_z) &= \big(n_{r,a} + \delta_{r,a}(x_z)\big)a_{r,a}(x_z) \\ \Omega(x_z) &= \big\{(n_r, n_a) \in \mathbb{N}^2 \,\big|\, f_{x_z}\big(x_{n_r}(x_z), x_{n_a}(x_z)\big) > 0\big\}, \end{aligned} \tag{2.10}$$

where $a_{r,a}(x_z)$ is the real space lattice parameter parallel to $x_{r,a}$ and $\delta_{r,a}(x_z)$ designates the required shift to adjust the origin of the lattice at a specified x_z (see Fig. 2.4). Since only the values of x_r are relevant for the following argument, this simple model even holds for the case of varying anisotropies. For calculations in reciprocal space, an effective reciprocal lattice parameter $g_{\mathbf{Q}} = 2\pi a_r^{-1}\sqrt{h^2+k^2+l^2}$ is used, where h,k and l are the indices pertaining to the reflection $\mathbf{Q}$.

Here, a subtle problem arises when trying to rewrite this phase sum in continuous coordinates: the origin of the coordinate system in real space

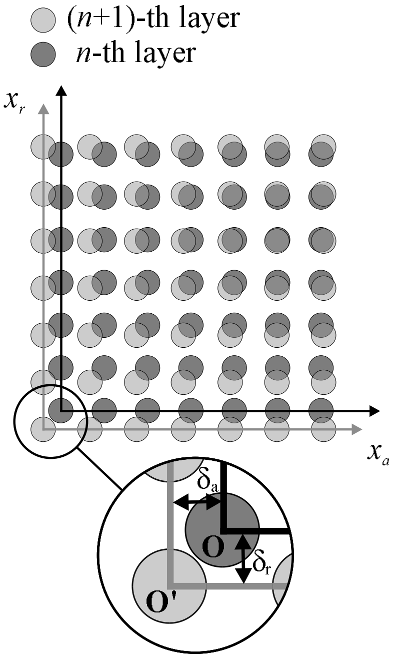

Figure 2.4: Determination of offsets in lattice origins for the discrete phase sum of two different iso-strain areas. For two subsequent layers n and $n+1$ with different lattice parameters, the origins of the lattices $\mathbf{O}$ and $\mathbf{O}'$ are subject to positional shifts δ_a and δ_r in the angular and radial directions x_a and x_r. The functional dependence of the radial shift δ_r strongly influences the intensity distribution in reciprocal space.

must be chosen and kept fixed for the whole calculation while discrete lattice points are still used. The reason for this stems from the fact that the value of x_z in Eq. (2.10) not only influences the position of the Bragg-condition along q_r for the corresponding iso-strain area, but also introduces a phase shift which depends on the alignment of lattice points in subsequent lattice planes. This information will be lost when neglecting the quantization of the lattice and has to be added to the integrals as a phase function $\phi(x_z)$ which is dependent on the origin of the discrete coordinates. Although $\phi(x_z)$ is determined by $\delta_r(x_z)$ alone, the determination of both $\delta_r(x_z)$ and $\delta_a(x_z)$ allows us to extend our result to all reflections parallel to $\mathcal{P}$ without going back to Eq. (2.10).

If there exists a line of coherence parallel to $\mathbf{p}$ along which the lattice points of different x_z are stacked with zero shifts, the origin for x_r and x_a is most conveniently chosen on this line, as $\delta_{r,a}(x_z)$ will then vanish for all values of x_z and $\phi(x_z)$ will be unity throughout the whole crystal. For the case of nano-structures which are axially symmetric with respect to $\mathbf{p}$, a symmetry argument shows that the line of coherence must coincide with the line of symmetry.

The sum in Eq. (2.10) may thus be approximated by a convolution of the form factor $\tilde{F}_{x_z}(q_r, q_a)$ of the iso-strain area at x_z with a delta function around the appropriate Bragg peak at $g_{\mathbf{Q}}(x_z) - Q$ along q_r multiplied by the phase factor $\phi(x_z)$:

$$F(q_r, q_a) = \int \mathrm{d}x_z \int \tilde{F}_{x_z}(u, q_a)\, \phi(x_z) \delta\big(u - q_r + (g_{\mathbf{Q}}(x_z) - Q)\big)\, \mathrm{d}u$$

with

$$\tilde{F}_{x_z}(q_r, q_a) = \iint f_{x_z}(x_r, x_a) e^{iq_r x_r + iq_a x_a}\, \mathrm{d}x_r\, \mathrm{d}x_a. \tag{2.11}$$

In order to simplify Eq. (2.11), it has to be noted that for a selected reciprocal coordinate q_r^0 the integral over x_z will have relevant contributions only in a certain range Δx_z around the position x_z^0 where the Bragg-condition is fulfilled. Taking eq. (2.7) into account and assuming $g_{\mathbf{Q}}(x_z)$ to be a monotonic function, the upper and lower limits for Δx_z are given by

$$\begin{aligned} x_z^{\pm} &= g_{\mathbf{Q}}^{-1}\Big(g_{\mathbf{Q}}(x_z^0) \pm C\frac{2\pi}{R(x_z^0)}\Big) \\ &\approx x_z^0 \pm C\frac{2\pi}{R(x_z^0)}\left.\frac{\mathrm{d}g_{\mathbf{Q}}^{-1}}{\mathrm{d}q_r}\right|_{q_r = g_{\mathbf{Q}}(x_z^0)} \end{aligned} \tag{2.12}$$

which gives an estimate for Δx_z:

$$\Delta x_z \approx C \frac{2\pi}{R(x_z^0)} \left(\frac{\mathrm{d}g_{\mathbf{Q}}}{\mathrm{d}x_z} \right)^{-1} \Bigg|_{x_z = x_z^0} . \tag{2.13}$$

If spatial resolution can be achieved as explained in section 2.2.3, the range given by Δx_z will be a subset of the entire range of the integration given by the size of the nano-structure.

Two approximations can now be made with respect to the relevant range of integration:

First, the shape function of the projected iso-strain area can be considered constant in Δx_z which is strictly valid if the relative variation of $R(x_z)$ in Δx_z is small compared to $R(x_z^0)$:

$$\Delta x_z \, \frac{1}{R(x_z^0)} \, \frac{\mathrm{d}R}{\mathrm{d}x_z} \Bigg|_{x_z = x_z^0} \ll 1. \tag{2.14}$$

In that case, the index x_z on $\tilde{F}$ in eq. (2.11) should be renamed to x_z^0.

Second, the reciprocal lattice parameter can be approximated as a linear function throughout Δx_z:

$$g_{\mathbf{Q}}(x_z) = g_{\mathbf{Q}}(x_z^0) + g'_{\mathbf{Q}}(x_z^0)(x_z - x_z^0). \tag{2.15}$$

In addition, the expression can be further simplified by restricting the analysis to structures which have a line of vertical coherence by choosing the origin for x_r and x_a at the line of symmetry. As discussed above, we can then set $\phi(x_z) = 1$. The scattering amplitude for these approximations is obtained as

$$F(q_r^0, q_a) = \int \tilde{F}_{x_z^0} \left(q_r - g_{\mathbf{Q}}(x_z^0) + Q + g'_{\mathbf{Q}}(x_z^0) x_z, q_a \right) \mathrm{d}x_z. \tag{2.16}$$

If the relevant range of integration Δx_z lies wholly within the nano-structure, the bounds of the x_z integration in Eq. (2.16) may be extended to infinity whereby the constant offset in the first argument becomes arbitrary and can be omitted. The resulting simplified expression is written as

$$F(q_r^0, q_a) = (g'_{\mathbf{Q}}(x_z^0))^{-1} \int \tilde{F}_{x_z^0} (u, q_a) \, \mathrm{d}u. \tag{2.17}$$

Rewriting the integral in Eq. (2.17) in terms of the real-space shape function $f_{x_z^0}$ leads to

$$F(q_r^0, q_a) = (g'_{\mathbf{Q}}(x_z^0))^{-1} \int f_{x_z^0} (0, x_a) \, e^{i q_a x_a} \, \mathrm{d}x_a. \tag{2.18}$$

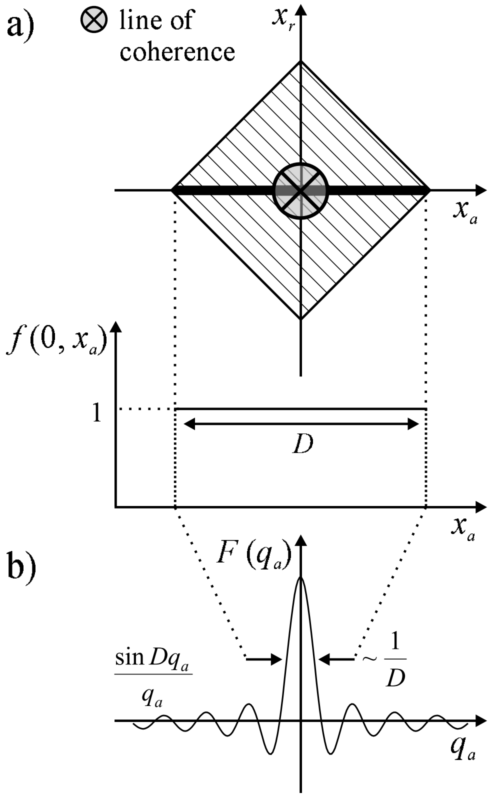

Figure 2.5: Calculation of iso-strain scattering from the real space shape function of the iso-strain areas. (a) For a cross section with the origin chosen at the line of coherence of the nano-structure, the functional dependence of iso-strain scattering in the angular direction q_a can be calculated from the linear section at $x_r = 0$. For convex cross-sections without holes, the section is a constant interval. The iso-strain form-factor $F(q_a)$ in (b) is calculated as the Fourier transform of $f(0, x_a)$ and thus shows a $\frac{\sin x}{x}$-behavior. The length D of the section can be derived from the width of the central maximum.

In summary, the angular scattering amplitude is given by the *one-dimensional* Fourier-transform of the linear section through the shape function perpendicular to $\mathbf{Q}$ and $\mathbf{p}$ (see Fig. 2.5). If the sections are single contiguous intervals of length $D_{\mathbf{Q}}(x_z^0)$, the remaining integral can be calculated as

$$F(q_r^0, q_a) = (g'_{\mathbf{Q}}(x_z^0))^{-1} \, \frac{\sin \frac{1}{2} q_a D_{\mathbf{Q}}(x_z^0)}{\frac{1}{2} q_a}. \tag{2.19}$$

The scattering intensity is thus proportional to the inverse square of the reciprocal lattice parameter gradient and falls of as q^{-2} along q_a. In summary, the lateral form factor of iso-strain scattering along q_a is determined exclusively by the section length of the two-dimensional *projection* of the iso-strain area along x_a and is independent of the actual shape of the projection.

2.3 Height resolution for nano-crystals above a surface

2.3.1 Four-process scattering

In scattering geometries of grazing incidence or exit where the angles of incidence (α_i) and exit (α_f) are comparable to the critical angle of total external reflection (α_c), the Born approximation is no longer accurate and refraction effects have to be taken into account [77]. For a plain surface, the structure factor of the sample is modulated by the product of the transmission functions

$$t_{i,f}(\alpha_{i,f}) = \frac{2 \sin \alpha_{i,f}}{\sin \alpha_{i,f} + \sqrt{\sin^2 \alpha_{i,f} - \sin^2 \alpha_c}} \tag{2.20}$$

describing the changes in field strength as the beam enters and exits the sample through the surface. For strained nano-structures on top of the surface, the optical part of the scattering process additionally includes multiple scattering between the surface and the nano-structures above it.

Since strain-driven island formation in the Stranski-Krastanow growth mode leads to nano-structures which are coherent at the substrate interface but with continuously relaxing lattice parameter towards the top, the lattice parameter values in the island are nowhere present in the substrate, apart from very small distortions. By selecting a total momentum transfer which corresponds to a certain lattice parameter in the island, one excludes Bragg scattering contributions from the substrate. In first order perturbation theory, the surface acts like a mirror, doubling the incoming and the diffracted beam as shown in Fig. 2.6.

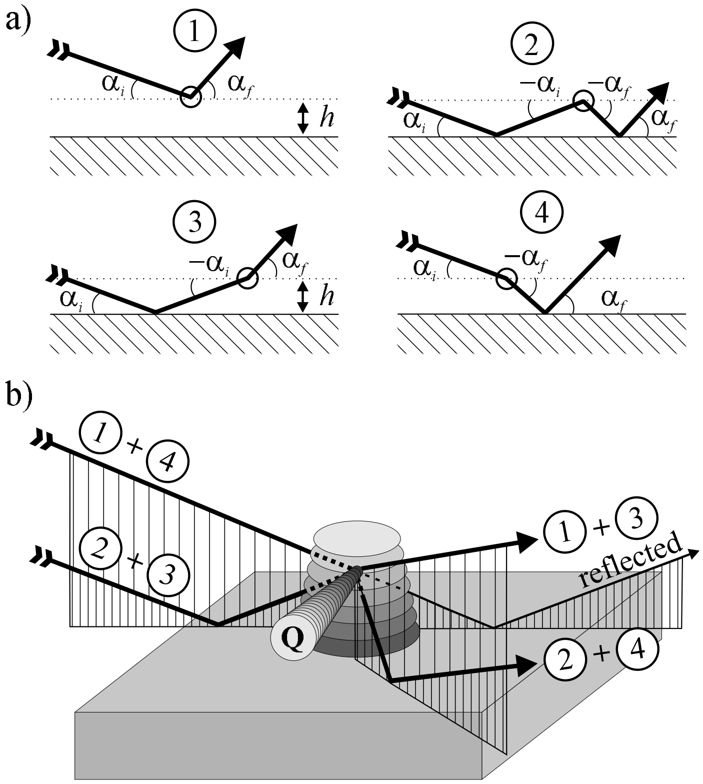

Figure 2.6: Four scattering processes from first order perturbation theory. Part (a) shows a side view of the four processes which interfere coherently and give rise to a generalized optical function for grazing incidence diffraction. The process labeled as (1) is the direct Bragg-reflection at the iso-strain area selected by the total momentum transfer **Q**. Process (2) employs two ordinary reflections from the surface before and after Bragg reflections at grazing angles of α_i and α_f respectively. The actual Bragg-scattering is denoted by a circle. Process (3) and (4) each involve one of those substrate reflections. The three dimensional beam paths are shown in part (b). The total momentum transfer **Q** which is parallel to the surface requires the diffracted beams to be deflected out of the plane of incidence.

In the following calculations involving surface reflections we fix the reciprocal coordinates q_r at an arbitrary q_r^0 and q_a at 0 and consider the dependence of the structure factor on the angles of incidence (α_i) and exit (α_f) which was set aside in section 2.2. Each scattering process has a different vertical momentum transfer q_z dependent on the angles of incidence and exit for the Bragg scattering process. Furthermore, each resulting structure factor $F^z(q_z)$ has a different relative amplitude which is given by the product of all reflectivities r involved in the particular scattering sequence. The total scattering amplitude $F_{\text{total}}(\alpha_i, \alpha_f)$ then results as

$$\begin{aligned} F^z_{\text{total}}(\alpha_i, \alpha_f) &= F^z(q_{z,1}) + r(\alpha_i) r(\alpha_f) F^z(q_{z,2}) + \\ &\qquad r(\alpha_i) F^z(q_{z,3}) + r(\alpha_f) F^z(q_{z,4}) \\ \text{with} \quad q_{z,1} &= k(\alpha_i + \alpha_f) \\ q_{z,2} &= k(-\alpha_i - \alpha_f) \\ q_{z,3} &= k(-\alpha_i + \alpha_f) \\ q_{z,4} &= k(\alpha_i - \alpha_f), \end{aligned} \tag{2.21}$$

where k is the length of the wave vector of the incoming beam.

2.3.2 Vertical structure factor in iso-strain scattering

Equation (2.21) is valid for arbitrary nano-structures above a plain surface. Including the phase factor $e^{iq_z x_z}$ for a finite q_z in Eq. (2.16) leads to an expression which is more general than Eq. (2.17):

$$F(q_r^0, q_a, q_z) = (g'_{\mathbf{Q}}(x_z^0))^{-1} e^{iq_z x_z^0} \int \tilde{F}_{x_z^0}(u, q_a)\, e^{iq_z (g'_{\mathbf{Q}}(x_z^0))^{-1} u}\, \mathrm{d}u. \tag{2.22}$$

By writing out the Fourier transforms Eq. (2.22) becomes

$$F(q_r^0, q_a, q_z) = (g'_{\mathbf{Q}}(x_z^0))^{-1} e^{iq_z x_z^0} \int f_{x_z^0}\left(\frac{q_z}{g'_{\mathbf{Q}}(x_z^0)}, x_a\right) e^{iq_a x_a}\, \mathrm{d}x_a. \tag{2.23}$$

Generalizing the notion of sections as in Eq. (2.19) to $D_{\mathbf{Q}}(x_z^0, x_a)$ so as to include an arbitrary angular distance from the line of vertical coherence, yields an expression for the structure factor for non-zero q_z:

$$F(q_r^0, q_a, q_z) = (g'_{\mathbf{Q}}(x_z^0))^{-1}\, e^{iq_z x_z^0}\, \frac{\sin \frac{1}{2} q_a D_{\mathbf{Q}}(x_z^0, q_z (g'_{\mathbf{Q}}(x_z^0))^{-1})}{\frac{1}{2} q_a}. \tag{2.24}$$

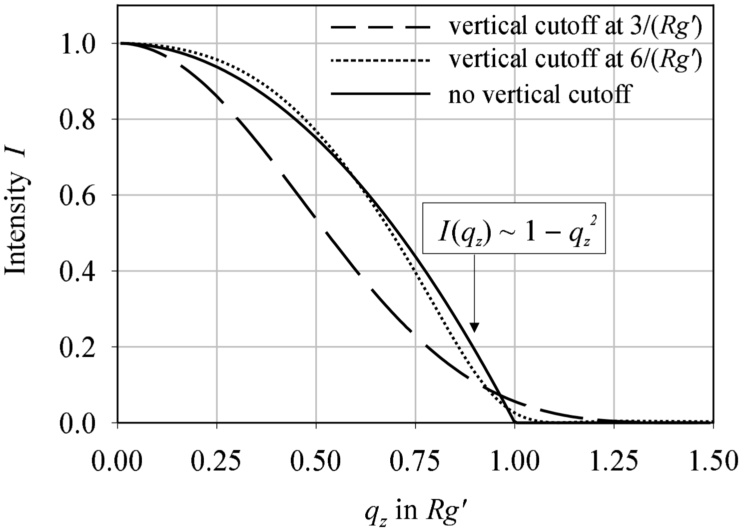

Figure 2.7: Dependence of the structure factor on q_z. The range in q_z where the structure factor is finite is determined by the product of the lateral size R and the reciprocal lattice parameter gradient g'. The figure shows the intensity resulting from the structure factor for a circular cross section. In an idealized iso-strain scattering model, the vertical structure factor traces the lateral shape (see text) which, for a circular cross section yields an intensity distribution proportional to $1 - q_z^2$. In a realistic situation the iso-strain integration cannot be extended to infinity and a vertical cutoff on either side of the iso-strain-area is introduced. Two such cutoffs are shown as the dotted and dashed lines.

The q_z-dependence of the structure factor at $q_a = 0$ is thus proportional to the variation along x_r of the shape function's section length parallel to x_a:

$$F^z(q_z) = F(q_r^0, 0, q_z) = (g'_{\mathbf{Q}}(x_z^0))^{-1}\, e^{iq_z x_z^0}\, D_{\mathbf{Q}}\left(x_z^0, \frac{q_z}{g'_{\mathbf{Q}}(x_z^0)}\right). \tag{2.25}$$

Figure 2.7 pictures this relationship for a circular cross-section. Equation (2.25) shows that $F^z(q_z)$ will be zero above a maximum value $q_z^{0,max}$ which is given by the maximum lateral extent $x_a^{0,max}$ (R in Fig. 2.7) and the reciprocal lattice parameter gradient at x_z^0 (g' in Fig. 2.7):

$$q_z^{0,max} = x_a^{0,max} g'_{\mathbf{Q}}(x_z^0). \tag{2.26}$$

Close to the lower and upper limit in x_z of the nano-structure where the iso-strain approximations fail, $F(q_z)$ will be smoothed out, especially near $q_z^{0,max}$ above which it will still yield non-zero values.

2.3.3 Generalized optical functions

Now we restrict the calculation to cases where the iso-strain areas are sufficiently large and the weighted projection of the shape function along x_a is varying slowly enough at small q_z to neglect the shape-dependence of $F(q_z)$ at angles of incidence and exit which are comparable to α_c. For cross-sections with smooth outlines near $x_r = 0$ this leads to

$$F^z(q_z) \approx e^{iq_z x_z^0} \quad \text{for} \quad q_z \simeq k\alpha_c \tag{2.27}$$

and is strictly correct when

$$\frac{1}{F^z(0)} \left.\frac{\mathrm{d}F^z(q_z)}{\mathrm{d}q_z}\right|_{q_z=0} k\alpha_c = \frac{1}{D_{\mathbf{Q}}(x_z^0, 0)} \left.\frac{\mathrm{d}D_{\mathbf{Q}}(x_z^0, q_z)}{\mathrm{d}q_z}\right|_{q_z=0} k\alpha_c \ll 1 \tag{2.28}$$

is fulfilled. If either the angle of incidence (α_i) or the angle of exit (α_f) is larger than α_c, the term with q_z^0 becomes dominant as the other three terms scale with the reflectivity of the substrate.

Inserting this approximation into Eq. (2.21) and factorizing out $e^{ik(\alpha_i+\alpha_f)x_z^0}$ the total amplitude is obtained as

$$\begin{aligned} F^z_{\text{total}}(\alpha_i, \alpha_f) = F^z\big(k(\alpha_i + \alpha_f)\big)e^{ik(\alpha_i+\alpha_f)} \times \\ \Big(1 + r(\alpha_i)r(\alpha_f)e^{-2ik(\alpha_i+\alpha_f)x_z^0} + r(\alpha_i)e^{-2ik\alpha_i x_z^0} + r(\alpha_f)e^{2ik\alpha_f x_z^0}\Big). \end{aligned} \tag{2.29}$$

By factorizing the parentheses in Eq. (2.29) one can now separate the dependencies on α_i and α_f which are found to be identical. This relationship can thus be expressed as

$$\begin{aligned} F^z_{\text{total}}(\alpha_i, \alpha_f) &= F^z\big(k(\alpha_i + \alpha_f)\big)\, t^{\text{fps}}(\alpha_i, x_z^0)\, t^{\text{fps}}(\alpha_f, x_z^0) \\ \text{with} \quad t^{\text{fps}}(\alpha, z) &= 1 + r(\alpha)e^{-2ik\alpha z}. \end{aligned} \tag{2.30}$$

The functional form of the total amplitude F^z_{total} is now analogous to the case of a flat surface with F^z derived in section 2.3.2 assuming the role of the structure factor and t^{fps} as a generalized optical function in place of the transmission function, with t^{fps} including the effects of the four-process scattering (fps). Indeed, for $z = 0$ one finds that

$$t^{\text{fps}}(\alpha, 0) = 1 + r(\alpha) = t(\alpha) \tag{2.31}$$

is the same function as in Eq. (2.20).

For a discussion of the scattered intensity the absolute square of t^{fps} is analyzed:

$$\begin{aligned} I^{\text{fps}}(\alpha,z) &= \left|t^{\text{fps}}(\alpha,z)\right|^2 \\ &= \left(1+r(\alpha)e^{-2i\alpha z}\right)\left(1+r^*(\alpha)e^{2ik\alpha z}\right) \\ &= 1+\left|r(\alpha)\right|^2+2\Re\big(r(\alpha)\big)\cos 2k\alpha z+2\Im\big(r(\alpha)\big)\sin 2k\alpha z. \end{aligned} \tag{2.32}$$

At this point it is convenient to continue with the reduced coordinates

$$\hat{\alpha}=\frac{\alpha}{\alpha_c}; \qquad \hat{z}=k\alpha_c z. \tag{2.33}$$

Since α is of the order of α_c, which is typically a few mrad, the reflectivity and the transmittivity are usually written as

$$\begin{aligned} r(\hat{\alpha}) &= \frac{\hat{\alpha}-\sqrt{\hat{\alpha}^2-1}}{\hat{\alpha}+\sqrt{\hat{\alpha}^2-1}} \\ t(\hat{\alpha}) &= \frac{2\hat{\alpha}}{\hat{\alpha}+\sqrt{\hat{\alpha}^2-1}}, \end{aligned} \tag{2.34}$$

not taking roughness effects into account. Due to the square root in Eq. (2.34) there are two regimes for $\hat{\alpha}<1$ and $\hat{\alpha}>1$ which have to be dealt with separately.

For $\hat{\alpha}<1$ in Eq. (2.34), it is convenient to separate real and imaginary parts by taking $(-i)$ out of the square roots in r:

$$r(\hat{\alpha})=\left(2\hat{\alpha}^2-1\right)+i\left(2\hat{\alpha}\sqrt{1-\hat{\alpha}^2}\right). \tag{2.35}$$

Evidently, $\left|r(\hat{\alpha})\right|^2=1$ and therefore

$$I^{\text{fps}}(\hat{\alpha},\hat{z})=2+2\left(2\hat{\alpha}^2-1\right)\cos 2\hat{\alpha}\hat{z}+4\hat{\alpha}\sqrt{1-\hat{\alpha}^2}\,\sin 2\hat{\alpha}\hat{z}. \tag{2.36}$$

The angle of maximum intensity $\hat{\alpha}^{max,1}$ in Eq. (2.36) is implicitly given by (see Appendix C)

$$\hat{\alpha}^{max,1}=\cos\hat{\alpha}^{max,1}\hat{z}. \tag{2.37}$$

For the case of an iso-strain area where the Bragg-scattering only occurs at a certain height above the sample's surface, one can measure the maximum and determine the height z from

$$z=\frac{1}{k\alpha^{max,1}}\arccos\frac{\alpha^{max,1}}{\alpha_c}. \tag{2.38}$$

Beyond the critical angle ($\hat{\alpha} > 1$), the generalized optical function is a harmonic oscillation of period $2\hat{z}$ whose amplitude decays as $\hat{\alpha}^{-1}$ on top of a background which asymptotically decays towards unity as $\hat{\alpha}^{-2}$:

$$I^{\text{fps}}(\hat{\alpha}, \hat{z}) = 1 + \frac{2\hat{\alpha}^2 - 1 - 2\hat{\alpha}\sqrt{\hat{\alpha}^2 - 1}}{2\hat{\alpha}^2 - 1 + 2\hat{\alpha}\sqrt{\hat{\alpha}^2 - 1}} + 2\frac{\hat{\alpha} - \sqrt{\hat{\alpha}^2 - 1}}{\hat{\alpha} - \sqrt{\hat{\alpha}^2 - 1}} \cos 2\hat{z}\hat{\alpha}. \tag{2.39}$$

The position of the first maximum of the oscillatory part $\alpha^{max,2}$ thus also gives the height z of the iso-strain area,

$$z = \frac{\pi}{k\alpha^{max,2}}. \tag{2.40}$$

Figure 2.8 shows how the maximum of the classic transmission function at $\hat{z} = 0$ at $\hat{\alpha} = 1$ shifts to lower $\hat{\alpha}$ for larger $\hat{z}$. As the sharp transmission

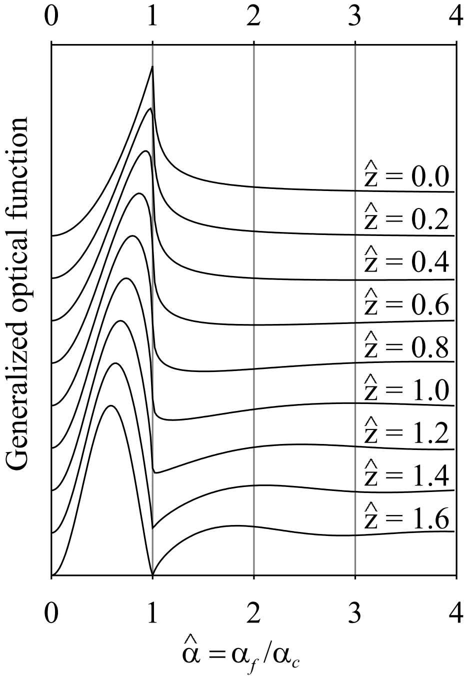

Figure 2.8: Generalized optical functions for various reduced heights $\hat{z}$. The sharp maximum at $\hat{z} = 0$ is seen to move to smaller angles $\hat{\alpha}$ for increasing $\hat{z}$, at the same time assuming a broader and symmetric shape. Near $\hat{z} = \frac{\pi}{2}$ the intensity is modulated to zero. The oscillatory behavior in the range $\hat{\alpha} > 1$ which becomes apparent for $\hat{z} > 1$ is due to the intuitive 'mirror effect' of an iso-strain area above a reflecting surface.

peak is smoothed and broadened, a minimum starts to form at $\hat{\alpha} > 1$ moving towards lower angles together with the first pronounced maximum. In fact, at $\hat{\alpha} = 1$, where a strong maximum is expected for traditional grazing incidence diffraction, the absolute square of the generalized optical function

$$I^{\text{fps}}(1, \hat{z}) = 2\,(1 + \cos 2\hat{z}) \tag{2.41}$$

falls to zero for $\hat{z} = \frac{\pi}{2}$.

2.4 Experimental considerations

In order to combine the analytical techniques described in sections 2.2 and 2.3, a grazing incidence and exit scattering geometry [38,78] is most appropriate (Fig. 2.9). In this case, the total momentum transfer lies predominantly in the plane of the sample's surface. The direction **p** which can be thought of as the stacking direction for the projected iso-strain areas is then parallel to the surface normal, i.e. the direction in which stress in heteroepitaxial systems can be relieved by means of strain. For centro-symmetrical islands,

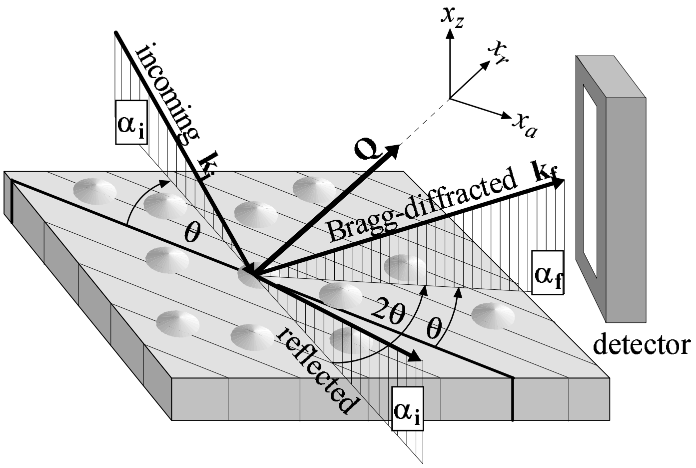

Figure 2.9: Scattering geometry for grazing incidence and exit. Both the angle of incidence α_i and the angle of exit α_f are close to the critical angle of total external reflection α_c. Diffraction takes place on lattice planes which are perpendicular to the sample's surface. The intensity is measured by a position sensitive detector which records α_f-spectra.

this configuration has the added advantage that the line of symmetry is also parallel to **p** and can be taken as the origin for the lateral coordinates x_r and x_a. Furthermore, for angles of incidence and exit below the critical angle of total external reflection, the penetration depth of the evanescent x-ray beam below the surface is of the order of 5-10 nm [79], maximizing the relative scattering power of the dots with respect to the substrate.

The applicability of the presented analytical methods is limited by the size and strain gradient of the islands and their functional dependencies on the height above the surface. If the lateral size R becomes too small, the fundamental requirement of spatial distinction described in section 2.2.1 breaks down. Likewise, if the strain gradient g' is too small, the insufficient spreading in reciprocal space will prohibit the differentiation of spatial regions. For a given height H of the island, these prerequisites can be commonly expressed as a rule of thumb:

$$\eta = Rg'H \gg 1. \tag{2.42}$$

The dimensionless system constant η thus quantifies the goodness of the iso-strain approximation. For a typical system of lateral size 50 nm, exhibiting a lattice parameter difference of 5% along a height of 10 nm and a measurement at a total momentum transfer of 4 Å^{-1}, η has a numerical value of 100.

For too small R, the system enters the size-regime of atomic defects which has its own methods for the analytical treatment of the scattering intensity [80]. For too small g' at large R, the strain effects are best treated as corrections to the strainless case. While the values of R and H are fixed for a particular system, the numerical value of g' can be increased by choosing a higher order reflection.

The determination of heights with Eq. (2.38) has different accuracies for small and large values of $\hat{z}$. While the deviation of the first pronounced maximum is substantial for values of $\hat{z} > 0.2$, for values smaller than that, a highly accurate knowledge of the critical angle α_c and a good resolution in α_f is required. Equation (2.40) on the other hand, shows a reciprocal behaviour to Eq. (2.38) where the accuracy is high for small $\hat{z}$ and low for large $\hat{z}$. However, the rapidly decaying amplitude of the oscillatory part in Eq. (2.39) and the decaying structure factor derived in section 2.3.2 are unfavorable for the experimental determination of this maximum.

Realistic iso-strain areas will not be flat but curved. Although this fact does not constitute a problem for the iso-strain scattering formalism presented in section 2.2.4, the determination of height in section 2.3.3 is based on a single height z above the surface. If the vertical extent introduced by the curvature is small compared to the height z of the iso-strain area under consideration, it can be neglected. However, also for substantial curvatures, the shift of the first pronounced maximum of the generalized optical function in Eq. (2.32) describes a mean weighted height of the iso-strain area.

All calculations in sections 2.2 and 2.3 neglect the variation of lateral size R and strain gradient g' within the relevant range of integration Δx_z as defined in Eq. (2.13). In general, these assumptions may not be very well fulfilled, with values for Δx_z up to 0.5 still describing realistic situations. These deviations from the idealizations leading to Eqs. (2.19) and (2.38) result in an averaging over the parameters R and g'. Thus, even while the scatterered intensity may not be closely traced by the theoretical curves, the main features will stand out and mean values of R, g' and z can be obtained.

A different approach, which makes use of finite element calculations of the entire dot in order to simulate the scattering intensity [66] is less analytic but more synthetic. This method has the advantage of being applicable to *any* vertical and lateral concentration profile, but gives relatively little insight into the interdependence between real space structure and scattered intensity distribution. The approach presented here, on the other hand, provides a *physical understanding* of the relationship of strain-related phenomena in real and reciprocal space.

2.5 Results and Discussion

2.5.1 Synopsis of iso-strain scattering

Figure 2.10 recapitulates the essential ideas presented in sections 2.2 and 2.3 without focusing on the technical ascpects of the derivation: By identifying key features of the x-ray intensity distribution in reciprocal space, one can directly reconstruct the geometry as well as the distribution of local lattice parameter and material composition. Thus, a transformation of scattering data from quantum dots to nanometer-scale tomographic images is achieved. This transformation from reciprocal space to real space is possible for the presented class of nano-structures, provided that two fundamental conditions regarding the resolution of strain and height are fulfilled:

(i) If the lattice parameter varies monotonically by a few percent across the extent of a crystallite whose dimensions are of the order of 10 nm (Fig. 2.10a), the intensity distribution will be spread out over a fairly large region of reciprocal space about the substrate reflection. Thus, one may think of the intensity at each point as attributed to a region of constant lattice parameter, i.e. to a slice through the quantum dot at a

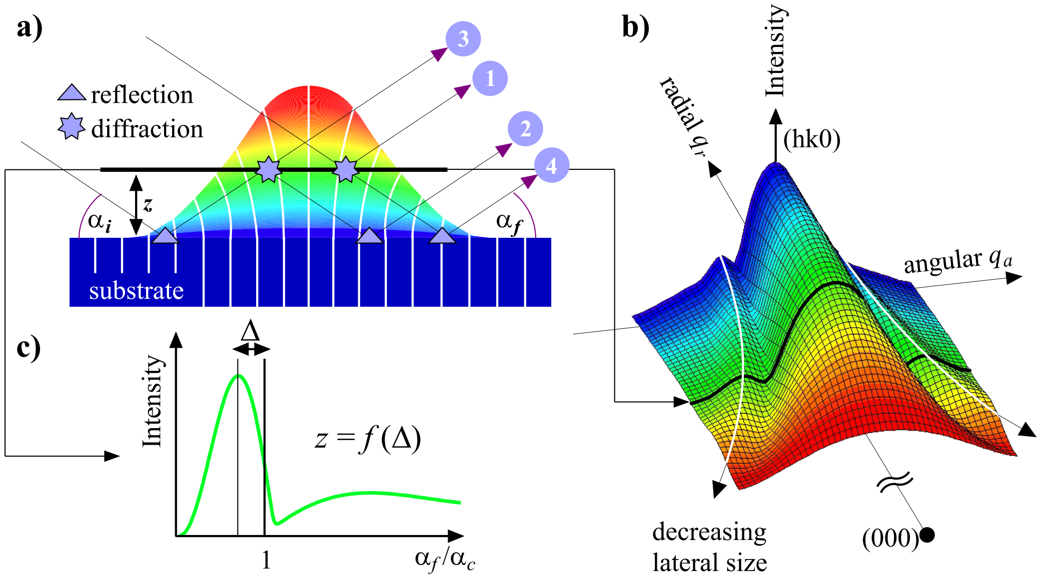

Figure 2.10: Schematic representation of the methodical approach of iso-strain scattering. Part (a) shows the scattering processes for a particular region of constant lateral lattice parameter at a height z above the substrate (the vertical lines indicate lattice planes). The diffraction processes deflect the beam out of the plane of the paper, while reflection processes alone cannot change the azimuth of beam propagation. Angles of incidence (α_i) and exit (α_f) as well as lattice distortions are greatly exaggerated. The color scale of the dot corresponds to a distribution of lattice parameters. A simulated intensity distribution for a section through reciprocal space close to a surface Bragg-reflection (hk0) is shown in (b). The color scale indicates the origin of the scattered intensity in (a). The dependence of lateral extent on lattice parameter is reflected in the width of the central maximum and the positional variation of the side maxima as denoted by the white lines. Part (c) shows the simulated α_f-spectrum corresponding to the iso-strain area at the selected height z (α_c is the critical angle of total external reflection). The numerical value of z is calculated from the maximum position α_f^{max}.

certain height interval. This pseudo-resolution introduced by the variation of lattice parameter effectively decomposes the scattering from the dot into the contributions from its iso-strain areas (Fig. 2.10b).

(ii) The dots must be free-standing: the presence of a free surface around the dots serves as a reference level against which the mean height of the iso-strain areas within the dots can be evaluated. At very small angles of incidence (α_i) and exit (α_f) close to the critical angle of total external reflection (α_c), the surface serves as a beam multiplier, giving rise to the four different scattering processes shown in Fig. 2.10a. The diffraction process, which takes place at the iso-strain area, selected by the total momentum transfer, may be combined with the two additional reflection processes before and/or after diffraction. The coherent sum of these four amplitude terms causes distinct features in the spectra along the exit angle (α_f), from which the mean height above the substrate can be directly calculated with sub-nm accuracy (Fig. 2.10c).

2.5.2 Samples

Two sample series A and B with varying growth temperature and a single specimen C were available for experimental investigations. Chronologically, sample C served as the testbed for the applicability of the methodic approach, while series A and B were grown subsequently to study the origin of the unusual material composition found as a results of the analysis of sample C. Sample labels and growth temperatures are summarized in table 2.1.

Samples in series A* were grown by solid source molecular beam epitaxy (MBE) on semi-insulating GaAs(001) substrates. First a 200 nm GaAs buffer layer and AlAs/GaAs (2 nm/10 nm) short period superlattice were grown to obtain a smooth growth surface. This was followed by a 150 nm GaAs layer grown at 600° C. The sample temperature was then reduced to the InAs island growth temperature (450° C to 530° C) as determined by using a pyrometer. Once at growth temperature, the InAs islands were formed using alternating beam epitaxy (ABE). Island formation was monitored by reflection high energy electron diffraction (RHEED). Immediately after formation of the InAs islands the substrate temperature was reduced. As shown by atomic force microscopy, the chosen growth conditions lead to rotationally symmetric quantum dots, with a random lateral arrangement of dot positions. Dislocations are not expected for this range of growth parameters.

---

*series A was grown by W. Schoenfield (group of P. Petroff) at the Materials Department at the University of California in Santa Barbara, CA 93106, USA

temperature	series A	series B	series C
530° C	A1	B1	C
500° C	A2	B2	
475° C	A3	B3	
450° C	A4	B4	

Table 2.1: List of investigated sample series. All samples were grown by MBE and show uncapped InAs islands on GaAs(001) substrates. Sample C is a specimen from a series without temperature variation.

Samples in series B* were grown under similar conditions as a reference for series A. Contrary to the procedure used for series A, the total coverage of InAs was not determined by the 2D–3D growth transition [16, 81], but was nominally set at a fixed value of 2.3 monolayers for all samples. Both in series A as well as in series B, the dot density was strongly temperature dependent [82] increasing by one order of magnitude from 10^{11} cm^{-2} at 530° C to 10^{10} cm^{-2} at 450° C. As shown by atomic force microscopy [26], these growth conditions lead to rotationally symmetric quantum dots, with a random lateral arrangement of dot positions.

Finally, for sample C†, a nominal total of 1.9 monolayers of InAs was deposited at a substrate temperature of 530° C. In and As were deposited alternatingly: the In shutter was opened for 4 s, followed by a growth interruption of 2 s under an As beam equivalent pressure of $1 \cdot 10^{-5}$ Torr. One such cycle resulted in a deposition of 0.15 monolayers of InAs. The transition from 2D to 3D growth was observed in situ by RHEED at 1.7 monolayers. Transmission electron microscopy investigations on sample C clearly showed no evidence for dislocations, as expected for these growth parameters.

2.5.3 Results of iso-strain scattering

All measurements have been performed at the TROÏKA II beamline at the European Synchrotron Radiation Facility (ESRF) in Grenoble at a wavelength of 1.5 Å. Here, results are shown from measurements between the (220)-reflections of GaAs and InAs, where three-dimensional mappings of reciprocal space are performed (Fig. 2.11). To this end, a position sensitive

---

[*] series B was grown by M. Arzberger (group of G. Abstreiter) at the Walter Schottky Institut at the Technische Universität München, Am Coulombwall, D-85748 Garching

[†] sample C was grown by J. García at the UCSB (see series A)

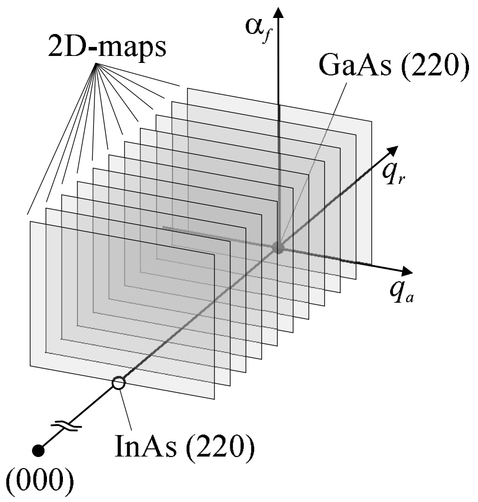

Figure 2.11: Three-dimensional mapping of reciprocal space between the (220) surface reflections of GaAs and InAs. The coordinate system is formed by two reciprocal coordinates q_r (radial) and q_a (angular) which are parallel to the real space coordinates x_r and x_a shown in Fig. 2.9 and the angle of exit α_f. The three-dimensional map is composed of two-dimensional maps in the (q_a, α_f)-plane for different values of q_r. In qualitative terms, q_r is a measure of lattice parameter, q_a shows effects of lateral shape while the α_f-direction reveals height and curvature of the iso-strain areas.

detector (see Fig. 2.8) records α_f-spectra in angular scans along q_a which are repeated at successive radial positions q_r. Each value of q_r corresponds to a different strain state. Given that the iso-strain approximations presented in section 2.2 are valid (see section 2.4), only the close vicinity of the selected iso-strain area contributes to the scattering intensity at this point. The scattering from this tiny portion of the near-surface parts of the sample is detectable due to the diffraction condition which effectively blinds out all other strain states. The electromagnetic field was additionally constrained to the near-surface region by choosing an incident angle of 0.2°, well below the critical angle of total external reflection at 0.28°. The figures in the exemplary discussion of the analysis are taken from sample A1.

Each angular scan of a three-dimensional mapping results in a two-dimensional reciprocal space map (RSM) as those shown in Fig. 2.12. The analysis of the scattering intensity proceeds by evaluating three different aspects of

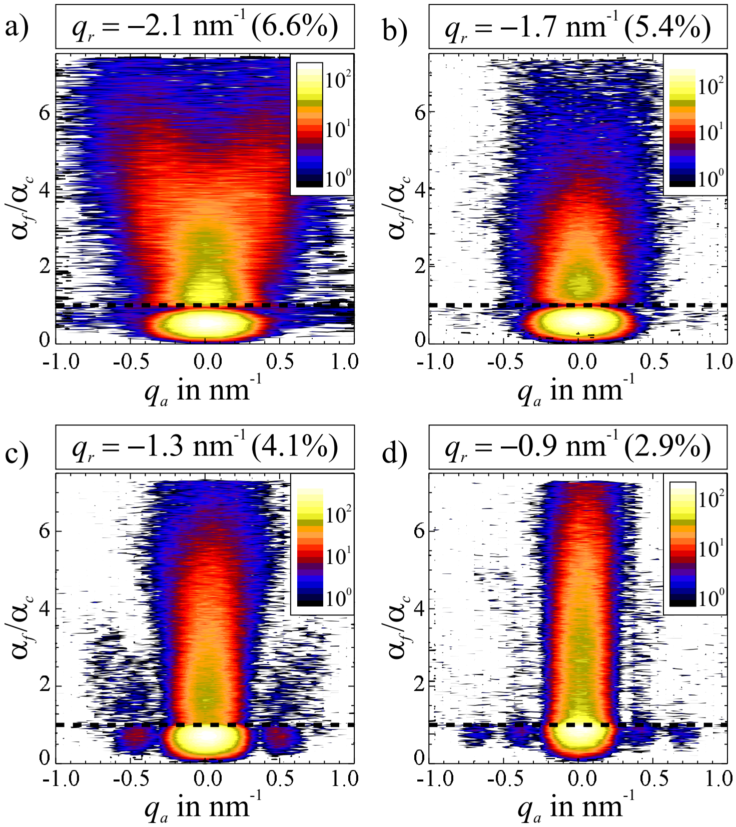

Figure 2.12: Four exemplary two-dimensional reciprocal space maps in the (q_a, α_f)-plane (sample A1). The collection of 16 such maps constitutes the three-dimensional map of reciprocal space between the two reflections of GaAs and InAs. The four maps display increasing values of q_r which corresponds to a decreasing lattice parameter difference between the selected iso-strain area and the substrate. The difference in percent is given in parentheses after the value of q_r. Clearly visible features are the narrowing of the central maximum at $\alpha_f < \alpha_c$ with decreasing lattice parameter difference corresponding to an increase in the lateral size of the dot towards the substrate and the increase of the α_f-position of the global maximum which indicates lower heights for decreasing strain.

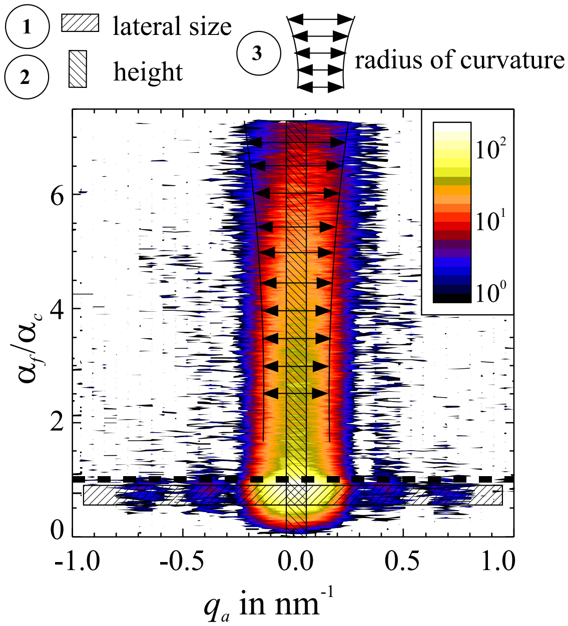

Figure 2.13: Visualization of the three-step analysis of the reciprocal space map shown in Fig. 2.12d. The lateral size of the strain state selected by q_r is extracted from the intensity distribution along the horizontal slice (step 1). Analysis of the vertical slice yields the mean height of the iso-strain area above the substrate (step 2). The radius of curvature is extracted from the dependence of the half widths in q_a on $\frac{\alpha_f}{\alpha_c}$ (step 3).

the RSMs for each radial position q_r which are visualized in Fig. 2.13. An exemplary evaluation of the RSM in Fig. 2.12d is shown in Fig. 2.14. First, the angular variation of the scattering intensity integrated for α_f up to α_c (Fig. 2.14a, step 1 in Fig. 2.13) is fitted using Eq. (2.19) yielding the lateral size of the iso-strain area. In the present case of axially symmetric islands, this corresponds to the radius of the circular projection of the iso-strain area. Second, the mean height of the iso-strain area above the surface is determined from the position of the first pronounced maximum of the scattering intensity along α_f (Fig. 2.14b, step 2 in Fig. 2.13). To improve statistics, for each value of α_f the RSM is integrated along q_a in the range of the central maximum. The numerical value of the height z is calculated using Eq. (2.38). In order to obtain an estimate for the curvature of the iso-strain areas, the half-width of the central maximum along q_a is plotted as a function of α_f (Fig. 2.14c, step 3 in Fig. 2.13). The variation in curvature due to the lateral shape as

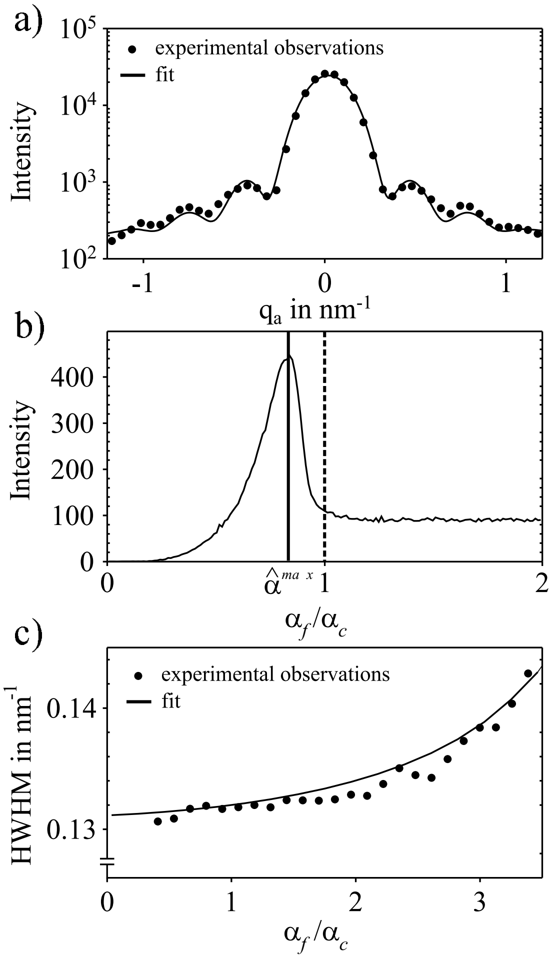

Figure 2.14: Results of the three-step analysis of the reciprocal space map shown in Fig. 2.12d. Part (a) shows the determination of lateral size using the $\frac{\sin x}{x}$-law of Eq. (2.19) (step 1 in Fig. 2.13). Allowing for a size distribution of a few percent, the functional dependence is well followed. The height of the iso-strain area is determined in (b). The position of the optical maximum at $\hat{\alpha}^{max}$ differs from 1 as would be expected for grazing incidence diffraction on planar surfaces. The actual height is then calculated from Eq. (2.38) (step 2 in Fig. 2.13). The curvature fit is displayed in (c). Here, the half widths of the central maximum for different values of α_f are fitted with a hollow sphere of variable radius of curvature (step 3 in Fig. 2.13).

given by Eq. (2.24) typically accounts to less than 20% of the total change in half-width and has to be substracted. The remaining variation in half-width is compared to that of a hollow spherical segment with the base radius taken from the first step. The radius of curvature is then varied to achieve an optimum correspondence with the experimental data. This last step is not generalizable for arbitrary shapes but depends on the actual shape model.

Figure 2.15 shows the experimental α_f-dependencies and the calculated generalized optical functions using Eq. (2.32). The optical functions are seen to dominate the low part of the α_f-spectrum while the intensities for larger values of α_f can only be explained by including the vertical structure factor from Eq. (2.24) together with corrections for size distribution and curvature. However, the essential information – the height of the iso-strain area – is extracted from the first maximum alone, eliminating the need for complex fitting procedures.

Until recently, the picture of island formation in Stranski-Krastanow growth was restricted to the epitaxially deposited phase forming islands without interdiffusion taking place. Recent experiments [83–86], however, suggest that this picture may be too simple and growth parameters such as temperature, flux rates and flux ratios [87–89] are of crucial importance. Information on the chemical composition within the islands can be obtained by comparing the intensities from radial scans along q_r for a pair of strong and weak reflections [90], such as (400) and (200) in the zinc-blende structure of InAs and GaAs. The difference of the atomic numbers of Ga and As is 2 while In has 16 more electrons than As. Since the scattering intensity for the (200)-reflection in the zinc-blende structure scales as the difference of the atomic form factors, which in turn are roughly proportional to the number of electrons, the InAs (200)-reflection will be about 64 times stronger than the GaAs (200)-reflection. This contrast can be used to determine the concentrations of Ga and In in alloys. The measured quantity is the intensity ratio from the (400) and (200) reflections

$$p(q_r) = \left| \frac{c_{In}(q_r) F^{400}_{InAs} + c_{Ga}(q_r) F^{400}_{GaAs}}{c_{In}(q_r) F^{200}_{InAs} + c_{Ga}(q_r) F^{200}_{GaAs}} \right|^2 \tag{2.43}$$

where $c_{In}(q_r)$ and $c_{Ga}(q_r)$ are the average concentrations of In and Ga for the particular iso-strain area selected by q_r and $F^{400/200}_{GaAs/InAs}$ are the structure factors of InAs an GaAs at the (400) and (200) reflections. Together with the constraint $c_{In}(q_r) + c_{Ga}(q_r) = 1$, Eq. (2.43) can be resolved for $c_{In}(q_r)$. The calculation is straightforward but due to the complex nature of the structure factors the final result is a long expression and is derived in Appendix D. The experimental curves are displayed in Fig. 2.16.

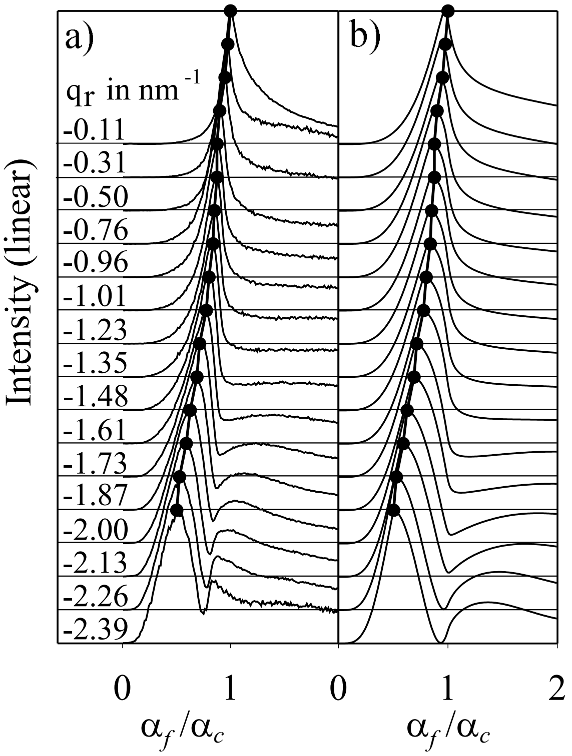

Figure 2.15: Comparison of experimental α_f-spectra with corresponding calculations of the generalized optical functions. The height determined from the experimental spectra in (a) is used as the single parameter for the calculation of the theoretical optical functions in (b) which are drawn with the same vertical offsets as in (a). The qualitative features are well reproduced, a detailed functional conformity, however, cannot be expected due to the non-planar nature of the iso-strain areas, especially for smaller values of q_r. The thick lines connect the positions of the first pronounced maxima which are the basis of the height calculation as shown in Fig. 2.14b. Further noticeable matching features are the dip in intensity which develops at larger heights around the critical angle and the occurrence of a broad second maximum which moves towards lower angles for larger heights.

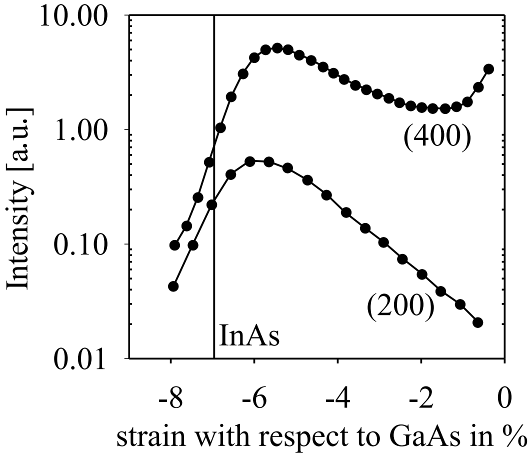

Figure 2.16: Radial intensity distributions along q_r for a strong (400) and a weak (200) reflection. Instead of q_r, the corresponding strain with respect to GaAs is chosen as the axis to make both reflections comparable. The material composition of each iso-strain area is determined by the intensity ratio of both curves. The fact that the (200) intensity is getting weaker with respect to the (400) curve for smaller lattice parameter differences to the substrate shows immediately that the Ga content is larger at the bottom of the islands.

The generalized optical function derived in Eq. (2.32) not only influences the intensity distribution along α_f but through an indirect mechanism also that along q_r. For one fixed q_r, i.e. one particular iso-strain area, the influence of α_i and α_f factorize. The analysis of the α_f-spectra as shown in Fig. 2.15 is therefore independent of the particular value of α_i. However, different values of q_r correspond to different heights z. Hence, the optical function varies along the radial direction. If the value of α_i is below the critical angle of the substrate α_c, there may be a certain height z and a corresponding radial position q_r where the optical function has its maximum exactly at α_i. Around that q_r, the intensity will be enhanced and may even lead to a local maximum. Such a maximum can be easily mistaken as a prevalent strain state in the strain distribution, hence care has to be taken to single out the optical effects. The maxima in Fig. 2.16 thus carry little useful information and a successful measurement requires extreme accuracy in the adjustment of the angles of incidence for both reflections. Figure 2.17 shows the dependence of the functional form of the radial scan on the value of α_i. As α_i approaches α_c, the maximum induced by the optical function of α_i vanishes entirely.

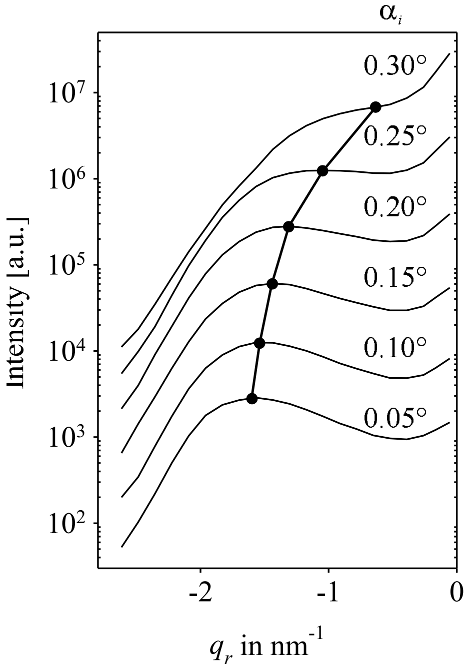

Figure 2.17: Measured radial scans along q_r for various values of α_i showing an indirect influence of the generalized optical function defined in Eq. (2.32). Both α_i and α_f are constant for each scan. As the angle of incidence α_i is decreased, the local maxima connected by the thick line shift to smaller values of q_r. This behavior can be explained as an interaction of the optical functions of α_i and α_f.

The final result of the analysis for series A is displayed in Fig. 2.18 where lateral size R, height z, radius of curvature R_K, and the concentration of Ga c_{Ga} are plotted as functions of lattice parameter difference with respect to the GaAs substrate. Since all of these functions are monotonic, a unique relationship can be established between any of theses quantities. As seen in atomic force microscopy measurements (AFM), the samples grown at 475° C and 450° C exhibit large relaxed clumps in addition to the small coherent islands which are the principal objects of interest. Beyond a certain strain, the scattering intensity is dominated by the relaxed chunks and the contribution of the coherent islands is no longer resolvable. The maximum strains reported in Fig. 2.18 were chosen at discontinuities of the height functions which in both cases exhibit a small interval of negative slope beyond those values of q_r.

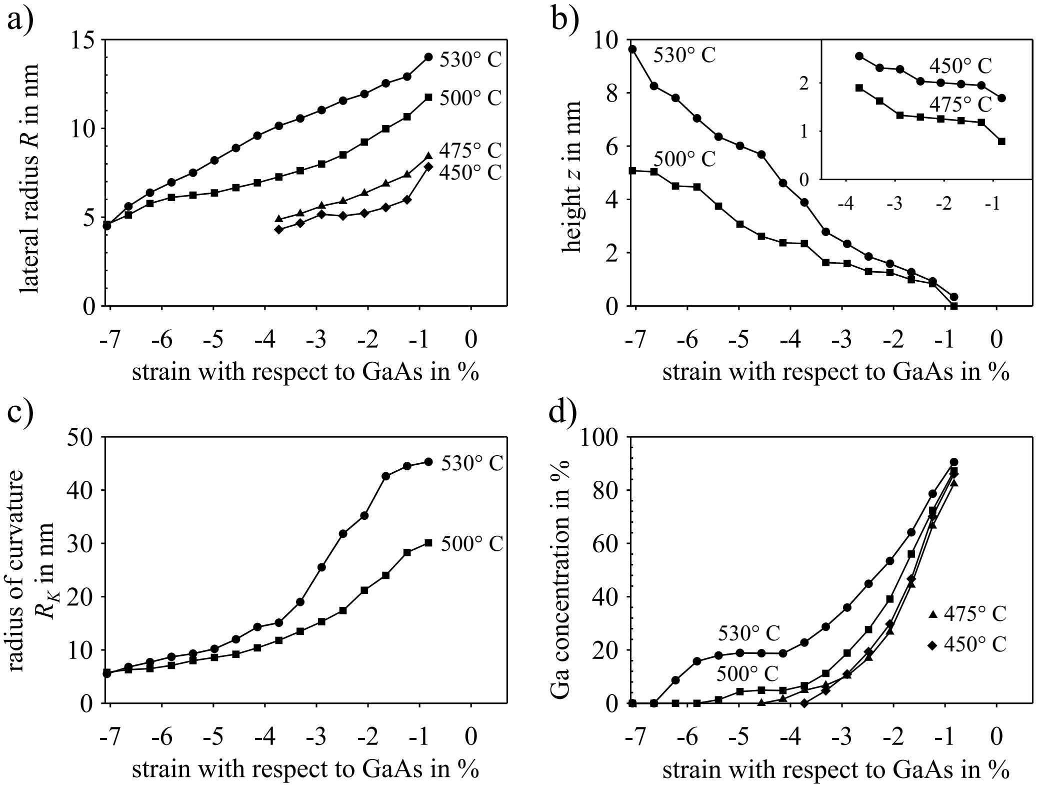

Figure 2.18: Results for lateral size, height, curvature and composition as functions of strain relative to the GaAs substrate for all four samples of series A discussed in the text. The curves for 475° C and 450° C are incomplete due to large relaxed clusters which prohibit any evaluation for larger strain states. Lateral size in (a) and height in (b) are seen to decrease with temperature while retaining similar functional dependencies on strain. Also, radius of curvature in (c) and Ga concentration in (d) show a monotonic decrease with decreasing temperature.

The fact that the heights for the samples grown at 530° C and 500° C saturate at a strain which corresponds to the lattice parameter of InAs, shows that the tops of these islands are covered with pure InAs. The lateral sizes decrease with decreasing temperature [91] and are compatible with AFM pictures. As the most important result, the Ga-concentration in the dots is increasing markedly with increasing growth temperature.

Finally, the information contained in the four graphs of Fig. 2.18 can be used to draw real space tomographic images of the islands. Figure 2.19 show the strain and Ga-distributions for samples A1 and A2 grown at 530° C and 500° C where complete data sets are available. It has to be noted that the images do not show iso-concentration areas but iso-strain areas with

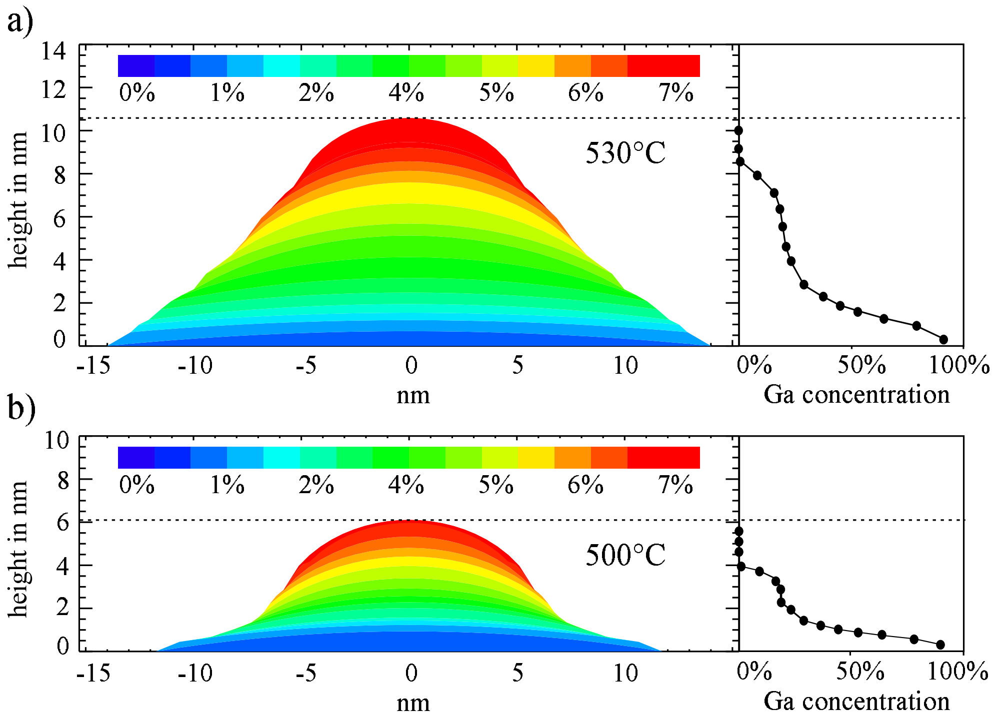

Figure 2.19: Tomographic images for samples A1 and A2 grown at 530° C (a) and 500° C (b). The color coding ranges from 0% lattice parameter difference at the bottom of the islands to 7% strain with respect to GaAs at the top. The Ga concentration is displayed as a function of height on the right side of each image. The dots grown at 500° C are markedly smaller than those grown at 530° C and show a reduced Ga concentration.

their mean Ga-concentration displayed on their right side. The atomistic calculations presented in section 2.5.4 show that starting with planar iso-concentration areas, the experimentally found curvatures of the iso-strain areas can be fully explained.

The results from series B are qualitatively similar to those of series A, but differ in two respects:

(i) Contrary to samples A3 and A4, no large dislocated islands are found for the corresponding samples B3 and B4. The whole range in reciprocal space between GaAs and InAs shows the continuous characteristics of a single type of islands which are coherent to the substrate. Hence, the entire dot and not just the lower part of the islands are analyzable with iso-strain scattering.

(ii) The heights of the iso-strain areas of samples B2, B3 and B4 cannot be successfully evaluated using Eq. (2.38). This is due to two factors:

   (a) Since samples B2, B3 and B4 do not display side maxima as in the predicted intensity distribution proportional to $\frac{\sin x}{x}$ (see Fig. 2.5), the size distribution in these samples is appreciable and broadens the range of heights for each iso-strain area.

   (b) The fixed total InAs coverage of 2.3 monolayers seems to result in too large island densities [92] for temperatures smaller than 530° C to be evaluated with the formalism presented in section 2.3. In these cases, the uncovered area is too small for Eq. (2.28) to hold. In addition, the specific form of inter-dot correlations would have to be considered.

Therefore, only for sample B1 grown at 530° C a tomographic image can be drawn (Fig. 2.20), the functional dependencies of size and composition on the relative lattice parameter difference with respect to GaAs are shown in Fig. 2.21 for all samples of series B.

Figure 2.22 shows the results for sample C, which, although from a different series, is very similar to samples A1 and B1, indicating that for size and composition, temperature is a dominant growth parameter.

These findings confirm and add a spatially resolved strain mapping to previous results on inter-diffusion where the In content is enriched [7, 83, 93] or reduced [84, 94, 95], depending on the composition of the epitaxially deposited material. Preliminary Rutherford Back Scattering experiments indicate that Ga diffuses no deeper than 15 nm into the substrate. Possibly, the actual value is much lower. Ga may thus be transported into the dot by surface kinetics [96, 97]. Although the mechanism of Ga-incorporation

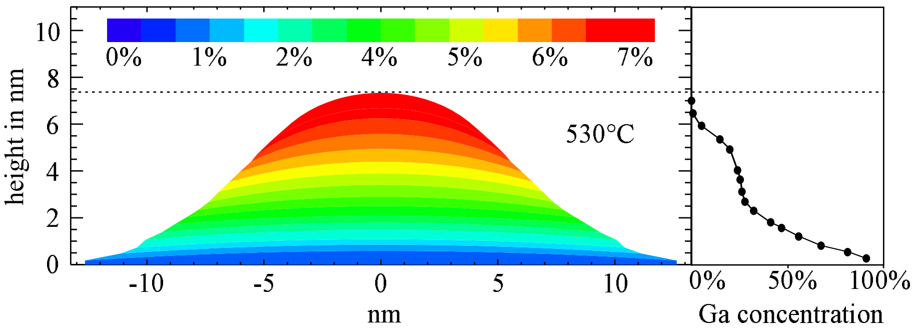

Figure 2.20: Tomographic image for sample B1. Apart from the smaller island size, the result is qualitatively similar to that of sample A1 in Fig. 2.19

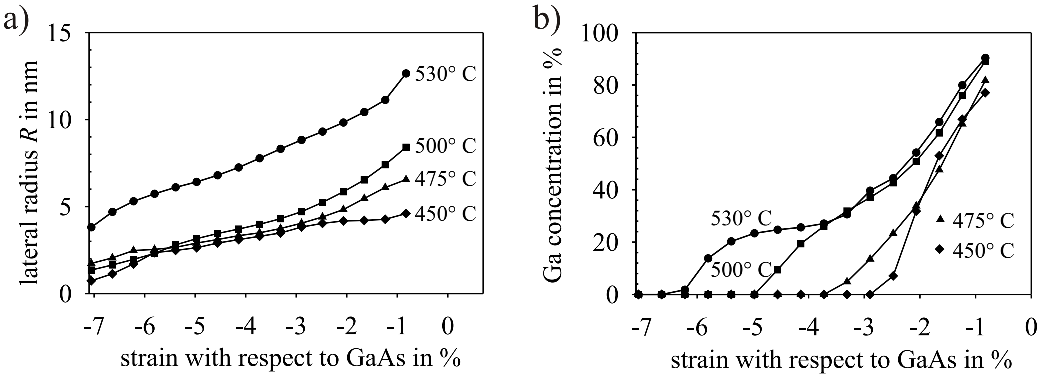

Figure 2.21: Results for lateral size and composition as functions of strain relative to the GaAs substrate for series B. Contrary to series A (see Fig. 2.18), the whole lattice parameter range between GaAs and InAs can be evaluated. Besides the systematic decrease in size, (a) also shows a change in shape between the various temperatures. Likewise, the composition in (b) shows a systematic behavior, with decreasing Ga content for decreasing growth temperature.

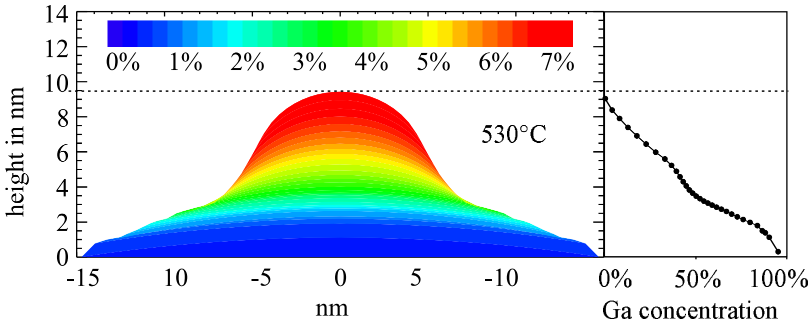

Figure 2.22: Tomographic image for sample C. The result is qualitatively similar to that of sample A1 in Fig. 2.19

into the islands is still unclear, these measurements shed light on the related temperature dependence and diffusion profiles.

2.5.4 Atomistic calculations of strain relaxation

Finite element calculations have long been in use for simulating strain and stress in crystalline structures [98]. With the investigation of smaller and smaller nano-structures, the atomistic nature of matter can no longer be neglected. Especially in hetero-epitaxial systems with a lattice parameter mismatch of a few percent and only a few hundred thousand atoms forming a single nano-structure, the continuum approximations may break down, giving incorrect results in highly stressed regions. The granularity of matter comes even more into play for nano-crystallites with heterogeneous composition: For structures with a diameter of the order of 10 unit cells, the substitutional incorporation of foreign atoms cannot be accurately described by continuously varying coefficients of elasticity for a bulk crystal with the local material composition. An atomistic approach is therefore more suitable* [99].

Although the full quantum mechanical treatment of an atomic lattice is a formidable task far beyond the capabilities of today's computers, classical many-body interatomic potentials [100] have been constructed to give excellent results for first-order elastic constants in GaAs and InAs [101]. Using a conjugate gradient method [102] to find the closest local potential energy minimum for a set of atoms, the relaxed spatial configuration can be deter-

---

The calculations presented in this section are the result of a DAAD collaboration with K. Nordlund at the University of Helsinki, Finland mined for modelled nano-structures which are initially out of equilibrium. Relaxing an uncapped nano-structure which is a few tens of nanometers across, requires a substantial substrate for which the island acts as a stressor. Therefore, a few million atoms need to be included in order to obtain a realistic model. Computing devices operating at 50 MFlop/s are capable of processing one such calculation in a time span of typically 20 hours.

Usually, calculations of strain fields are compared to experimental results of diffuse scattering [99]. Since the results presented in section 2.5 lead to real-space structural models, a much more direct self-consistency check between theory and experiment can be made: The experimentally determined outer shape together with the associated Ga concentration profiles for samples A1, A2 and C are taken as input data for a rotationally symmetric atomistic construction of the island with all unit cells chosen to be of the size of GaAs. To be self-consistent, the strain field in the relaxed island must then match the tomographic images of the experimental evaluation.

One missing link in the experimental method is the lateral composition profile of Ga. Recent findings of Liu et al. [94] show that for buried [103] $In_{0.5}Ga_{0.5}As$ quantum dots grown at 510° C, significant lateral compositional inhomogeneity occurs, where most of the In is concentrated in an inverted cone with the tip at the bottom of the dot. If such an In distribution can be generalized to include other $In_xGa_{1-x}As$ quantum dot systems and even be explained as a property of free-standing islands, the resulting strain states should be compatible with the results of section 2.5. However, in our case of pure InAs deposition, the corresponding atomistic calculation which is shown in Fig. 2.23 contradicts the experimental results in Fig. 2.19.

Assuming a laterally homogeneous Ga-profile leads to the strain distributions shown in the right hand side of Fig. 2.24 where the experimentally found strain fields are compared with the outcome of the atomistic calculations for series A and C. The good qualitative agreement between each corresponding pair of images shows that the assumption of a laterally constant composition is in accordance with the experiment. The jagged nature of the iso-strain areas together with the appearance of surface effects in the simulated strain fields are due to the statistical nature of the dot composition. The strain relaxation simulations are carried out with one particular random configuration of In and Ga atoms having the correct depth dependence in the concentrations. In the x-ray experiments, at least 10^5 such islands – all with different configurations – contribute to the detected intensity. However, the

---

*Here, an adaptive conjugate gradient described in Ref. 99 has been used to minimize the potential energy, which reduces the required floating point operations to one third of that of conventional conjugate gradient methods.

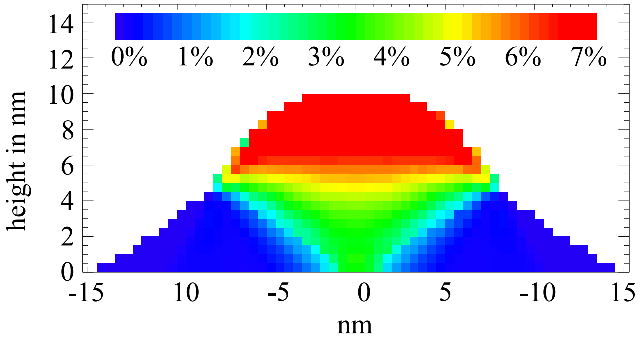

Figure 2.23: Atomistic strain calculation for sample A1 with "inverted cone"-In profile as suggested by Ref. [94]. The color scale shows the strain in the [110] direction with respect to the GaAs substrate. The apparent "resolution element" comprises several atoms to achieve a smooth transition of colors. The laterally averaged vertical Ga concentration is the same as that of sample A1. These results are in contradiction to Fig. 2.19

quantitative range of strain with respect to the GaAs substrate as well as the curvature of the iso-strain areas are both reproduced in the theoretical simulation. It has to be noted that the introduction of curvature is not an artefact of the initial assumptions, since the composition in the atomistic model has planar iso-surfaces. For practical purposes, the now available information on strain and composition can thus be regarded as complete.

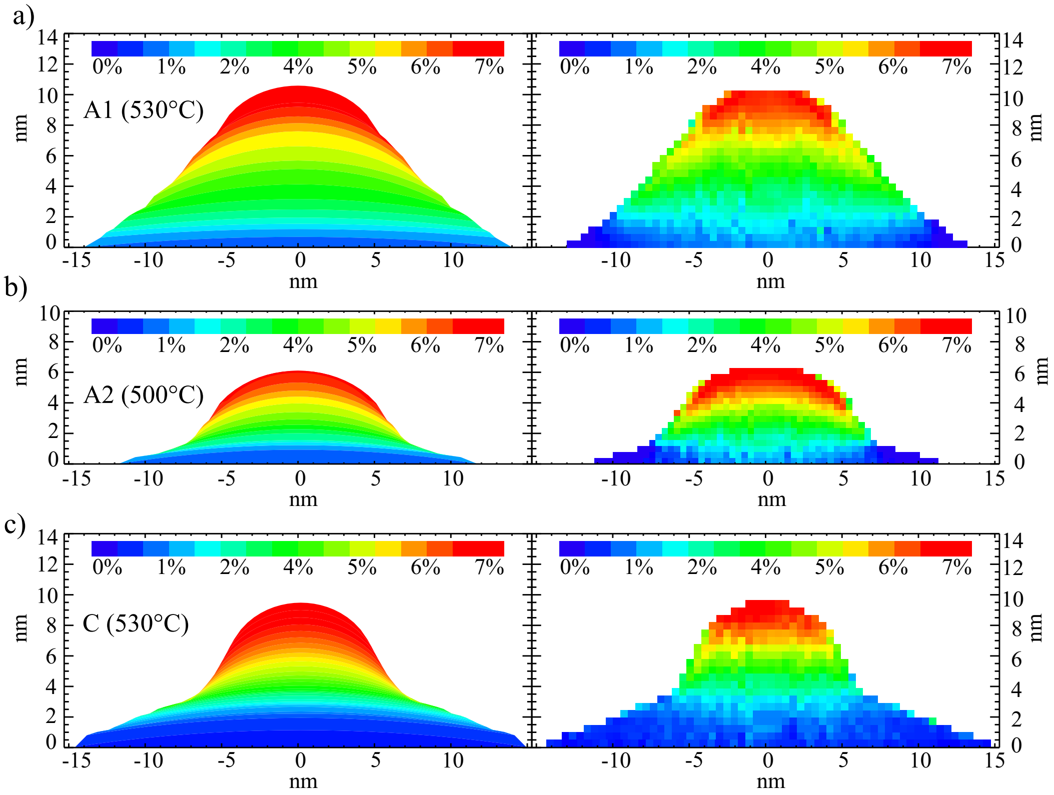

Figure 2.24: Atomistic calculations of strain fields compared to experimental images. Series A and C have been simulated starting from an atomistic reconstruction of the islands with a lattice parameter of GaAs throughout the dot and shape and vertical Ga-profile taken from Fig. 2.19 and Fig. 2.22. The lateral distribution of Ga has been assumed to be constant. Reasonable agreement is achieved for the quantitative range of strain with respect to the GaAs substrate and the curvature of the iso-strain areas which is not present in the iso-surfaces of the material composition of the atomic model. (a) and (b) show the comparisons for the samples of series A grown at 530° C and 500° C, in part (c) sample C is displayed. The left hand side of each pair of images is the experimental result, while the right hand side shows the corresponding atomistic calculation.

Appendix A

Modified Laue formula for vertically stacked quantum dots

Starting from Eq. (1.4), a suitable exponential term is factorized out in both numerator and denominator to obtain the functional form of sines:

$$\begin{aligned}
F_N\left(q_z, q_\parallel\right) &= \frac{1-e^{N\left(iq_zD-\sigma^2q_\parallel^2-\mu\right)}}{1-e^{iq_zD-\sigma^2q_\parallel^2-\mu}} \\
&= \frac{e^{i\frac{N}{2}\left(q_zD+i\sigma^2q_x^2+i\mu\right)}}{e^{i\frac{1}{2}(q_zD+i\sigma^2q_x^2+i\mu)}}\ \frac{e^{-i\frac{N}{2}\left(q_zD+i\sigma^2q_\parallel^2+i\mu\right)}-e^{i\frac{N}{2}\left(q_zD+i\sigma^2q_\parallel^2+i\mu\right)}}{e^{-i\frac{1}{2}\left(q_zD+i\sigma^2q_\parallel^2+i\mu\right)}-e^{i\frac{1}{2}\left(q_zD+i\sigma^2q_\parallel^2+i\mu\right)}} \\
&= e^{i\frac{1}{2}q_z(N-1)D-\frac{1}{2}\sigma^2q_x^2(N-1)}\ \frac{\sin\frac{q_zND+i\sigma^2q_x^2N}{2}}{\sin\frac{q_zD+i\sigma^2q_x^2}{2}} \\
&= e^{i\frac{1}{2}q_z(N-1)D-\frac{1}{2}\sigma^2q_x^2(N-1)}\times \\
&\qquad \frac{\sin\frac{q_zND}{2}\cosh\frac{\sigma^2q_x^2N}{2}+i\cos\frac{q_zND}{2}\sinh\frac{\sigma^2q_x^2N}{2}}{\sin\frac{q_zD}{2}\cosh\frac{\sigma^2q_x^2}{2}+i\cos\frac{q_zD}{2}\sinh\frac{\sigma^2q_x^2}{2}}.
\end{aligned} \tag{A.1}$$

The structure factor, which is the absolute square of $F_N(q_z, q_\parallel)$ is thus

$$\begin{aligned}
S_N\left(q_z, q_\parallel\right) &= \left|F_N\left(q_z, q_\parallel\right)\right|^2 \\
&= e^{-\sigma^2q_\parallel^2(N-1)}\ \frac{\sin^2\frac{q_zND}{2}\cosh^2\frac{\sigma^2q_x^2N}{2}+\cos^2\frac{q_zND}{2}\sinh^2\frac{\sigma^2q_x^2N}{2}}{\sin^2\frac{q_zD}{2}\cosh^2\frac{\sigma^2q_x^2}{2}+\cos^2\frac{q_zD}{2}\sinh^2\frac{\sigma^2q_x^2}{2}} \\
&= e^{-\sigma^2q_\parallel^2(N-1)}\times \\
&\qquad \frac{\sin^2\frac{q_zND}{2}\left(1+\sinh^2\frac{\sigma^2q_x^2N}{2}\right)+\left(1-\sin^2\frac{q_zND}{2}\right)\sinh^2\frac{\sigma^2q_x^2N}{2}}{\sin^2\frac{q_zD}{2}\left(1+\sinh^2\frac{\sigma^2q_x^2}{2}\right)+\left(1-\sin^2\frac{q_zD}{2}\right)\sinh^2\frac{\sigma^2q_x^2}{2}}.
\end{aligned} \tag{A.2}$$

The mixed terms cancel and the expression of Eq. (1.5)

$$S_N\left(q_z, q_{\|}\right) = e^{-\sigma^2 q_{\|}^2 (N-1)} \frac{\sin^2 \frac{q_z N D}{2} + \sinh^2 \frac{\sigma^2 q_x^2 N}{2}}{\sin^2 \frac{q_z D}{2} + \sinh^2 \frac{\sigma^2 q_x^2}{2}} \tag{A.3}$$

remains.

The half width of the principle maxima are most easily evaluated by considering the approximated envelope function of Eq. (A.3)

$$\begin{aligned} f\left(q_z\right) &= \frac{p}{\sin^2 \frac{q_z D}{2} + p} \\ \text{with} \quad p &= \sinh \frac{\sigma^2 q_x^2 + \mu}{2}. \end{aligned} \tag{A.4}$$

For the calculation of the half width, the numerator, which is constant in q_z, can be chosen arbitrarily as p to simplify the intermediate steps. Eq. (A.4) is increasingly inaccurate for very small σq_x, where the half widths go to zero. This effect can be incorporated into the constant μ, whose numerical value is of secondary interest. One maximum of Eq. (A.4) is

$$f_{max} = 1 \quad \text{at} \quad q_z = 0 \tag{A.5}$$

and the first consecutive minimum for positive q_z is

$$f_{min} = \frac{p}{1+p} \quad \text{at} \quad q_z = \frac{2\pi}{D}. \tag{A.6}$$

Hence, the half width Δq_z^{HWHM} is the value of q_z where f assumes the average value of f_{min} and f_{max}:

$$f\left(\Delta q_z^{HWHM}\right) = \frac{f_{min} + f_{max}}{2} = \frac{1}{2}\left(\frac{p}{1+p}\right) = \frac{1+2p}{2\,(1+p)}. \tag{A.7}$$

Inserting f from Eq. (A.4) gives an equation from which Δq_z^{HWHM} can be determined:

$$\frac{p}{\sin^2 \frac{\Delta q_z^{HWHM} D}{2} + p} = \frac{1+2p}{2\,(1+p)}. \tag{A.8}$$

The remaining task is to resolve Eq. (A.8) for Δq_z^{HWHM}.

$$\sin^2 \frac{\Delta q_z^{HWHM} D}{2} = \frac{2p\,(1+p)}{1+2p} - p = \frac{p}{1+2p}. \tag{A.9}$$

p is now inserted from Eq. (A.4) and transformed to a simple expression with a single trigonometrical function on both sides:

$$\begin{aligned}\sin^2 \frac{\Delta q_z^{HWHM} D}{2} &= \frac{\sinh^2 \frac{\sigma^2 q_x^2 + \mu}{2}}{1 + 2\sinh^2 \frac{\sigma^2 q_x^2 + \mu}{2}} = \frac{\sinh^2 \frac{\sigma^2 q_x^2 + \mu}{2}}{\cosh\left(\sigma^2 q_x^2 + \mu\right)} \\ &= \frac{\frac{1}{2}\left(\cosh \sigma^2 q_x^2 + \mu - 1\right)}{\cosh\left(\sigma^2 q_x^2 + \mu\right)} = \frac{1}{2}\left(1 - \frac{1}{\cosh\left(\sigma^2 q_x^2 + \mu\right)}\right),\end{aligned} \tag{A.10}$$

which can be rewritten as

$$\begin{aligned}1 - 2\sin^2 \frac{\Delta q_z^{HWHM} D}{2} &= \frac{1}{\cosh\left(\sigma^2 q_x^2 + \mu\right)} \\ \cos \Delta q_z^{HWHM} D &= \frac{1}{\cosh\left(\sigma^2 q_x^2 + \mu\right)}\end{aligned} \tag{A.11}$$

Using the notion of *secans hyperbolicus*, the resulting expression appears especially simple

$$\cos \Delta q_z^{HWHM} D = \operatorname{sech}\left(\sigma^2 q_x^2 + \mu\right) \tag{A.12}$$

and can be resolved for q_z:

$$\Delta q_z^{HWHM} = \frac{1}{D} \arccos \operatorname{sech}\left(\sigma^2 q_x^2 + \mu\right), \tag{A.13}$$

which is the same as Eq. (1.9).

Appendix B

Random positional stacking faults in a one-dimensional lattice

The derivation* leading to Eq. (1.16) starts from the assumption that the nearest neighbor has a spatial distribution of

$$f_1(x) = \frac{1}{\sqrt{2\pi}\gamma}\, e^{-\frac{x^2}{\gamma^2}} \tag{B.1}$$

around its regular lattice position, with γ as the disorder parameter of the system. The spatial distribution of the n-th neighbor with respect to the same reference point is obtained by subsequent folding of f_1 with itself:

$$\begin{aligned} f_n(x) &= \underbrace{f_1(x) \otimes f_1(x) \cdots \otimes f_1(x)}_{n \text{ times}} \\ &= \frac{1}{\sqrt{2\pi} n\gamma}\, e^{-\frac{x^2}{n\gamma^2}}, \end{aligned} \tag{B.2}$$

which corresponds to a $\sqrt{n}$-fold increase in half width, but retains the same functional form as for the nearest neighbor.

If $\rho_i(x)$ is defined as the delta-function describing the spatial deviation of the i-th point of the actual lattice, the convolution $\rho_i(x) \otimes \rho_j(-x)$ gives the difference of the distance between the i-th and j-th lattice points from the nominal value prescribed by the perfect lattice. For the homogeneous system

---

*A short form of this derivation is reported in Ref. 56 for random positional stacking faults of lattice *planes* described by Eq. (B.1), the average for the ensemble of all lattice points with the same distance $i - j$ is equivalent to $f_{|i-j|}$:

$$\langle \rho_i(x) \otimes \rho_j(-x) \rangle_{i-j=const} = f_{|i-j|}(x). \tag{B.3}$$

The density function $\rho(x)$ of the entire lattice – modulo the structure factor of a single lattice point – is given by

$$\rho(x) = \sum_i \rho_i(x) \otimes \delta(x - iD), \tag{B.4}$$

where D is the lattice constant. To calculate the scattering intensity for ρ, the Patterson function* $P(x)$ is calculated:

$$\begin{aligned} P(x) &= \rho(x) \otimes \rho(-x) \\ &= \sum_i \sum_j \big[\rho_i(x) \otimes \delta(x - iD)\big] \big[\rho_j(-x) \otimes \delta(x + jD)\big] \\ &= \sum_i \sum_j \big[\rho_i(x) \otimes \rho_j(-x)\big] \otimes \big[\delta(x - iD) \otimes \delta(x + jD)\big] \\ &= \sum_n \sum_{i-j=n} \big[\rho_i(x) \otimes \rho_j(x)\big] \otimes \delta[x - (i-j)D]. \end{aligned} \tag{B.5}$$

The second sum in the last step of Eq. (B.5) is equivalent to a statistical averaging for the ensemble of lattice points with n periods apart. Hence, after Eq. (B.3) is inserted, the Patterson function can be rewritten as a single sum:

$$\begin{aligned} P(x) &= \sum_n f_{|n|}(x) \otimes \delta(x - nD) \\ &= \sum_n \frac{1}{\sqrt{2\pi}|n|\gamma}\, e^{-\frac{x^2}{|n|\gamma^2}} \otimes \delta(x - nD). \end{aligned} \tag{B.6}$$

The structure factor $S(q)$ is now readily calculated as

$$\begin{aligned} S(q) &= \mathcal{F}\{P(x)\} \\ &= \sum_n e^{-\frac{1}{4}q^2|n|\gamma^2} \times e^{iqnD}. \end{aligned} \tag{B.7}$$

---

*The Patterson function is the autocorrelation function [104] of the density function and is related to the scattering intensity by a simple Fourier transform. This intermediate step allows for the introduction of statistical averaging *before* applying a Fourier transform.

Now, the sum in Eq. (B.7) is split into two sums running from zero to infinity. Since the 0-th term is counted twice it has to be subtracted. The resulting geometric series can be evaluated analytically as

$$\begin{aligned} S(q) &= \sum_n e^{-\left(\frac{1}{4}q^2\gamma^2 - iqD\right)n} + \sum_n e^{-\left(\frac{1}{4}q^2\gamma^2 + iqD\right)n} - 1 \\ &= \frac{1}{1-\exp\left(-\frac{1}{4}q^2\gamma^2 + iqD\right)} + \frac{1}{1-\exp\left(-\frac{1}{4}q^2\gamma^2 - iqD\right)} - 1 \\ &= \frac{1-\exp\left(-\frac{1}{2}q^2\gamma^2\right)}{1+\exp\left(-\frac{1}{2}q^2\gamma^2\right) - 2\exp\left(-\frac{1}{4}q^2\gamma^2\right)\cos\left(qD\right)}, \end{aligned} \tag{B.8}$$

yielding the expression in Eq. (1.16).

It is important to note that this approach holds for a two-dimensional rectangular lattice with lattice constants (D_x, D_y) with a Gaussian nearest-neighbor distribution and arbitrary error ellipse whose principle axes γ_x and γ_y are aligned with the two-dimensional coordinate system (x, y) of the lattice. The Patterson function in Eq. (B.6) can be written as

$$P(x,y) = \sum_n \sum_m \frac{\exp\left(-\frac{x^2}{|n|\gamma_x^2} - \frac{y^2}{|m|\gamma_y^2}\right)}{\pi\sqrt{|n|\gamma_x^2 + |m|\gamma_y^2}} \otimes \delta(x - nD_x, y - mD_y), \tag{B.9}$$

since in all steps leading to Eq. (B.6), x can be replaced by a two dimensional vector (x, y). The resulting structure factor

$$\begin{aligned} S(q_x, q_y) &= \mathcal{F}\{P(x,y)\} \\ &= \sum_n e^{-\frac{1}{4}\left(q_x^2|n|\gamma_x^2 + q_y^2|m|\gamma_y^2\right)} \times e^{iq_x nD_x + iq_y nD_y} \end{aligned} \tag{B.10}$$

separates into two expressions of type Eq. (B.7):

$$S(q_x, q_y) = S_x(q_x)\ S_y(q_y) \tag{B.11}$$

Since Eq. (B.11) cannot be applied to lattices with a four-dimensional symmetry *and* an ordering anisotropy, the one-dimensional "lattice line" approach is more general, though only approximate. As the system presented in section 1.2.2 shows no anisotropy in γ, it could *a posteriori* be described by the fully two-dimensional Eq. (B.11).

Appendix C

Maximum of the generalized optical function

Starting from the expression for grazing angles below the critical angle of total reflection ($\hat{\alpha}$) in Eq. (2.36)

$$I(\hat{\alpha}) = 2 + 2\left(2\hat{\alpha}^2 - 1\right)\cos 2\hat{\alpha}\hat{z} + 4\hat{\alpha}\sqrt{1-\hat{\alpha}^2}\ \sin 2\hat{\alpha}\hat{z}, \tag{C.1}$$

the angle of maximum intensity is determined by calculating the null of the derivative of Eq. (C.1):

$$\begin{aligned}
\frac{\mathrm{d}I(\hat{\alpha})}{\mathrm{d}\hat{\alpha}} &= 4\hat{\alpha}\cos 2\hat{z}\hat{\alpha} - 2\hat{z}\left(2\hat{\alpha}^2-1\right)\sin 2\hat{z}\hat{\alpha} + \\
&\quad + \left(2\sqrt{1-\hat{\alpha}^2} + \frac{2\hat{\alpha}(-2\hat{\alpha})}{2\sqrt{1-\hat{\alpha}^2}}\right)\sin 2\hat{z}\hat{\alpha} + 4\hat{z}\hat{\alpha}\sqrt{1-\hat{\alpha}^2}\cos 2\hat{z}\hat{\alpha} \\
&= 4\hat{\alpha}\left(1+\hat{z}\sqrt{1-\hat{\alpha}^2}\right)\cos 2\hat{z}\hat{\alpha} - \\
&\qquad \left[2\frac{2\hat{\alpha}^2-1}{\sqrt{1-\hat{\alpha}^2}} + 2\hat{z}\left(2\hat{\alpha}^2-1\right)\right]\sin 2\hat{z}\hat{\alpha} \\
&= 4\hat{\alpha}\left(1+\hat{z}\sqrt{1-\hat{\alpha}^2}\right)\cos 2\hat{z}\hat{\alpha} - \\
&\qquad \frac{2\left(2\hat{\alpha}^2-1\right)}{\sqrt{1-\hat{\alpha}^2}}\left(1+\hat{z}\sqrt{1-\hat{\alpha}^2}\right)\sin 2\hat{z}\hat{\alpha} \\
&= 2\hat{\alpha}\left(1+\hat{z}\sqrt{1-\hat{\alpha}^2}\right)\left[2\hat{\alpha}\cos 2\hat{z}\hat{\alpha} - \frac{(2\hat{\alpha}^2-1)}{\sqrt{1-\hat{\alpha}^2}}\sin 2\hat{z}\hat{\alpha}\right].
\end{aligned} \tag{C.2}$$

The first bracket in Eq. (C.2) cannot become zero for $\hat{z} > 0$, a possible null $\hat{\alpha}_{max}$ of the second bracket is determined by

$$2\hat{\alpha}_{max} \cos 2\hat{z}\hat{\alpha}_{max} - \frac{(2\hat{\alpha}_{max}^2 - 1)}{\sqrt{1 - \hat{\alpha}_{max}^2}} \sin 2\hat{z}\hat{\alpha}_{max} = 0. \tag{C.3}$$

Since $\hat{\alpha}_{max} < 1$, $\hat{\alpha}_{max} = \cos u$ is a valid substitution, which is now applied for all instances of $\hat{\alpha}_{max}$ outside of trigonometric functions:

$$2\cos u \cos 2\hat{z}\hat{\alpha}_{max} - \frac{(2\cos^2 u - 1)}{\sqrt{1 - \cos^2 u}} \sin 2\hat{z}\hat{\alpha}_{max} = 0$$

$$2\cos u \cos 2\hat{z}\hat{\alpha}_{max} - \frac{\cos 2u}{\sin u} \sin 2\hat{z}\hat{\alpha}_{max} = 0. \tag{C.4}$$

Since $\sin u = 0$ corresponds to $\hat{\alpha}_{max} = 1$, which is not considered here, Eq. (C.4) can be multiplied by $\sin u$.

$$2\sin u \cos u \cos 2\hat{z}\hat{\alpha}_{max} - \cos 2u \sin 2\hat{z}\hat{\alpha}_{max} = 0$$

$$\sin 2u \cos 2\hat{z}\hat{\alpha}_{max} - \cos 2u \sin 2\hat{z}\hat{\alpha}_{max} = 0$$

$$\sin(2u - 2\hat{z}\hat{\alpha}_{max}) = 0. \tag{C.5}$$

The only null of Eq. (C.5), which will produce real values for $\hat{\alpha}_{max}$ is found for a vanishing argument of the sine:

$$2u - 2\hat{z}\hat{\alpha}_{max} = 0, \tag{C.6}$$

which, after reinsertion of the definition of u gives

$$\arccos \hat{\alpha} - \hat{z}\hat{\alpha}_{max} = 0$$

$$\hat{\alpha}_{max} = \cos \hat{z}\hat{\alpha}_{max}. \tag{C.7}$$

This is the same expression as in Eq. (2.37).*

---

*The proof that the smallest solution for $\hat{\alpha}_{max}$ in Eq. (C.7) is always a maximum, is lengthy and does not provide much further insight.

Appendix D

Calculation of the material composition of a binary alloy from the ratio of two reflections

The aim of contrast variation is to extract the material composition of a binary alloy of constituents A and B from a strong (S) and a weak (W) reflection. For the weak reflection, the contribution from materials A and B may often be of different orders of magnitude. However, in the case of weak reflections the imaginary and the real part of the structure factors may become equally important, disallowing the neglection of the usually smaller imaginary part. The measured quantity p is the ratio of the observed intensities I^S and I^W at equivalent points in reciprocal space.

$$p = \frac{I^S}{I^W}. \tag{D.1}$$

With the complex structure factors defined as

$$\chi^{S/W}_{A/B} = \chi^{S/W}_{A/B,\Re} + i\chi^{S/W}_{A/B,\Im} \tag{D.2}$$

for both materials A and B and reflections S and W and c_A and c_B being the concentrations of A and B, the intensity ratio p is given by

$$p = \left| \frac{c_A\chi_A^S + c_B\chi_B^S}{c_A\chi_A^W + c_B\chi_B^W} \right|^2$$

$$\text{with} \quad c_a + c_b = 1. \tag{D.3}$$

To reduce Eq. (D.3) to one unknown variable, c_B is eliminated:

$$p = \left| \frac{c_A\left(\chi_A^S - \chi_B^S\right) + \chi_B^S}{c_A\left(\chi_A^W - \chi_B^W\right) + \chi_B^W} \right|^2, \tag{D.4}$$

which suggests the introduction of *difference structure factors* $\Delta\chi^S$ and $\Delta\chi^W$ defined as

$$\begin{aligned} \Delta\chi^{S/W} &= \chi_A^{S/W} - \chi_B^{S/W} = \Delta\chi_{\Re}^{S/W} + i\chi_{\Im}^{S/W} \\ \text{with} \quad \Delta\chi_{\Re/\Im}^{S/W} &= \chi_{A,\Re/\Im}^{S/W} - \chi_{B,\Re/\Im}^{S/W}. \end{aligned} \tag{D.5}$$

The resulting expression for g is then expanded into complex notation and the absolute square is calculated.

$$\begin{aligned} p &= \left| \frac{c_A \Delta\chi^S + \chi_B^S}{c_A \Delta\chi^W + \chi_B^W} \right|^2 \\ &= \left| \frac{\left(c_A \Delta\chi_{\Re}^S + \chi_{B,\Re}^S\right) + i\left(c_A \Delta\chi_{\Im}^S + \chi_{B,\Im}^S\right)}{\left(c_A \Delta\chi_{\Re}^W + \chi_{B,\Re}^W\right) + i\left(c_A \Delta\chi_{\Im}^W + \chi_{B,\Im}^W\right)} \right|^2 \\ &= \frac{\left(c_A \Delta\chi_{\Re}^S + \chi_{B,\Re}^S\right)^2 + \left(c_A \Delta\chi_{\Im}^S + \chi_{B,\Im}^S\right)^2}{\left(c_A \Delta\chi_{\Re}^W + \chi_{B,\Re}^W\right)^2 + \left(c_A \Delta\chi_{\Im}^W + \chi_{B,\Im}^W\right)^2} \\ &= \frac{c_A^2 \left|\Delta\chi^S\right|^2 + 2c_A\left(\Delta\chi_{\Re}^S \chi_{B,\Re}^S + \Delta\chi_{\Im}^S \chi_{B,\Im}^S\right) + \left|\chi_B^S\right|^2}{c_A^2 \left|\Delta\chi^W\right|^2 + 2c_A\left(\Delta\chi_{\Re}^W \chi_{B,\Re}^W + \Delta\chi_{\Im}^W \chi_{B,\Im}^W\right) + \left|\chi_B^W\right|^2}. \end{aligned} \tag{D.6}$$

The fraction in Eq. (D.6) is now resolved into a second order polynomial[*] in c_A,

$$\begin{aligned} c_A^2 \left(p\left|\Delta\chi^W\right|^2 - \left|\Delta\chi^S\right|^2\right) + 2c_A\left[p\Re\langle\Delta\chi^W, \chi_B^W\rangle - \Re\langle\Delta\chi^S, \chi_B^S\rangle\right] + \\ + \left(p\left|\chi_B^W\right|^2 - \left|\chi_B^S\right|^2\right) = 0, \end{aligned} \tag{D.7}$$

and resolved for c_A:

$$\begin{aligned} c_A = \frac{1}{p\left|\Delta\chi^W\right|^2 - \left|\Delta\chi^S\right|^2} \Bigg[& - p\Re\langle\Delta\chi^W, \chi_B^W\rangle + \Re\langle\Delta\chi^S, \chi_B^S\rangle - \\ & \sqrt{\left(p\Re\langle\Delta\chi^W, \chi_B^W\rangle - \Re\langle\Delta\chi^S, \chi_B^S\rangle\right)^2 - 4\left(p\left|\Delta\chi^W\right|^2 - \left|\Delta\chi^S\right|^2\right)\left(p\left|\chi_B^W\right|^2 - \left|\chi_B^S\right|^2\right)} \Bigg]. \end{aligned} \tag{D.8}$$

---

[*] $\langle .\,, . \rangle$ denotes the complex scalar product

Appendix E

Scattering coherence in disordered lattice coherent systems

The limits of the applicability of the Babinet principle [105] to *diffraction* experiments on self-organized nano-structures may sometimes not be immediately evident. Originally, the Babinet-principle has been formulated for optics and is often used in the context of small angle x-ray scattering. By analogy, the small angle pattern around a Bragg reflection can be interpreted by invoking the equivalence of regions with swapped electron densities. Holes in a lattice matrix will effectively produce the same small angle scattering as if there were no matrix and a corresponding lattice in the place of the holes.

However, the attempt to discuss the effects of lattice coherence in the framework of the Babinet principle will not lead to correct results. The Babinet principle deals with alternating regions of *locally constant* electron density, ignoring any *globally constant* scattering potential. Approximating an atomic lattice by a constant electron density for a diffraction experiment is highly inaccurate and effectively implies a neglection of the diffraction process itself. The point of view is thus changed to that of a forward scattering experiment. While the small angle pattern can nonetheless be successfully evaluated, any conclusions regarding the Bragg-peaks themselves are inherently wrong.

A typical misconception of this kind is the assumption that ensembles of free-standing nano-structures which are coherent to the substrate, but otherwise not perfectly ordered, should scatter coherently. The argument asserts, that since equivalent holes in a lattice matrix would result in sharp Bragg-peaks with broad small angle patterns around them, by virtue of the Babinet principle this must also be true for the free-standing case. The following calculation explicitly shows that this conclusion is incorrect.

Consider a one-dimensional arrangement of N "islands" consisting of M atoms with lattice parameter a. The islands are spaced at random positions $p_n\, a$ where p_n are integers with $p_n - p_{n-1} > M$. (see Fig. E.1). The extension to a two-dimensional quadratic lattice is straightforward.

The structure factor of this model is given by

$$F(q) = \sum_{n=0}^{N-1} \sum_{m=0}^{M-1} e^{iq(p_n a + ma)}. \tag{E.1}$$

The "form factor" part of the islands splits off and produces an ordinary Laue term, while the further exact treatment of the sum over n can only be carried out numerically.

$$F(q) = \frac{1 - e^{iqMa}}{1 - e^{iqa}} \sum_{n=0}^{N-1} e^{iqp_n a}. \tag{E.2}$$

In case of a perfectly periodic arrangement with $p_n = Pn$, Eq. (E.2) reduces to

$$F_{\text{periodic}}(q) = \frac{1 - e^{iqMa}}{1 - e^{iqa}} \times \frac{1 - e^{iqPNa}}{1 - e^{iqPa}}, \tag{E.3}$$

leading to dominant superstructure Bragg-peaks of half-width $(Pa)^{-1}$ and maximum intensity $(PMN)^2$. The total intensity below each Bragg-peak

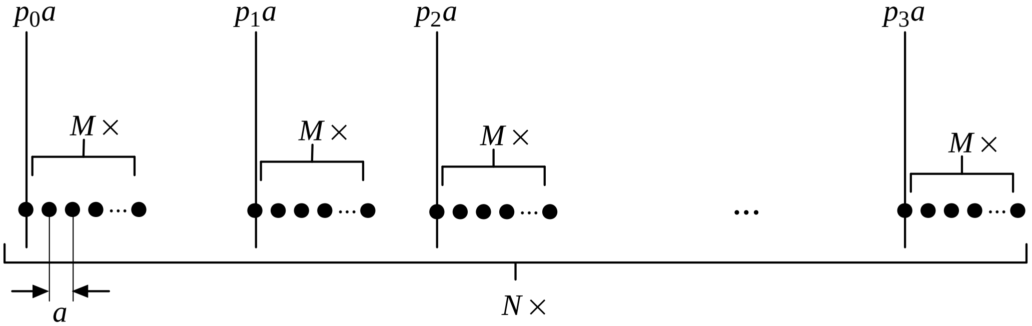

Figure E.1: One-dimensional model for the calculation of coherence effects in quantum dot systems. N islands consisting of M atoms with lattice parameter a are spaced at integer multiples p of the lattice parameter. The positions of the islands are varied in integer steps of a with a Gaussian random variable of standard deviation σ.

thus scales as $(MN)^2$. This is indeed a case of coherent inter-island interference with a small angle pattern of the dot form factor around each peak.

For totally random p_n, averaged for an ensemble of such systems, the sum over n yields $\sqrt{N}$ by a random walk argument for the vector diagram of the sum in complex space.

$$F_{\text{random}}(q) = \sqrt{N}\,\frac{1 - e^{iqMa}}{1 - e^{iqa}} \tag{E.4}$$

giving Bragg-peaks of half-width $(Ma)^{-1}$ and maximum intensity NM^2. The total intensity below each Bragg-peak thus scales as N which indicates an incoherent scattering of the islands.

For intermediate situations, Eq. (B.8) is a suitable replacement for the scattering intensity of the sum over n in Eq. (E.2). In this case, there will be broad superstructure reflections whose intensities decay with a Gaussian characteristics along q.

Appendix F

Angle of exit in the w21v geometry

The w21v diffractometer geometry as used at the TROÏKA II beamline involves four circles. Two circles α and ω rotate the sample, two circles δ and γ move the detector, both sets of circles being independent of each other* (see Fig. F.1). In each set of circles, one axis is fixed in space (α and δ, resp.), while the other is rotated together with the first (ω and γ, resp.). For grazing incidence diffraction experiments, it is most convenient to use the fixed axis α of the sample to adjust the angle of incidence. The azimuth of the sample can then be changed by varying ω without the need to continously readjust α to keep a constant penetration depth. The δ-axis of the detector will thus vary the angle of exit, while γ is used to set the scattering angle for the diffraction process.

Alignment and data collection in grazing incidence diffraction measurements are greatly facilitated by the use of a position sensitive detector (PSD) whose angular variation is set up to be along the angle of exit (i.e. along δ) for $\gamma = 0$. This angular variation has to be considered as a separate axis β on which none of the other axes are dependent. For the experiments presented in section 2.5, an accurate knowledge of α_f is mandatory. The w21v diffractometer geometry, however, has the side effect that the angle of exit depends on the positions of γ and δ in a non-trivial way, with the PSD-axis β introducing an additional complication. For the reasons discussed in section 2.3.3, re-gauging the zero for α_f using the transmission maximum at the Bragg-angle is not advisable for samples with free-standing nano-structures.

For the calculation of the total rotation matrix *with respect to the sample*

---

*For this reason, the diffractometer geometry is also called the s2d2-geometry (two circles for the sample, two for the detector)

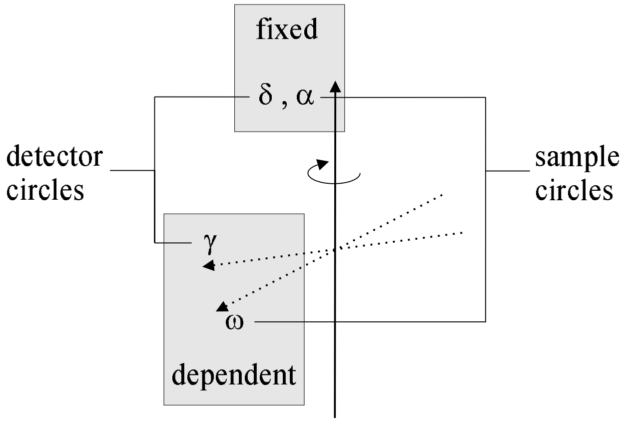

Figure F.1: Circles in the w21v diffractometer geometry. The two sets of circles for sample and detector are independent of each other. Each set consists of one fixed and one dependent axis.

surface, the coordinate system at $\delta = \gamma = \beta = 0$ is chosen with the x-axis pointing towards the detector and the z-axis parallel to the surface normal of the sample. For the calculation, the three-dimensional rotation matrices around the z and y axis are required:

$$\underline{\mathbf{R}}^y(\theta) = \begin{pmatrix} \cos\theta & 0 & -\sin\theta \\ 0 & 1 & 0 \\ \sin\theta & 0 & \cos\theta \end{pmatrix}$$

$$\underline{\mathbf{R}}^z(\theta) = \begin{pmatrix} \cos\theta & -\sin\theta & 0 \\ \sin\theta & \cos\theta & 0 \\ 0 & 0 & 1 \end{pmatrix} \tag{F.1}$$

The rotation of the detector can be described as a product of cartesian rotation matrices of all circles, if *all* relevant axes can be arranged in such a sequence that for any single matrix the corresponding axis is independent on on any matrices on the right. This can be shown geometrically, but the key argument is highly intuitive: any dependencies on axes that are treated later on in the calculation chain are irrelevant. For the w21v geometry the correct total matrix $\underline{\mathbf{R}}(\delta, \gamma, \beta, \alpha)$ to rotate the detector from its initial position $x = 1, y = z = 0$ to an angular configuration (δ, γ, β) with the angle of incidence set at α is given by

$$\underline{\mathbf{R}}(\delta, \gamma, \beta, \alpha) = \underline{\mathbf{R}}^y(\delta - \alpha).\underline{\mathbf{R}}^z(\gamma).\underline{\mathbf{R}}^y(\beta) \tag{F.2}$$

The γ-axis is fixed with respect to the PSD-axis β and neither the δ nor the α-axis are dependent on γ or β. Since the α-axis coincides with the δ-axis, for which it effectively sets the zero position, both axes can be combined into a single rotation matrix around y with a rotation angle of $\delta - \alpha$.

The total rotation matrix is calculated explicitely as

$$\underline{\mathbf{R}}(\delta,\gamma,\beta,\alpha) =$$

$$\begin{pmatrix} \begin{array}{l} \cos\beta\cos\gamma\cos(\delta-\alpha)- \\ \sin\beta\sin(\delta-\alpha) \end{array} & \cos(\delta-\alpha)\sin\gamma & \begin{array}{l} \cos\gamma\cos(\delta-\alpha)\sin\beta- \\ \cos\beta\sin(\delta-\alpha) \end{array} \\ \cos\beta\sin\gamma & \cos\gamma & \sin\beta\sin\gamma \\ \begin{array}{l} \cos(\delta-\alpha)\sin\beta+ \\ \cos\beta\cos\gamma\sin(\delta-\alpha) \end{array} & \sin\gamma\sin(\delta-\alpha) & \begin{array}{l} \cos\beta\cos(\delta-\alpha)- \\ \cos\gamma\sin\beta\sin(\delta-\alpha) \end{array} \end{pmatrix} \tag{F.3}$$

The vector $\mathbf{d}(\delta,\gamma,\beta,\alpha)$ for the rotated detector is thus given by

$$\begin{aligned} \mathbf{d}(\delta,\gamma,\beta,\alpha) &= \underline{\mathbf{R}}(\delta,\gamma,\beta,\alpha).\begin{pmatrix} 1 \\ 0 \\ 0 \end{pmatrix} \\ &= \begin{pmatrix} \cos\beta\cos\gamma\cos(\delta-\alpha)-\sin\beta\sin(\delta-\alpha) \\ \cos\beta\sin\gamma \\ \cos(\delta-\alpha)\sin\beta+\cos\beta\cos\gamma\sin(\delta-\alpha) \end{pmatrix}. \end{aligned} \tag{F.4}$$

Together with the projection of $\mathbf{d}(\delta,\gamma,\beta,\alpha)$ on the plane of the sample surface, which – by definition – coincides with the xz-plane

$$\mathbf{d}^{proj}(\delta,\gamma,\beta,\alpha) = \begin{pmatrix} \cos\beta\cos\gamma\cos(\delta-\alpha)-\sin\beta\sin(\delta-\alpha) \\ \cos\beta\sin\gamma \\ 0 \end{pmatrix}, \tag{F.5}$$

the angle of exit can be calculated as

$$\begin{aligned} \cos\alpha_f(\delta,\gamma,\beta,\alpha) &= \frac{\mathbf{d}(\delta,\gamma,\beta,\alpha).\mathbf{d}^{proj}(\delta,\gamma,\beta,\alpha)}{|\mathbf{d}^{proj}(\delta,\gamma,\beta,\alpha)|} \\ &= \sqrt{\cos^2\beta\sin^2\gamma+(\cos\beta\cos\gamma\cos(\delta-\alpha)-\sin\alpha\sin(\delta-\alpha))^2}. \end{aligned} \tag{F.6}$$

It is often of experimental interest to determine the position β on the detector, for which the angle of exit is zero. Noting that positive angles of exit correspond to configurations where the z-component of $\mathbf{d}(\delta, \gamma, \beta, \alpha)$ in Eq. (F.4) is positive, the inequality

$$\tan\beta > \frac{\tan(\alpha - \delta)}{\cos\gamma} \qquad \text{for} \quad -\frac{\pi}{2} < \gamma < \frac{\pi}{2} \tag{F.7}$$

can be derived. At $\gamma = \frac{\pi}{2}$, a pole in the diffractometer geometry prevents arbitrary changes in the angle of exit.

List of Figures

Bibliography

[1] S. Facsko, T. Dekorsy, C. Koerdt, C. Trappe, H. Kurz, A. Vogt, and H. L. Hartnagel, Science **285**, 1551 (1999).

[2] D. J. Eaglesham and M. Cerullo, Phys. Rev. Lett. **64**, 1943 (1990).

[3] C. D. Andereck, S. S. Liu, and H. L. Swinney, J. Fluid Mech. **164**, 155 (1986).

[4] H. L. Swinney, in *Critical Problems in physics*, edited by V. L. Fitch, D. R. Marlow, and M. A. E. Dementi (Princeton University Press, Princeton, 1997), p. 51.

[5] D. J. Bottomley, Appl. Phys. Lett. **72**, 783 (1998).

[6] X. Z. Liao, J. Zou, D. J. H. Cockayne, J. Qin, Z. M. Jiang, X. Wang, and R. Leon, Phys. Rev. B **60**, 15605 (1999).

[7] J. Tersoff, Phys. Rev. Lett. **81**, 3183 (1998).

[8] F. M. Ross, J. Tersoff, and R. M. Tromp, Phys. Rev. Lett. **80**, 984 (1998).

[9] D. E. Jesson, G. Chen, K. M. Chen, and S. J. Pennycook, Phys. Rev. Lett. **80**, 5153 (1998).

[10] M. Iwamatsu and Y. Okabe, J. Appl. Phys. **86**, 5541 (1999).

[11] S. Lee, I. Daruka, C. S. Kim, A.-L. Barabási, J. L. Merz, and J. K. Furdyna, Phys. Rev. Lett. **81**, 3479 (1998).

[12] MRS Bull. **23**, (1998).

[13] D. Loss and D. P. DiVincenzo, Phys. Rev. A **57**, 120 (1998).

[14] R. Aguado and L. P. Kouwenhoven, Phys. Rev. Lett. **84**, 1986 (2000).

[15] V. A. Shchukin, N. N. Ledentsov, P. S. Kop'ev, and D. Bimberg, Phys. Rev. Lett. **75**, 2968 (1995).

[16] H. T. Dobbs, D. D. Vvedensky, A. Zangwill, J. Johansson, N. Carlsson, and W. Seifert, Phys. Rev. Lett. **79**, 897 (1997).

[17] J. Tersoff, C. Teichert, and M. G. Lagally, Phys. Rev. Lett. **76**, 1675 (1995).

[18] Q. Xie, A. Madhukar, P. Chen, and P. Kobayashi, Phys. Rev. Lett. **75**, 2542 (1995).

[19] G. S. Solomon, J. A. Trezza, M. A. F, and J. S. Harris, Phys. Rev. Lett. **76**, 952 (1996).

[20] A. A. Darhuber, P. Schittenhelm, V. Holý, J. Stangl, G. Bauer, and G. Abstreiter, Phys. Rev. B **55**, 15652 (1997).

[21] A. A. Darhuber, V. Holý, J. Stangl, G. Bauer, A. Krost, F. Heinrichsdorff, M. Grundmann, D. Bimberg, V. M. Ustinov, P. S. Kop'ev, A. O. Kosogov, and P. Werner, Appl. Phys. Lett. **70**, 955 (1997).

[22] O. G. Schmidt, S. Schieker, K. Eberl, and O. Kienzle, Appl. Phys. Lett. **73**, 659 (1998).

[23] V. Shchukin, D. Bimberg, V. G. Malyshkin, and N. N. Ledentsov, Phys. Rev. B **57**, 12262 (1998).

[24] G. Springholz, V. Holý, M. Pinczolits, and G. Bauer, Science **282**, 734 (1998).

[25] R. Nötzel, T. Fukui, H. Hasegawa, J. Temmyo, and T. Tamamura, Appl. Phys. Lett. **65**, 2854 (1994).

[26] J. M. García, G. Medeiros-Ribeiro, K. Schmidt, T. Ngo, J. L. Feng, A. Lorke, J. Kotthaus, and P. M. Petroff, Appl. Phys. Lett. **71**, 2014 (1997).

[27] P. D. Siverns, S. Malik, G. McPherson, D. Childs, C. Roberts, R. Murry, and B. A. Joyce, Phys. Rev. B **58**, R10127 (1998).

[28] I. Kegel, T. Metzger, J. Peisl, J. Stangl, G. Bauer, and D. Smilgies, Phys. Rev. B **60**, 2516 (1999).

[29] S. A. Stepanov, E. A. Kondrashkina, M. Schmidbauer, R. Köhler, J.-U. Pfeiffer, T. Jach, and A. Y. Souvorov, Phys. Rev. B **54**, 8150 (1996).

[30] E. K. D. Kandel, Phys. Rev. Lett. **75**, 2742 (1995).

[31] C. P. Liu, J. M. Gibson, D. G. Cahill, T. I. Kammins, D. P. Basile, and R. S. Williams, Phys. Rev. Lett. **84**, 1958 (2000).

[32] V. L. Thanh, V. Yam, P. Boucaud, F. Fortuna, C. Ulysse, D. Bouchier, L. Vervoort, and J.-M-Lourtioz, Phys. Rev. B **60**, 5851 (1999).

[33] H. Dosch, *Critical Phenomena at Surfaces and Interfaces* (Springer, Berlin, 1992).

[34] M. Schmidbauer, T. Wiebach, H. Raidt, M. Hanke, R. Köhler, and H. Wawra, Phys. Rev. B **58**, 10523 (1998).

[35] I. Kegel, T. H. Metzger, P. Fratzl, J. Peisl, A. Lorke, J. M. García, and P. M. Petroff, Europhys. Lett **45**, 222 (1999).

[36] M. Tolan, W. Press, F. Brinkop, and J. P. Kotthaus, J. Appl. Phys. **75**, 7761 (1994).

[37] R. L. Headrick and J.-M. Baribeau, Phys. Rev. B **48**, 9174 (1993).

[38] T. Salditt, T. H. Metzger, C. Brandt, U. Klemradt, and J. Peisl, Phys. Rev. B **51**, 5617 (1995).

[39] T. H. Metzger, K. Haj-Yahya, J. Peisl, M. Wendel, H. Lorenz, J. P. Kotthaus, and G. S. CargillIII, J. Appl. Phys. **81**, 1212 (1997).

[40] T. Salditt, T. H. Metzger, and J. Peisl, Phys. Rev. Lett. **73**, 2228 (1994).

[41] J. Stangl, V. Holý, P. Mikulik, G. Bauer, I. Kegel, T. H. Metzger, O. G. Schmid, C. Lange, and K. Eberl, Appl. Phys. Lett. **74**, 3785 (1999).

[42] O. Kienzle, F. Ernst, M. Rühle, O. G. Schmidt, and K. Eberl, Appl. Phys. Lett. **74**, 269 (1999).

[43] V. Holý, C. Giannini, L. Tapfer, T. Marschner, and W. Stolz, Phys. Rev. B **55**, 9960 (1997).

[44] U. Pietsch, H. Metzger, S. Rugel, B. Jenichen, and I. K. Robinson, J. Appl. Phys. **74**, 2381 (1993).

[45] P. Schittenhelm, C. Engel, F. Findeis, G. Abstreiter, A. A. Darhuber, G. Bauer, A. Kosogov, and P. Werner, J. Vac. Sci. Technol. B **16**, 1575 (1998).

[46] S. A. Chaparro, Y. Zhang, J. Drucker, D. Chandrasekhar, and D. J. Smith, J. Appl. Phys. **87**, 2245 (2000).

[47] I. Kegel, T. H. Metzger, and J. Peisl, Appl. Phys. Lett. **74**, 2978 (1999).

[48] K. Paschke, T. Geue, T. A. Barberka, A. Bolm, U. Pietsch, M. Rösch, E. Batke, F. Faller, K. Kerkel, J. Oshinowo, and A. Forchel, Appl. Phys. Lett. **70**, 1031 (1997).

[49] E. A. Kondrashkina, S. A. Stepanov, M. Schmidbauer, R. Opitz, R. Khler, and H. Rhan, J. Appl. Phys. **81**, 175 (1997).

[50] N. Darowski, U. Pietsch, U. Zeimer, V. Smirnitzki, and F. Bugge, J. Appl. Phys. **84**, 1366 (1998).

[51] J. H. Davies, Appl. Phys. Lett. **75**, 4142 (1999).

[52] T. H. Metzger, I. Kegel, R. Paniago, and J. Peisl, J. Phys. D **32**, A202 (1999).

[53] A.Darhuber, V. Holý, P. Schittenhelm, J. Stangl, I. Kegel, Z. Kovats, T. H. Metzger, G. Bauer, G. Ab-streiter, and G. Grübel, Physica E **2**, 789 (1998).

[54] J. Grim, V. Holý, J. Kubena, A. A. Darhuber, S. Zerlauth, and G. Bauer, Semicond. Sci. Technol. **14**, 443 (1999).

[55] P. Dutta and S. K. Sinha, Phys. Rev. Lett. **47**, 50 (1981).

[56] J. M. Cowley, *Diffraction Physics* (North-Holland Publishing Company, Amsterdam, 1975).

[57] S. Guha, A. Madhukar, and K. C. Rajkumar, Appl. Phys. Lett. **57**, 2110 (1990).

[58] R. Leon, Science **267**, 1966 (1995).

[59] A. P. Alivisatos, Science **271**, 933 (1996).

[60] F. H. Julien and A. Alexandrou, Science **282**, 1429 (1998).

[61] D. Bimberg, M. Grundmann, and N. N. Ledentsov, *Quantum Dot Heterostructures* (Wiley, Chichester, 1999).

[62] J. Groenen, R. Carles, S. Christiansen, M. Albrecht, W. Dorsch, H. P. Strunk, H. Wawra, and G. Wagner, Appl. Phys. Lett. **71**, 3856 (1997).

[63] B. R. Bennett, V. V. Shanabrook, E. R. Glaser, R. Magno, and M. E. Twigg, Superlatt. and Microstr. **21**, 267 (1999).

[64] O. V. Kolosov, M. R. Castell, C. D. Marsh, G. A. D. Briggs, T. I. Kamins, and R. S. Williams, Phys. Rev. Lett. **81**, 1046 (1998).

[65] Q. Shen, C. C. Umbach, B. Weselak, and J. M. Blakely, Phys. Rev. B **53**, R4237 (1996).

[66] T. Wiebach, M. Schmidbauer, M. Hanke, H. Raidt, R. Köhler, and H. Wawra, Phys. Rev. B **61**, 5571 (2000).

[67] M. Schmidbauer, T. Wiebach, H. Raidt, M. Hanke, R. Köhler, and H. Wawra, J. Phys. D: Appl. Phys. **32**, A230 (1999).

[68] N. Darowski, U. Pietsch, Y. Zhuang, S. Zerlauth, G. B. D. Lübbert, and T. Baumbach, Appl. Phys. Lett. **73**, 806 (1998).

[69] N. Darowski, K. Paschke, U. Pietsch, K. H. Wang, A. Forchel, T. Baumbach, and U. Zeimer, J. Phys. D: Appl. Phys. **30**, L55 (1997).

[70] A. J. Steinfort, P. M. L. O. Scholte, A. Ettema, F. Tuinstra, M. Nielsen, E. Landemark, D. M. Smilgies, R. Feidenhans'l, G. Falkenberg, L. Seehofer, and R. L. Johnson, Phys. Rev. Lett. **77**, 2009 (1996).

[71] V. Bressler-Hill, A. Lorke, S. Varma, P. M. Petroff, K. Pond, and W. H. Weinberg, Phys. Rev. B **50**, 8479 (1994).

[72] M. Biehl, W. Kinzel, and S. Schinzer, Europhys. Lett **41**, 443 (1998).

[73] I. Kegel, T. H. Metzger, A. Lorke, J. Peisl, J. Stangl, G. Bauer, J. M. García, and P. M. Petroff, *Nanometer-scale resolution of strain and interdiffusion in self-assembled InAs/GaAs quantum dots*, submitted for publication to Phys. Rev. Lett.

[74] I. Kegel, T. H. Metzger, A. Lorke, J. Peisl, J. Stangl, G. Bauer, W. V. Schoenfeld, and P. M. Petroff, *Determination of strain fields and composition of self-organized quantum dots with X-Ray Diffraction*, submitted for publication to Phys. Rev. B.

[75] I. Kegel, T. H. Metzger, J. Peisl, A. Lorke, J. P. Kotthaus, J. M. García, and P. M. Petroff, Mat. Res. Soc. Symp. Proc. **524**, 89 (1998).

[76] T. H. Metzger, I. Kegel, R. Paniago, A. Lorke, J. Peisl, J. Schulze, I. Eisele, P. Schittenhelm, and G. Abstreiter, Thin solid films **336**, 1 (1998).

[77] M. Rauscher, R. Paniago, H. Metzger, Z. Kovats, J. Domke, J. Peisl, H. D. Pfannes, J. Schulze, and I. Eisele, J. Appl. Phys. **86**, 6763 (1999).

[78] T. H. Metzger, I. Kegel, R. Paniago, and J. Peisl, J. Phys. D: Appl. Phys. **32**, A202 (1999).

[79] M. Tolan, *X-Ray Scattering from Soft-Matter Thin Films* (Springer-Verlag, Berlin, 1999), Chap. 2.

[80] P. Ehrhart, J. Nucl. Mater **216**, 170 (1994), and references therein.

[81] D. E. Jesson, M. Kästner, and B. Voigtländer, Phys. Rev. Lett. **84**, 330 (2000).

[82] J.-J. Shen, A. Brown, R. A. Metzger, B. Sievers, L. Bottomley, P. Eckert, and W. B. Carter, J. Vac. Sci. Technol. B **16**, 1326 (1998).

[83] N. Grandjean, J. Massies, and O. Tottereau, Phys. Rev. B **55**, R10189 (1997).

[84] P. B. Joyce, T. J. Krzyzewski, G. R. Bell, B. A. Joyce, and T. S. Jones, Phys. Rev. B **58**, R15981 (1998).

[85] E. Mateeva, P. Sutter, and M. G. Lagally, Appl. Phys. Lett. **74**, 567 (1999).

[86] G. Medeiros-Ribeiro, A. M. Bratkovski, T. I. Kamins, D. A. A. Ohlberg, and R. S. Williams, Science **279**, 353 (1998).

[87] A. Madhukar, Q. Xie, P. Chen, and A. Konkar, Appl. Phys. Lett. **64**, 2727 (1994).

[88] G. S. Solomon, J. A. Trezza, and J. S. Harris, Appl. Phys. Lett. **66**, 991 (1995).

[89] H. Eisele, O. Flebbe, T. Kalka, C. Preinesberger, F. Heinrichsdorff, A. Krost, D. Bimberg, and M. Dähne-Prietsch, Appl. Phys. Lett. **75**, 106 (1999).

[90] B. E. Warren, *X-Ray Diffraction* (Dover Publications, New York, 1990), Chap. 3.3.

[91] W. Dorsch, H. P. Strunk, H. Wawra, G. Wagner, J. Groenen, and R. Charles, Appl. Phys. Lett. **72**, 179 (1998).

[92] R. Leon, J. Wellman, X. Z. Liao, J. Zou, and D. J. H. Cockayne, Appl. Phys. Lett. **76**, 1558 (2000).

[93] X. Z. Liao, J. Zou, D. J. H. Cockayne, R. Leon, and C. Lobo, Phys. Rev. Lett. **82**, 5148 (1999).

[94] N. Liu, J. Tersoff, O. Baklenov, A. L. Holmes, Jr., and C. K. Shih, Phys. Rev. Lett. **84**, 334 (2000).

[95] B. Lita, R. S. Goldman, J. D. Phillips, and P. K. Bhattacharya, Appl. Phys. Lett. **75**, 2797 (1999).

[96] M. A. Salmi, M. Alatalo, T. Ala-Nissila, and R. M. Nieminen, Surface Science **425**, 31 (1999).

[97] M. Schmidt, R. Kusche, B. von Issendorf, and H. Haberland, Nature **393**, 238 (1998).

[98] A. Ulyanenkov, N. Darowski, J. Grenzer, U. Pietsch, K. H. Wang, and A. Forchel, Phys. Rev. B **60**, 16701 (1999).

[99] K. Nordlund, P. Partyka, R. S. Averback, I. K. Robinson, and P. Ehrhart, *Atomistic simulation of diffuse X-ray scattering from defects in solids*, submitted for publication to J. Appl. Phys., and references therein.

[100] C. Pryor, Phys. Rev. B **57**, 7190 (1998), and references therein.

[101] K. Nordlund, J. Nord, J. Frantz, and J. Keinonen, Comput. Mater. Sci. (2000), accepted for publication.

[102] W. H. Press, S. A. Teukolsky, W. T. Vetterling, and B. P. Flannery, *Numerical Recipies in C; The Art of Scientific Computing*, 2nd ed. (Cambridge University Press, New York, 1995).

[103] G. D. Lian, J. Yuan, L. M. Bown, G. H. Kim, and D. A. Ritchie, Appl. Phys. Lett. **73**, 49 (1998).

[104] T. Salditt, D. Lott, T. H. Metzger, J. Peisl, G. Vignaud, and P. Høghøj, Phys. Rev. B **54**, 5860 (1996).

[105] O. Glatter and O. Kratky, *Small Angle X-ray Scattering* (Academic Press, London, New York, 1982).

Danksagung

Meinem Doktorvater Prof. Dr. J. Peisl danke ich für die Möglichkeit, meine Doktorarbeit in der kreativen und kollegialen Atmosphäre seines Lehrstuhls durchführen zu können.

Herrn Dr. Hartmut Metzger danke ich für seine Betreuung und den Ideenreichtum, mit dem er die experimentelle Seite dieser Arbeit begleitete. Ohne seine vielfältigen Kontakte zu Synchrotronen und Wachtumsgruppen in aller Welt wäre meine Arbeit nicht in dieser Form zustande gekommen.

Julian Stangl und Herrn Prof. Dr. G. Bauer von der Johannes-Kepler-Universität in Linz danke ich für die äußerst fruchtbare experimentelle Zusammenarbeit. Auch als Diskussionspartner in streutechnischen Fragen waren sie sowohl für meine Motivation als auch für den notwendigen kritischen Dialog von nicht zu unterschätzendem Einfluß.

Ohne die Arbeit von Detlef Smilgies am TROÏKA II Strahlrohr der ESRF, der uns mit seinem hochpräzisen Diffraktometer immer wieder einen Experimentierplatz von kaum zu überbietender Effektivität zur Verfügung stellte, wäre die hohe Qualität der Meßdaten nicht erreicht worden.

Dr. Kai Nordlund danke ich für die begeisternde und erfolgreiche Zusammenarbeit bei den atomistischen Simulationen in München und Helsinki sowie für seine Gastfreundschaft bei meinem Aufenthalt in Finnland.

Für wertvolle simulationstechnische Hinweise auf dem Weg zu einer Herleitung der verallgemeinerten optischen Funktion gilt Dr. Vaclav Holý von der Masaryk Universität in Brno mein Dank.

Jorge García und Winston Schoenfeld danke ich in ihrer Eigenschaft als Mitarbeiter des Materials Department der University of California, Santa Barbara für die Proben, die für das Gelingen meine Arbeit ein wesentlicher Beitrag waren.

Für sein unermüdliches Interesse an meiner Arbeit und seine Vermittlungen und Nachhilfestunden in Probenfragen möchte ich Axel Lorke von der Universität München danken.

Markus Arzberger vom Walter-Schottky-Institut in München gilt mein Dank für die unkomplizierte und zügige Bereitstellung einer Probenserie in

einer experimentellen Notsituation.

Ich danke Herrn Prof. Moss für die hartnäckige Anregung von Appendix E und andere interessante Diskussionen.

Jim Patel vom SSRL in Stanford danke ich für sein Vertrauen und seine freundlichen Führungen durch Palo Alto samt interessanter Erzählungen über kalifornische Geschichte.

Mein Dank richtet sich außerdem an Herrn Wolf und die Werkstatt im Hauptgebäude der Universität München für die prompte Anfertigungen von Adapterplatten, Halterungen und Abdichtungen aller Art.

Ganz besonders möchte ich den Doktoranden und Doktorandinnen des Lehrstuhls für ihre Hilfsbereitschaft, Diskussionsfreude und nicht zuletzt für die interessanten Gespräche beim Mittagessen in der “Landwirtschaft” danken.

Diese Arbeit wurde durch die Deutsche Forschungsgemeinschaft unter der Projekt-Nr. Pe 127/1-6+2 unterstützt. Die Kooperation mit Dr. K. Nordlund in Finnland wurde durch den Deutschen Akademischen Austauschdienst unter der Projekt-Nr. 313/SF-PPP 6/98 finanziert.

Veröffentlichte Teile der Arbeit

- A.Darhuber, V. Holý, P. Schittenhelm, J. Stangl, I. Kegel, Z. Kovats, T. H. Metzger, G. Bauer, G. Abstreiter, and G. Grübel, *Structural characterization of self-assembled Ge dot multilayers by x-ray diffraction and reflectivity methods*, Physica E **2**, 789 (1998).

- I. Kegel, T. H. Metzger, J. Peisl, A. Lorke, J. P. Kotthaus, J. M. García, and P. M. Petroff, *Shape, size, strain and correlations in quantum dot systems studied by grazing incidence x-ray scattering methods*, Mat. Res. Soc. Symp. Proc. **524**, 89 (1998).

- T. H. Metzger, I. Kegel, R. Paniago, A. Lorke, J. Peisl, J. Schulze, I. Eisele, P. Schittenhelm, and G. Abstreiter, *Shape, size, strain and correlations in quantum dot systems studied by grazing incidence x-ray scattering methods*, Thin solid films **336**, 1 (1998).

- I. Kegel, T. H. Metzger, P. Fratzl, J. Peisl, A. Lorke, J. M. García, and P. M. Petroff, *Interdependence of strain and shape in self-assembled coherent InAs islands on GaAs*, Europhys. Lett **45**, 222 (1999).

- T. H. Metzger, I. Kegel, R. Paniago, and J. Peisl, *Grazing incidence x-ray scattering: an ideal tool to study the structure of quantum dots*, J. Phys. D: Appl. Phys. **32**, A202 (1999).

- I. Kegel, T. Metzger, J. Peisl, J. Stangl, G. Bauer, and D. Smilgies, *Vertical alignment of multilayered quantum dots studied by x-ray grazing-incidence diffraction*, Phys. Rev. B **60**, 2516 (1999).

- J. Stangl, V. Holý, P. Mikulik, G. Bauer, I. Kegel, T. H. Metzger, O. G. Schmid, C. Lange, and K. Eberl, *Self-assembled carbon-induced germanium quantum dots studied by grazing-incidence small-angle x-ray scattering*, Appl. Phys. Lett. **74**, 3785 (1999).

- I. Kegel, T. H. Metzger, and J. Peisl, *Lateral ordering of coherent Ge islands on Si(001) studied by triple-crystal grazing incidence diffraction*, Appl. Phys. Lett. **74**, 2978 (1999).
- I. Kegel, T. H. Metzger, A. Lorke, J. Peisl, J. Stangl, G. Bauer, J. M. García, and P. M. Petroff, *Nanometer-scale resolution of strain and interdiffusion in self-assembled InAs/GaAs quantum dots*, submitted for publication to Phys. Rev. Lett.
- I. Kegel, T. H. Metzger, A. Lorke, J. Peisl, J. Stangl, G. Bauer, W. V. Schoenfeld, and P. M. Petroff, *Determination of strain fields and composition of self-organized quantum dots with x-ray diffraction*, submitted for publication to Phys. Rev. B.

Lebenslauf

Name	Ingo Kegel
E-mail	ingo.kegel@gmx.net
Geburtsdatum	16.12.1972
Geburtsort	Berlin
Staatsangehörigkeit	Deutschland
Familienstand	ledig
Eltern	Brigitte und Gerd Kegel
Schule	
1979-1984	Joseph-Dosch-Grundschule in Gauting
1984-1990	Otto-von-Taube-Gymnasium in Gauting
1990-1992	United World College of the Adriatic (Italien)
1992	International Baccalaureate
Studium	
1992-1997	Physik an der Ludwig-Maximilians-Universität München
1997	Diplom Physik
1998-2000	Promotion am Lehrstuhl Peisl an der Ludwig-Maximilians-Universität München
Beruf	
seit 1997	IT-Projektleiter bei IMS Health in Hallbergmoos